# NEUTRON EXPOSURE FROM ELECTROM LINEAR ACCELERATORS AND A PROTON ACCELERATOR: MEASUREMENTS AND SIMULATIONS

---

A  Dissertation Presented to

The Faculty of the Graduate School

At the University of Missouri

---

In Partial Fulfillment

Of the Requirements for the Degree

Doctor of Philosophy

---

By

KUAN LING CHEN

Dr. Eric E. Klein          Dissertation Supervisor

Dr. Sudarshan K. Loyalka          Dissertation Supervisor

Dr. William H. Miller          Dissertation Supervisor

DECEMBER 2011

The undersigned, appointed by the dean of the Graduate School,
have examined the dissertation entitled

**Neutron Exposure from Electron Linear Accelerators and a Proton**

**Accelerator: Measurements and Simulations**

Presented by Kuan Ling Chen
A candidate for the degree of
Doctor of Philosophy
And hereby certify that, in their opinion, it is worthy of acceptance.

_____

Dr. Eric E. Klein

_____

Dr. Sudarshan K. Loyalka

_____

Dr. William H. Miller

_____

Dr. Tushar K. Ghosh

_____

Dr. Mark A. Prelas

_____

Dr. Robert V. Tompson Jr.

_____

Dr. Lixin Ma

This work is dedicated to my ever-supportive parents and family. 謝謝你們一路走來的支持與疼愛!

# ACKNOWLEDGEMENTS

# TABLE OF CONTENTS

# LIST OF TABLES

# LIST OF ILLUSTRATIONS

# ABSTRACT

The risk of developing radiation induced secondary cancers in patients undergoing external beam radiotherapy is a concern; particularly from secondary neutrons generated during delivery of high energy photon and proton beams. This work also investigated the effectiveness of several shielding materials commonly used for neutron shielding. It was found that high density concretes with higher concentrations of hydrogenous materials to be more suitable for space-restricted environments.

This work studied neutron production around two photon linear accelerators using measurements. It was found that ambient neutron dose equivalents from Elekta accelerator were significant lower than from Varian accelerator, especially for 18MV beams.

Neutron dose equivalent per therapeutic dose (H/D) around the MEVION S250 Proton Therapy System were evaluated using measurements and MCNPX calculations. It was found that H/D decreased as field sizes increased, and with distance from isocenter. The neutron production from the MEVION S250 was found to be comparable with other passive scattering systems.

**PRECEDING**

**THE ORANGIZATION OF THIS DISSERTATION**

This Dissertation has been organized into four chapters. Chapter 1 overviews the principle motive of this work and states three related questions (specific aims) and respective hypotheses. Chapter 1 also describes briefly the instrumentation for neutron measurements and Monte Carlo methods for particle transports which are used throughout the studies.

Chapter 2-4 are self-contained in that each of them contains the theoretical background, methods, results, and discussions associated with the specific problems stated in Chapter 1. In Chapter 2, the effectiveness of various materials used for radiation shielding, particularly for neutron shielding, is investigated. Chapter 3 compares the neutron productions from two types of electron linear accelerators: Varian and Elekta. In Chapter 4, neutron production from the first compact proton accelerator (MEVION S250 Proton Therapy System) is studied.

# CHAPTER 1

# INTRODUCTION AND BACKGROUND

This chapter overviews the principle motive of this work.  Three related questions (specific aims) and respective hypotheses are given.  An overview of the instrumentation for neutron measurements related to this dissertation is provided.  Finally, a brief introduction to the Monte Carlo method for particle transports used throughout the studies is included.

## 1.1    Clinical Concern of Neutron Exposure

Cancer is the second most common cause of death in the United States.  The sophistication of radiation delivery methods and systems have made radiotherapy a well-accepted treatment option to treat a variety of cancer types.  While the use of radiotherapy has increased the chances of survival of cancer patients, the increasing risk of developing secondary malignancies in patients that undergo radiotherapy has raised a concern.  Because there are uncertainties in correlating the risk of secondary cancers with radiotherapy, there is no conclusive and exclusive correlation between the two based on many retrospective studies that have investigated the risks of radiation-induced secondary cancers. [1-8]  For example, some studies reported no statistically significant difference between radiotherapy and other treatment modalities [1-2]; whereas some observed increased risk of radiation-induced secondary malignancies [3-6].  Nonetheless, the carcinogenic risk induced by ionizing radiation is well-known based on the statistical data drawn from studies of atomic bomb survivors, and the cancer dose-response relations indicate that cancer risk increases as absorbed dose increases

from about 0.05 Gy up to 2.5 Gy. [9]  Aside from absorbed dose, other factors including source radiation type, beam quality, irradiated volume ([9]), and secondary radiations, have strong influences on the chances of cancer occurrence.  In particular, stray radiations result in higher integral dose, which in turn increases the risks of secondary malignances [10].  In particular, neutron production from both high energy conventional linear accelerators and proton accelerators are the main sources of stray radiation.

## 1.2    Statement of the Problem and Specific Aims

In light of the fact that majority of cancer patients have been treated with radiation from external beams from linear accelerators [11], and studies have shown that dose from secondary neutrons was small, but not negligible.  Hence, the goal of this work is to evaluate neutron dose equivalents around the three different models of medical accelerators used for external beam radiotherapy.  Specifically for the first compact proton accelerator, the MEVION S250 (MEVION Medical Systems, MA), the main focus is to obtain an estimation of the neutron dose to a patient and for shielding needed for the treatment room.  The specific aims are as follows:

**Specific Aim 1:** Investigate the effectiveness of various shielding materials to be used in the proton facility at Washington University School of Medicine in St. Louis (WUSM).

**Hypothesis:**    Materials with higher iron concentration are more effective in stopping neutrons.

2

**Specific Aim 2:**  Compare neutron productions from two conventional linear accelerators: Varian and Elekta.

**Hypothesis:**  The electron accelerator from Elekta produces less secondary neutron dose due to the additional filter structure in the beam-line.


**Specific Aim 3:**  Characterize the neutron production from the MEVION S250 proton accelerator.

**Hypothesis:**  The neutron production from the MEVION S250 is comparable with other existing (passive scattering) proton accelerators.


## 1.3    An Overview of Instrumentation for Neutron Measurements

Since neutrons have no charge, the detection of neutrons depends on the ionizing properties of the products from neutron interaction with the target nuclei.  Neutrons interact with the nuclei of the target materials through elastic scattering, inelastic scattering and absorption, and the products from these interactions include recoil nuclei, charged particles, gamma ray and fission recoils.  The probabilities of various types of neutrons interactions depend on the neutron energy.  Neutrons can be categorized into several groups based on their energy.  Slow neutrons have energy range of 0.0253 eV to 0.1 keV.  In particular, neutrons with energy below about 1 eV are thermal neutrons, which neutrons are in approximate thermal equilibrium with matter.  The most important interaction for slow neutrons with matter is absorption and elastic scattering.  Intermediate neutrons have energy from 0.5 eV to 10 keV. This group is associated with resonances regions in neutron cross section.  Fast neutrons have energy range of 10 keV to 10 MeV.  Up to about 10 MeV, elastic scattering interaction is

important.  As energy increases, a nuclear reaction such as inelastic scattering becomes more important. [12-14]

Materials with large neutron reaction cross sections are desired so that efficient detectors can be built with small dimensions.  The cross section for neutron interactions in most materials is related to neutron energy.  Different detectors have been developed for different neutron energy regions.  In many instances, gamma ray production is significant, so that the choice of reaction relates to the ability to discriminate these gamma rays in the neutron detection process.  [13-14]

The most popular reaction used for neutron detection is the neutron capture reaction by boron-10, lithium-6 and helium-3 as shown in following.

$$^{10}_{5}B + {}^{1}_{0}n \rightarrow {}^{7}_{3}Li + {}^{4}_{2}He + 2.79 \text{ MeV}$$

$$^{6}_{3}Li + {}^{1}_{0}n \rightarrow {}^{3}_{1}H + {}^{4}_{2}He + 4.78 \text{ MeV}$$

$$^{3}_{2}He + {}^{1}_{0}n \rightarrow {}^{3}_{1}H + {}^{1}_{1}H + 0.76 \text{ MeV}$$
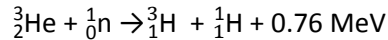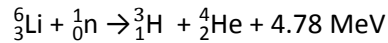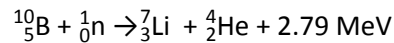
There are various types of commercially available neutron detectors that operate on these reactions.  One of the most common detectors used is the boron tri-fluoride ($BF_3$) proportional counter which is based on (n, $\alpha$) reaction for thermal neutron detections.  The $BF_3$ served both as the target for slow neutron conversion into secondary particles as well as a proportional gas.  The proportional counter usually is surrounded by a thick layer of polyethylene moderator to slow the neutrons down to an energy where they maybe efficiently captured by the nuclei of the detector gas.  In the case of $BF_3$ detector, the detections rely on the signal from the emitted alpha particle and lithium particles.  If a series of spheres with different diameters is used, neutron can be thermalized to different energies to obtain the

neutron flux spectrum. This technique was first developed by Brambeltt, Ewing and Bonner (1960, [15]). The $BF_3$ detector can be replaced with a lithium iodide ([6]LiI) detector, which is also based on (n, α) reaction. A small amount of europium (Eu) usually is incorporated as activator to form a [6]LiI(Eu) scintillation counter.

An example of using [3]He(n,α)[3]H is a the wide energy neutron detection instrument (WENDI) developed at Los Alamos National Laboratory. It is a type of neutron Roentgen equivalent man (rem) meter which also utilize the polyethylene as a moderator for detection. A unique feature of this instrument is the tungsten materials added around the [3]He tube as a neutron source to improve the high energy response of the meter beyond 8 MeV. [16-17]

In practice, every neutron monitoring instrument usually has a response function that approximately follows the ambient neutron dose equivalent, H*(10), for a given type of radiation over a given energy range. They measure the spectral neutron fluence and fold the information with an appropriate set of fluence-to-dose-equivalent conversion coefficients.

Neutron dose equivalent can also be measured with superheated liquid dosimeters. As neutrons enter the dosimeters, superheated droplets can be nucleated to form vapor by the recoil nuclei in the medium where the droplets are located. The vapor must exceed a critical radius determined by the mechanical equilibrium of surface tension of the liquid and pressure difference through the chamber wall to be registered. Two types of these neutron dosimeters exist, one is sensitive to fast neutrons and the other to thermal and epithermal neutrons via [6]Li(n, α)[3]H reaction. [18-20]

## 1.4    An Overview of Monte Carlo Methods for Particle Transport

## (MCNPX)

The Monte Carlo method uses a large number of randomized particle histories to estimate the average particle behavior.  In Monte Carlo calculations, particle histories or tracks are generated by random sampling of probability density functions of the particle interactions with the medium.  The probability distributions of the interactions and particle productions are usually expressed by tabulated experimental data or theoretical equations.   As more interactions occur within the simulation, the statistical uncertainty decreases.

The Monte Carlo particle transport system chosen for this work is the Monte Carlo N-Particle eXtended (MCNPX, version 2.6.0 [21]) transport code developed at the Los Alamos National Laboratory, USA.  The MCNPX development began in 1994 as extension of MCNP4B and LAHET.   MCNPX is a general purpose code that can be used to simulate 34 different types of particles of any energy.   It is fully three-dimensional and time dependent.   The three dimensional code geometry is based on cells obtained by interaction between first, second and some fourth degree surfaces.  In MCNPX, the algorithm used for electron transport is based on the condensed history method proposed by Berger (1963 [22]).   In particular, Goudsmit-Sauderson theory is used for angular deflections and the energy loss fluctuations is based on the enhancements of the Landau theory. [23-25]  The bremsstrahlung model is derived from the Koch and Moch theory [26].  More details are described in the MCNP user's manuals. [27-28] MCNPX utilizes the latest nuclear cross section libraries, which include continuous cross section data, with a range for neutrons, photons, electrons and protons that extend to energy up to 150 MeV.  Physics models are used for particle types and energies where tabular data are not available.  In this work, the most recently available cross section libraries are used whenever

possible with the mix-and-match feature provided in MCNPX.  The output data are normalized per source particle and can be either surface current, surface and cell flux, energy deposition into a cell, or fission and heating.  Several variance reduction features are also provided in MCNPX, including energy and time cutoffs, geometry, energy and time splitting, and biasing for different variables.  [21, 28]  These variance reducing techniques are used to the computation time required to obtain results of sufficient precision.

In this work, neutron fluences are tallied in a cell using F4 tally. It is a track length estimator in which the particle fluence is obtained by tallying the distance that a particle moves while inside the cell.  All particles entering the cell contribute to the final tally.  The obtained neutron fluences can be converted to ambient neutron dose equivalent using the conversion coefficient available in the NCRP Report No. 38 (1971, [12]) or ICRP publication 74 (1996 [29]). The flux-to-dose conversion factor as a function of neutron energy is shown in Figure 1.1.  The F6 tally is track length estimate of energy deposition and is used to tally the energy deposition over the simulation cell.
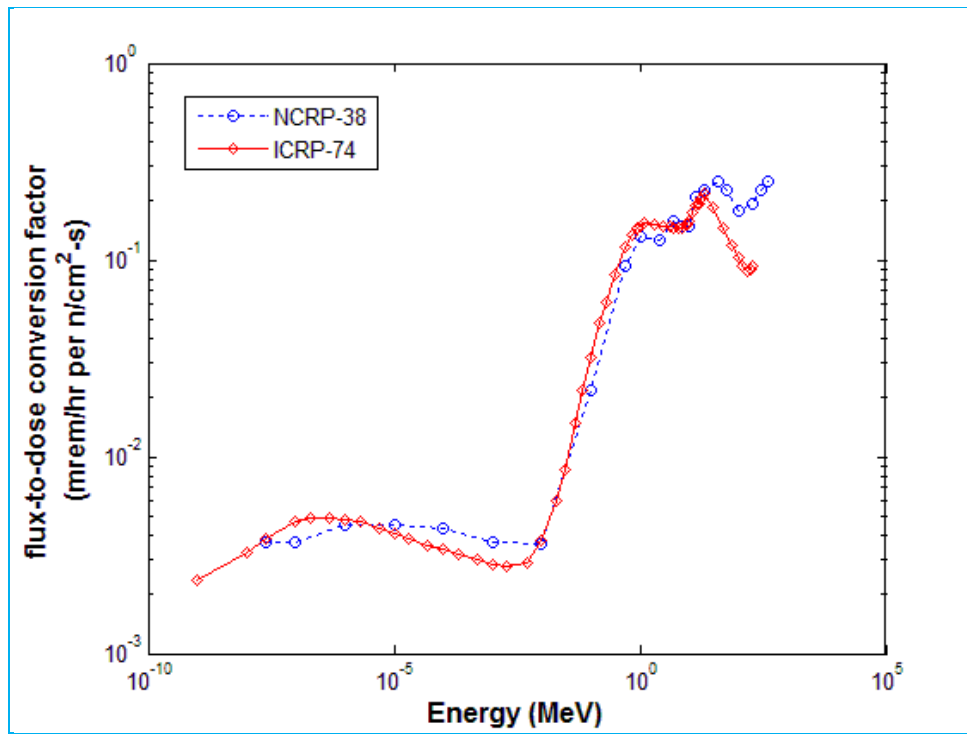
**Figure 1.1** Flux-to-dose equivalent conversion factors as a function of neutron energy from the NCRP Report No. 38 (1971 [12]) and ICRP publication 74 (1996 [29]).

# CHAPTER 2

# NEUTRON SHIELDING MATERIALS FOR THE MEVION S250 PROTON ACCELERATOR

This chapter focuses on the first specific aim stated in Chapter 1.  A brief introduction of shielding materials for neutrons is given, followed by the methods and materials that are specific for this chapter.  Finally, the results and discussion are included.

> Specific Aim 1:  Investigate the effectiveness of various shielding materials to
>
> be used in the proton facility at Washington University School
>
> of Medicine in St. Louis (WUSM).

> Hypothesis:  High density concrete samples with higher hydrogen
>
> concentrations are more effective in stopping neutrons.

## 2.1    Introduction

Secondary particles generated from high energy proton accelerators, especially neutrons, create a radiation protection challenge due to their abundance and highly penetrating nature.  Strategies for design and shielding methods vary considerable with configurations of proton facilities.  The material chosen for shielding is a balance of effectiveness and cost since the cost of building a proton facility is generally in the range of several tens to hundreds of million dollars, depending on the size of a facility.  Both analytical and statistical shielding calculations rely on neutron attenuation properties of chosen materials.

## 2.1.1    Shielding of Neutron Sources

The goal in designing radiation shielding is to remove all of the primary and secondary radiation emitted by a source.  Shielding of fast neutrons sources basically follows a three-step logic.  First, use materials with low atomic number (low Z), especially hydrogen, near the neutron sources.  Because low Z materials have large scattering cross sections, neutrons may lose a large fraction of their energy through elastic and inelastic scattering in a single collision and become thermal neutrons.  Second, since thermal neutrons are much easier to be captured, materials like boron with higher absorption cross sections are ideal to be placed after the fast neutron moderators.  Third, since many shielding materials produce gamma rays from inelastic scattering interactions, materials appropriate for photon shielding such as lead, steel and concrete, are used subsequent to thermal neutron shielding.  Thermal neutron cross sections for some elements that are commonly in connection with neutron shielding are given Table 2.1. [30 – 32]

**Table 2.1**    Thermal neutron cross sections for elements that related to neutron shielding.

| Element or Isotope | cross section ($b = 10^{-28}$ m$^2$) | |
| --- | --- | --- |
| | Scattering | Absorbing |
| Hydrogen | 38 | 0.33 |
| Oxygen | 3.76 | 27 |
| Boron | 4 | 759 |
| B-10 | -- | 3838 |
| Silicon | 2.2 | 0.16 |
| Iron | 11 | 2.55 |
| Cadmium | 6 | 2450 |

## 2.1.2    Materials for Neutron Shielding

Hydrogenous materials are efficient neutron shields, as approximately half of the energy of intermediate and fast neutrons is transferred to hydrogen atoms by elastic scattering. However, the drawback is the 2.22 MeV gamma ray emissions from $^1$H (n,γ) $^2$H reaction,  which require additional shielding.   Cadmium is a good neutron absorber since it has a high (n,γ) neutron capture cross section (2450 b).  However, it also produces gamma rays of 9.05 MeV that require shielding.

Boron is often incorporated into neutron shielding because of its large absorption cross section (759 b).   In addition, boron-10 ($^{10}$B), a constituent of 20% of nature boron, has large thermal neutron absorption cross sections (3838 b).  Although there are 0.48 MeV gamma rays emitted as a result of $^{10}$B (n,α) $^7$Li interaction, these gamma rays are easier to shield than the gamma rays from hydrogen capture.  A popular use of boron, is to combine it with polyethylene, a high hydrogen concentrated hydrocarbon material, to absorb thermal neutrons from hydrogen interactions.

Iron slows high energy neutrons down through inelastic scattering and the average neutron energy after inelastic scattering is proportional to square root of the incident neutron energy (E) and the mass number (A) ratio, i.e. $(E/A)^{1/2}$.  However, the lowest inelastic scattering energy level of iron-56 ($^{56}$Fe) is 874 keV, and $^{56}$Fe composed of 91.7% of natural iron.  For neutron energies below 874 keV, neutrons can only loss energy inefficiently via elastic scattering in the dominant $^{56}$Fe nucleus.  Therefore, to increase the efficiency in shielding high energy neutrons, light elements such as concrete can be used after iron or steel shields. [33]

Concrete and earth are widely used in building construction as radiation shields for the following reasons. They are dense, uniform and can serve as both shielding and structural support. They contain water and materials with light elements which are effective of absorbing thermal neutrons. They also contain materials such as metal that are excellent for gamma ray attenuations. The main component of dry earth is silicon dioxide ($SiO_2$) which is an effective material for both neutron and photon shielding. Concrete slabs are easy to construct and can be poured in places as permanent shielding or be made into concrete blocks for temporary shielding. For space-restricted environments, high density concrete is desirable. The density of concrete depends on its moisture content. Natural heavyweight aggregates consisting of magnetite ($Fe_2O_3 \cdot FeO$), ilmenite ($FeO \cdot TiO_2$), barite ($BaSO_4$) and hematite ($Fe_2O_3$) are often used to obtain high density concretes with density ranging from 2.9 to 6.1 $g/cm^3$. Hydrous aggregates such as serpentine ($3MgO \cdot 2SiO \cdot 2H2O$) and limonite ($Fe_2O_3 \cdot XH2O$), and other boron mineral are often included to moderate and absorb neutrons. [34 – 35]

Studies show that hydrogen content and concrete density determine the effectiveness of the concrete for shielding, thus they contribute an important part in selecting neutron shielding and gamma rays attenuation when designing radiation shields. [36 – 40] Bashter (1997 [36]) measured and calculated the neutron effective macroscopic removal cross section ($\Sigma_R$, $cm^{-1}$) and photon mass attenuation coefficient for seven types of concrete with densities ranging from 2.3 to 5.11 $g/cm^3$. The author reported that hematite-serpentine concrete had practical uses for neutron shielding since the serpentine aggregates retained most of its crystallization water at high temperature up to ~ 500 °C. The author concluded that the high density steel-magnetite concrete was an effective shield for both neutrons and photons. Abdo (2002 [37]) also suggested to use high density aggregates, such as magnetite, hematite and ilmenite ores, combined with hydrogenous ores, such as limonite and serpentine ores, to obtain a maximum

12

density for γ-ray shielding and retaining a sufficient moderating water for neutron shielding. Kharita *et al* (2008 [40]) measured the half value layer (HVL, cm) of six concrete samples in Am-Be neutron fields. They reported the concrete sample with high content of iron with present of iron hydroxides was the most efficient neutron shielding material.  They also concluded that samples with high content of hydrogen or carbon were good shielding materials for neutrons.

## 2.2     Methods and Materials
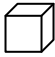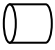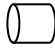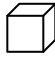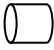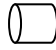
To quantify the effectiveness of high density materials used for neutron shielding in the new proton facility at WUSM, the tenth value layer (TVL, $cm^{-1}$) of the material samples were determined by both measurement and Monte Carlo calculations.  Along with the high density concrete samples, four other samples commonly incorporated in radiation shielding, were also included in the study.

A total of seven samples were investigated and their physical properties are listed in Table 2.2. The samples including three high density concrete (HDC) blocks supplied by a local manufacturer (Ranineri Building Materials, Inc. St. Louis, MO), a commercially available high density concrete, a regular density concrete (RDC), a steel sample (S), and a borated polyethylene sample (BPE).  The samples varied in geometric size and shape.  Samples A – C were the high density concrete designed specifically for the proton facility at WUSM.  They were composed of an iron heavy hematite mix, with approximately 60 % – 70 % iron by weight.  Since the aggregates mixed in these samples were acquired locally, each of the samples had slightly different density from the others as shown in Table 2.2.  Two square slabs of sample A were made for measurements, with a density of 4.27 $g/cm^3$ and dimensions of 6.7 × 21.5 × 21.5 $cm^3$

and 7.4 × 24.5 × 25.5 cm$^3$.  Sample B was a cylindrical block with a dimension of 30.5 cm in length and 15.5 cm in diameter, and a density of 3.70 g/cm$^3$.  Sample C also was a cylindrical block with a dimension of 20 cm in length and 10 cm in diameter, and a density of 2.89 g/cm$^3$.

Sample D was a commercially available high density block (Nuclear Shielding and Supplies, Tucson, AZ).  It had a density of 4.8 g/cm$^3$ and approximate dimensions of 10.16 × 15.25 × 43.18 cm$^3$.  Sample E was a regular density concrete brick with a density of 2.3 g/cm$^3$ and a dimension of 9.2 × 19 × 39 cm$^3$.  Sample F was a steel block with a density of 7.75 g/cm$^3$ and dimensions of 17 cm in length and 10.2 cm in diameter.  Sample G was a borated polyethylene cylinder with 5% boron by weight.  The density of sample G was 1.08 g/cm$^3$ and its dimension was 32.6 cm in length and 10.4 cm in diameter.

**Table 2.2**     Materials samples used for measurements and their physical properties. Where sample A – D are high density concretes (HDC); sample E is a regular density concrete (RDC); sample F is steel and sample G is borated polyethylene.

| Sample # | A | B | C | D | E | F | G |
|---|---|---|---|---|---|---|---|
| Materials | HDC | HDC | HDC | HDC | RDC | S | BPE |
| Density (g/cm$^3$) | 4.27 | 3.70 | 2.89 | 4.80 | 2.35 | 7.75 | 1.08 |
| Geometry | Slab | Cylinder | Cylinder | Chevron | Slab | Cylinder | Cylinder |

## 2.2.1     Neutron Attenuation Measurements of Shielding Materials

In this work, all measurements were performed at University of Missouri Research Reactor (MURR). A single plutonium beryllium ($^{239}$PuBe) neutron source was used in all measurements and calculations. The 5 Curie $^{239}$PuBe source was cylindrical in shape with a length of 13.0 cm and a diameter of 2.5 cm. Beryllium is an excellent target for neutron production because of its low neutron binding energy. This isotopic neutron source was desirable since it yielded neutron with specific energy and intensity distribution. The $^{239}$PuBe source has a continuous energy spectrum up to 11 MeV and an average energy of 4.83 MeV as seen in Figure 2.1. [41]
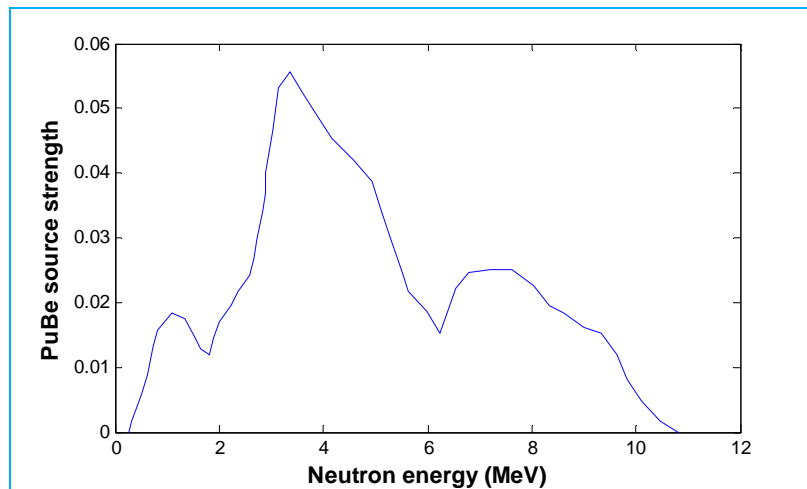


**Figure 2.1**     Normalized neutron spectrum of 5 Ci PuBe source. Note: figure is adapted from Griffin *et al.* (2008, [41])

A Bonner Sphere Spectrometer (BSS) system (Ludlum Measurements, Inc., Sweetwater, Texas) was used to determine neutron fluence spectrum and dose equivalent. This BSS system

consisted of a 6 different size modulating spheres made with high density polyethylene. The BSS utilized a 4mm high by 4 mm diameter cylindrical $^6$LiI(Eu) scintillator as a thermal neutron sensor. The BSS was sensitive to the neutron energy from thermal to approximately 12 MeV.

For each attenuation path, eight measurements were performed with the bare detector, detector covered with a cadmium layer, and spheres with diameter of 2", 3", 5", 8", 10" and 12". Corrections for dead time and gamma ray background were applied prior to unfolding. [42 – 43] A schematic diagram of measurement set up was shown in Figure 2.2. The distance between the center of $^{239}$PuBe source and the center of Bonner sphere system was 80cm (SDD). Material samples were placed at the same level as the BSS so that the center of each sample is at the same level as the detector, i.e. the $^6$LiI(Eu) scintillator. Although samples were different in shape and sizes, all samples were configured in a manner to allow measurements through various paths. At least two different thicknesses were used for measurement in each sample.
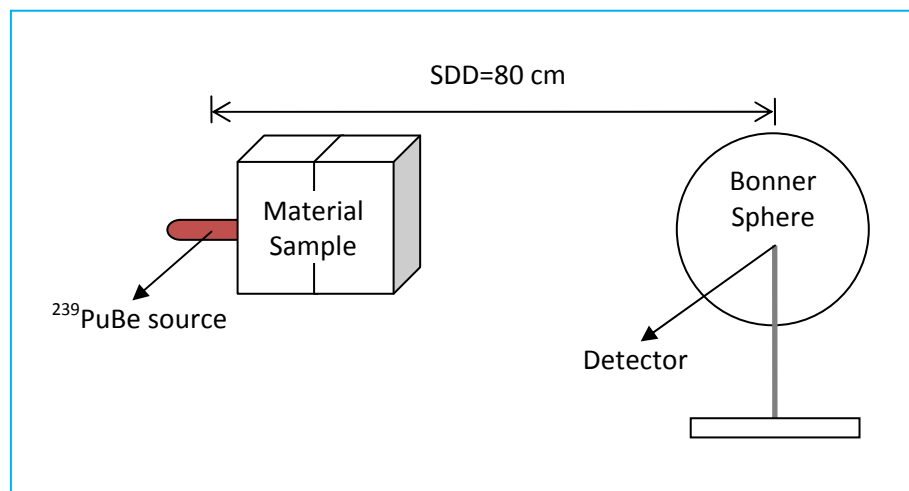


**Figure 2.2** A schematic representation of measurement set up. The distance between the $^{239}$PuBe source and the center of Bonner sphere system is 80cm (SDD). Material samples are levitated so that the center of each sample is at the same level as the detector, i.e. the $^6$LiI(Eu) scintillator.

## 2.2.1.1    Calculations of Tenth Value Layer (TVL)

The data were unfolded using a Fortran code (BONABS) to reconstruct the neutron fluence spectrum and calculate the ambient neutron dose equivalent. [44]  The neutron dose equivalent rates as a function of material thickness were plotted to generate the transmission curves for all materials.  A best power fit line was constructed for each transmission curve.  The tenth value layer (TVL, cm) values of each material were then calculated based on the fitting parameters of the transmission curves.

The calculation was based on the transmission method which was used experimentally for determination of the neutron effective macroscopic removal cross section ($\Sigma_R$, cm$^{-1}$) of a certain material mixture.  The neutron removal cross section ($\Sigma_R$, cm$^{-1}$) took scattering and buildup into account. [36 –37]  In concept, neutron attenuation and absorption in a shielding material can be represented by an exponential function related to shielding material thickness (x, cm) and the neutron removal cross section ($\Sigma_R$, cm$^{-1}$) as shown in equation (2.1).

$$I(x)=I_0\, e^{-\,\Sigma_R x} \quad \text{......} \ (2.1)$$

where $I_0$ and I were the intensity of neutron flux, i.e. the number of neutrons per unit area (n/cm$^2$), before and after passing through the shielding material.  Since for radiation protection, neutron dose equivalent had more significant meaning and the neutron dose equivalent rate (mRem/hr) can be converted from the neutron flux using fluence-to-dose equivalent conversion coefficient provided in the NCRP Report No. 38 (1971, [12]) or ICRP publication 74 (1996, [29]), dose equivalent rate can also be used to determine the neutron removal cross section ($\Sigma_R$, cm$^{-1}$) by replacing the neutron flux intensity in equation (2.1).

The tenth value layer (TVL, cm), was defined as the thickness of the attenuating materials which gave the neutron dose equivalent rate of one tenth of the intensity and can be calculated according to equation (2.2).

$$\text{TVL (cm)} = \frac{Ln(10)}{\Sigma_R} \quad \dotsc\dotsc \text{ (2.2)}$$

## 2.2.2   Monte Carlo Simulations

To calculate the TVL (cm) for each material by MCNPX, neutron fluence per incident neutron ($\Phi(E_n)/n$, cm$^{-2}$) was first calculated when no shielding material was used.  The $\Phi(E_n)/n$ values were then determined with different absorbing material thickness for each sample.  The incident neutron source was simulated as a cylindrical volume source with a length of 13.0 cm and diameter of 2.5 cm.  The energy distribution was modeled based on the neutron spectrum given in Griffin *et al*, (2008, [41]), as seen in Figure 2.1.  The cylindrical source was set to have an isotropic distribution profile in space.  Each calculation was simulated with $1\times10^8$ neutron histories to obtain less than a 0.05 % statistical relative error.  The simulation space was a sphere with a radius of 100 cm.

Neutron fluence per incident neutron, $\Phi(E_n)/n$, was tallied in an air filled spherical receptor in 100 logarithmically spaced energy bins between 0.01 eV and 100 MeV. The neutron receptor had a diameter of 12 cm and was located 80 cm away from the center of neutron source.  Using the energy dependent flux-to-dose equivalent rate conversion coefficient ($h_{\Phi_E}$, mrem/hr) from the NCRP Report No. 38 (1971 [12]), the obtained $\Phi(E_n)/n$ in each energy bin was then converted to energy weighted neutron dose equivalent rate ($H(E_n)/n$) according equation (2.3).

$$H(E_n)_i/n = h_{\Phi}(E_n)_i \cdot \Phi(E_n)_i \cdot d(E_n)_i \quad \cdots\cdots \text{ (2.3)}$$

Where $(E_n)_i$ is maximum neutron energy of the ith energy bin and $d(E_n)_i$ is the ith neutron energy interval.  The total neutron dose equivalent rate per incident neutron (H/n) was then calculated by summing all values obtained in all energy bins according equation (2.4).

$$H/n = \sum_{i=1}^{m} H(E_n)_i/n \quad \cdots\cdots \text{ (2.4)}$$

where m is the total number of energy bins.

Similar to the method used in measurements, the total neutron dose equivalents rates per incident neutron were plotted as a function of absorbing material thickness to generate the transmission curves.  The TVL (cm) values of each material were then calculated based on the neutron removal cross section ($\Sigma_R$, $cm^{-1}$) given by the best line fit of each transmission curve using equation (2.2).

Shielding materials were assumed to be homogeneous mixtures in all simulations.  Since the compositions for all materials used in measurements were not available, the compositions used for Monte Carlo calculations were obtained from the literature. [45 – 47]  The materials selections were based on the material densities due to the limitation data available in the literature.  Table 2.3 lists the compositions and densities of materials that were selected for simulation.  For samples A – C, though they had different physical densities, but considering that they were composed of the same aggregates, one material composition was used to simulate these three samples.  One advantage of using the same material for sample A – C was that the effect of sample geometry was revealed.

**Table 2.3**    Compositions of all materials selected for sample A – G to be used in simulations. Literature materials selection is based on the physical densities of the samples used in measurements.

| Sample # | A – C | D | E | F | G |
|---|---|---|---|---|---|
| Materials from literature | concrete, iron-limonite | concrete, magnetite and steel | ordinary concrete (NIST) | stainless steel-304 | 5% borated polyethylene |
| density | 4.27 | 4.64 | 2.30 | 7.92 | 0.95 |
| element | element weight fraction | | | | |
| H | 0.0005 | 0.002374 | 0.022100 | | 0.116 |
| B | | | | | 0.050 |
| C | | | 0.002484 | | 0.612 |
| O | 0.1800 | 0.137678 | 0.574930 | | 0.222 |
| Na | | | 0.015208 | | |
| Mg | 0.0020 | 0.003669 | 0.001266 | | |
| Al | 0.0050 | 0.010358 | 0.019953 | | |
| Si | 0.0140 | 0.015753 | 0.304627 | | |
| S | 0.0010 | | | | |
| K | | | 0.010045 | | |
| Ca | 0.0610 | 0.055675 | 0.042951 | | |
| Ti | | | | | |
| V | | 0.015969 | | | |
| Cr | | | | 0.190 | |
| Mn | 0.0160 | 0.000647 | | 0.020 | |
| Fe | 0.7210 | 0.757877 | 0.006435 | 0.695 | |
| Ni | | | | 0.095 | |
| references | [45] | [46] | [45] | [45] | [47] |

## 2.2.2.1    Calculations of Tenth Value Layer (TVL) with Different Material Compositions

In light of the fact that the effectiveness of concretes attenuating neutrons were highly dependent on their hydrogenous contents; and concretes with different compositions could result in the same density, additional simulations were carried out to investigate the influence of hydrogen and iron content on TVL values.  Four additional high density concretes of densities ranging from 4.27 to 5.9 g/cm$^3$ were used to repeat the calculations for sample A.  These concrete compositions are listed in Table 2.4.   For regular density concretes, three different materials with densities of 2.3 and 2.35 g/cm$^3$ were used for sample E calculations as shown in Table 2.5.

**Table 2.4**　The compositions of four high densities concretes used to repeat calculations for sample A.

| Materials | concrete, iron-limonite | concrete, magnetite and steel | concrete-MO | concrete, iron-Portland |
|---|---|---|---|---|
| Density (g/cm$^3$) | 4.27 | 4.64 | 5.50 | 5.90 |
| element | element weight fraction | | | |
| H | 0.000500 | 0.002374 | 0.005 | 0.003321 |
| O | 0.179910 | 0.137678 | 0.060 | 0.058563 |
| Mg | 0.001999 | 0.003669 | 0.037 | 0.001308 |
| Al | 0.004998 | 0.010358 | | 0.003320 |
| Si | 0.013993 | 0.015753 | | 0.009157 |
| S | 0.001000 | | | 0.000503 |
| Cl | | | 0.013 | |
| Ca | 0.060970 | 0.055675 | | 0.039847 |
| Ti | | 0.015969 | | |
| V | | 0.000647 | | |
| Mn | 0.01599 | | 0.004 | 0.003522 |
| Fe | 0.72064 | 0.757877 | 0.881 | 0.880459 |
| references | [46] | [46] | [46] | [46] |

**Table 2.5**　The compositions of three additional regular density concretes used for sample E calculations.

| Materials | regular concrete | ordinary concrete (NBS 03) | ordinary concrete (NBS 04) |
|---|---|---|---|
| Density (g/cm$^3$) | 2.30 | 2.35 | 2.35 |
| element | element weight fraction | | |
| H | 0.010 | 0.008485 | 0.005558 |
| C | | 0.050064 | |
| O | 0.532 | 0.473483 | 0.498076 |
| Na | 0.029 | | 0.017101 |
| Mg | | 0.024183 | 0.002565 |
| Al | 0.034 | 0.036063 | 0.045746 |
| Si | 0.337 | 0.145100 | 0.315092 |
| Si | | 0.002970 | 0.001283 |
| K | | 0.001697 | 0.019239 |
| Ca | 0.044 | 0.246924 | 0.082941 |
| Fe | 0.014 | 0.011031 | 0.012399 |
| references | [46] | [46] | [46] |

## 2.3    Results and Discussion

### 2.3.1    Measured Tenth Value Layers (TVL) for Various Materials

The measured neutron transmission curves of each material are shown in Figure 2.3, where the ratios of measured neutron dose equivalent rate (H, mrem/hr) were plotted as a function of shielding material thickness.  Neutron removal cross sections ($\Sigma_R$, cm$^{-1}$) given by the best fitting equations of the transmission curves were used to calculate TVL and the results were listed in Table 2.6.   The results indicated that materials with higher densities were more effective, especially in the case of high density concretes vs. regular density concretes.   This feature is preferred for environments possessing limited space.

The measured TVL values of the high density concretes that were designed specifically for shielding around the proton facility at WUSM, i.e. sample A – C, ranged from 46.7 to 57.7 cm. The discrepancies may be due to the composition differences among the material samples. Since these three samples were made separately using local aggregates, the amount of iron ore in such small sample sizes may not be consistent.   The other possible reason for the discrepancies may also be due to the geometry and sizes of the samples.  Because the neutron source used in the measurements was not well collimated, the differences in samples geometry and size would affect the measured neutron equivalent dose rates.  This effect was clear seen in the simulated TVL values where the same material compositions were used for sample A – C. The simulated TVL values were also were included in Table 2.6.

The highest measured TVL value was found to be the regular density concrete. Although higher TVL values were expected when comparing to high density concretes (HDC), the nearly as twice as much of the TVL vales in HDC, might be due the fact that the concretes used for measurements were old concrete blocks from the University of Missouri Research Reactor

(MURR). Since the hydrogenous content in concrete might decrease over time, a higher TVL value was expected.

The measured TVL values were also compared to the TVL values used for the analytical shielding calculations [48] and are also shown in Table 2.6. The TVL values were based on 90° scatter from a 250 MeV source [49]. These results were derived from reports using measurements. However, since the neutron energy and the neutron flux were much lower for the [239]PuBe source than for the neutrons expected from the high energy proton facility, the measured TVL values were expected to be much lower than the data presented in Table 2.6.

**Table 2.6**     Tenth values layer (TVL) values of various materials obtained by measurements and Monte Carlo simulations are presented. Where $\Sigma_R$ $(cm^{-1})$ is the neutron removal cross section. Materials densities listed under measurement were the physical densities for each material; whereas the densities listed under Monte Carlo simulation were the densities of materials selected for simulations. The TVL values listed under the analytical shielding calculation were the values obtained from the proton facility shielding report.

| Sample # | A | B | C | D | E | F | G |
|---|---|---|---|---|---|---|---|
| Materials | HDC | HDC | HDC | HDC | RDC | S | BPE |
| Measurement (using PuBe source) | | | | | | | |
| Density (g/cm$^3$) | 4.27 | 3.70 | 2.89 | 4.80 | 2.35 | 7.75 | 1.08 |
| $\Sigma_R$ (cm$^{-1}$) | 0.0493 | 0.0399 | 0.0434 | 0.0516 | 0.0295 | 0.0561 | 0.0331 |
| TVL (cm) | 46.7 | 57.7 | 53.1 | 44.6 | 78.1 | 41.0 | 69.6 |
| Monte Carlo simulation (using PuBe source) | | | | | | | |
| Density (g/cm$^3$) | 4.27 | 4.27 | 4.27 | 4.64 | 2.3 | 7.92 | 0.95 |
| TVL (cm) | 84.7 | 27.5 | 19.8 | 39.2 | 27.9 | 21.7 | 18.7 |
| Analytical shielding calculation (for 250 MeV source) [48] | | | | | | | |
| TVL (cm) | 52.4 | NA[a] | NA | NA | 85.6 | 36.2 | NA |

a. NA = data not available
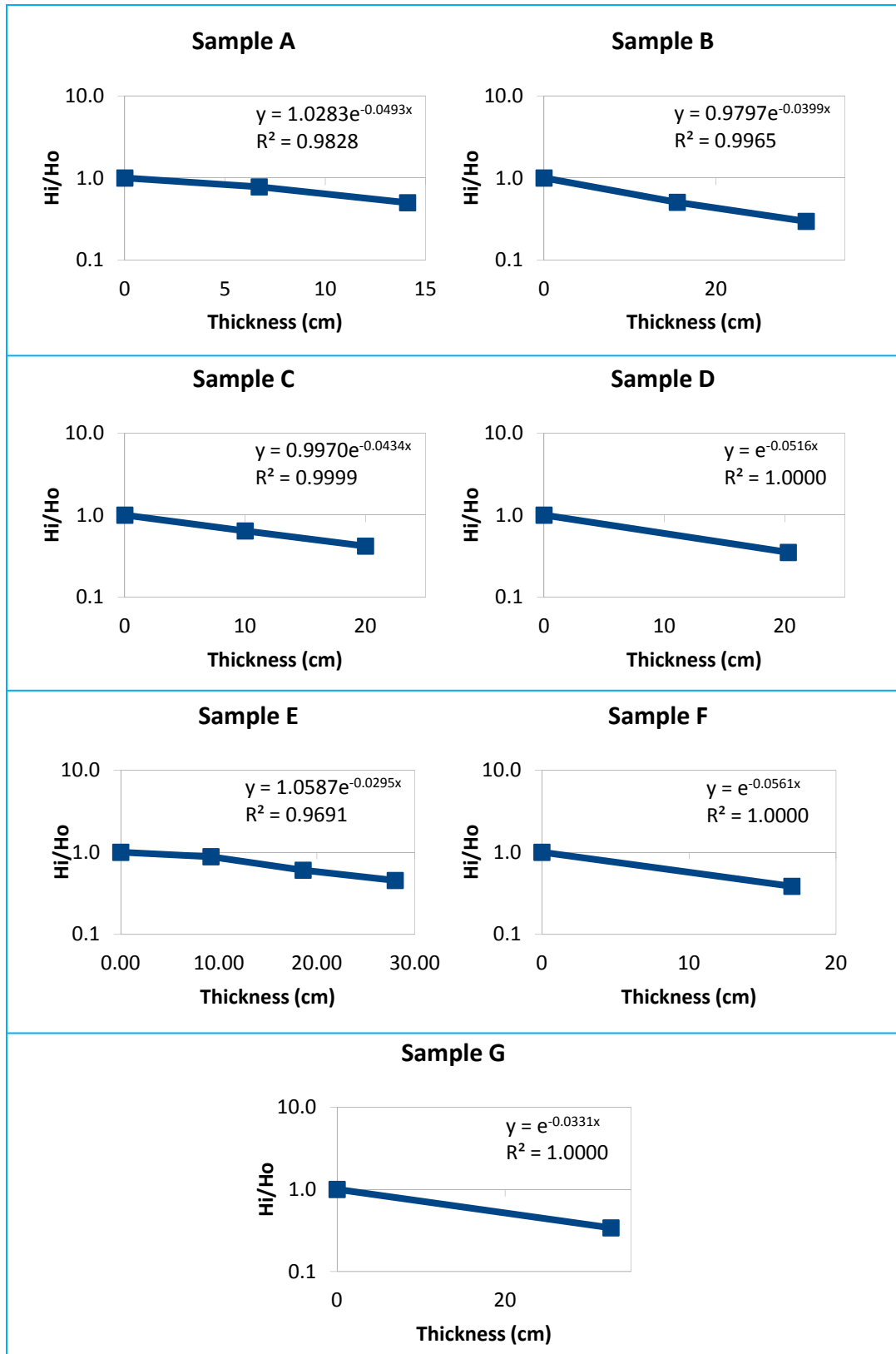
**Figure 2.3** Measured transmission curves of various materials. Where Hi is the ith dose equivalent rate (H, mrem/hr), and Ho is the dose equivalent rate obtained with no shielding present.

24

## 2.3.2    Influence of Surrounding Walls on TVL Values

Since most of the measured TVL values were higher than the Monte Carlo simulated results, additional MC calculations were performed to evaluate the influence of the surrounding walls.  Three walls were included as seen in Figure 2.4; including the floor, the wall behind the neutron detector, and the side wall closest to the measurement set up.  The distances between the walls and the source were estimated to be 1 m, 3 m and 2 m for the floor, the back wall and the side wall respectively.  The walls were simulated with 12 inch thick ordinary concrete as specified in Table 2.3 (E).
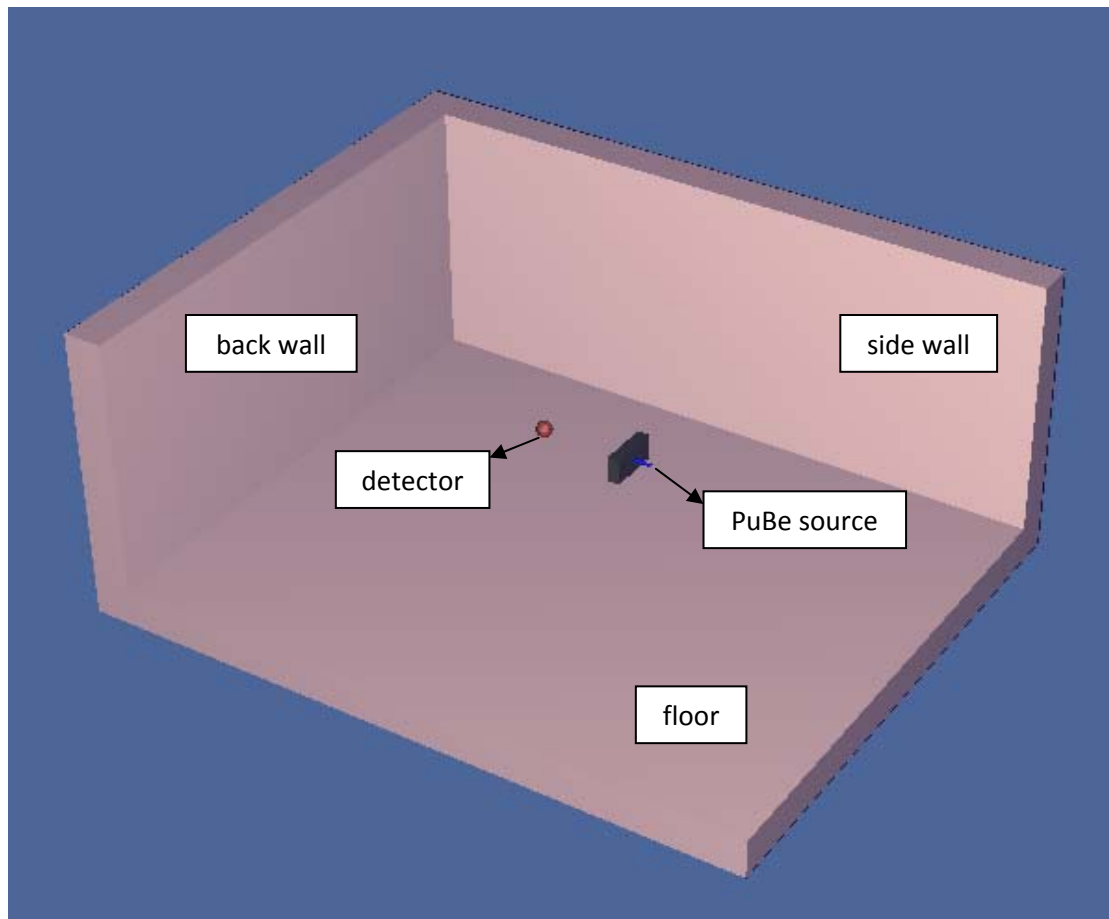


**Figure 2.4**    Schematic presentation of measurement set up with the present of surrounding walls.

The results are listed in Table 2.7.  The TVL values calculated with surrounding walls present were all higher compared to the values excluding the surrounding walls.  The percent differences due to the present of surrounding walls were ranging from 13.7 % to 33.7 %.  The higher TVL values when calculated with surrounding walls present suggested that the material sample sizes might be too small so that a fraction of neutrons did not go through the samples but rather to the walls and subsequently scattered back to the detector.

**Table 2.7**    Simulated tenth values layer (TVL) values of various materials calculated with and without surrounding walls present. Materials densities listed were the densities of materials selected for simulations.

| Sample # | A | B | C | D | E | F | G |
|---|---|---|---|---|---|---|---|
| Materials | HDC | HDC | HDC | HDC | RDC | S | BPE |
| Density (g/cm$^3$) | 4.27 | 4.27 | 4.27 | 4.64 | 2.3 | 7.92 | 0.95 |
| No surrounding walls | | | | | | | |
| TVL (cm) | 84.7 | 27.5 | 19.8 | 39.2 | 27.9 | 21.7 | 18.7 |
| With surrounding walls | | | | | | | |
| TVL (cm) | 103.7 | 35.1 | 25.3 | 45.4 | 32.5 | 26.3 | 28.2 |
| difference | 18.3 % | 21.7 % | 21.7 % | 13.7 % | 14.2 % | 17.5 % | 33.7 % |

## 2.3.3    Influences of Hydrogen Content and Concrete Density on TVL Values

Additional simulations were performed for both sample A, a high density concrete, and sample E, a regular density concrete, using different material compositions.  The results are shown in Table 2.8 and 2.9 respectively.

The results showed that the TVL values decreased with increasing hydrogen content in both high density and regular density concretes.  Higher concentrations of iron did not seem to affect the TVL values.  This might because the incident neutrons mean energy was 4.83 MeV so that the advantageous of using high density concrete was not significant.

**Table 2.8**   The simulated TVL values of four high densities concretes used to repeat calculations for sample A.

| Materials | concrete, iron-limonite | concrete, magnetite and steel | concrete-MO | concrete, iron-Portland |
|---|---|---|---|---|
| Density (g/cm$^3$) | 4.27 | 4.64 | 5.50 | 5.90 |
| Element | element weight fraction | | | |
| H | 0.000500 | 0.002374 | 0.005 | 0.003321 |
| Fe | 0.720640 | 0.757877 | 0.881 | 0.880459 |
| other | 0.027886 | 0.239749 | 0.114 | 0.116220 |
| TVL (cm) | 83.4 | 66.6 | 46.5 | 49.6 |

**Table 2.9**   The simulated TVL values of three additional regular density concretes used for sample E calculations.

| Materials | regular concrete | ordinary concrete (NBS 03) | ordinary concrete (NBS 04) |
|---|---|---|---|
| Density (g/cm$^3$) | 2.30 | 2.35 | 2.35 |
| element | element weight fraction | | |
| H | 0.010 | 0.008485 | 0.005558 |
| Fe | 0.014 | 0.011031 | 0.012399 |
| other | 0.976 | 0.980484 | 0.982943 |
| TVL (cm) | 37.8 | 37.9 | 42.8 |

### 2.3.4    Outcome of Specific Aim and the Coherence with Literature

The goal of this work was to estimate the effectiveness of various shielding materials for shielding the proton facility at WUSM.  Based on the measurements taken and the results of the Monte Carlo simulations, high densities concretes with sufficient hydrogen concentrations were the most effective materials in shielding neutrons.  As the amount of hydrogenous materials within the concrete increased, the significance increased.  This was in agreement with Abdo (2002, [37]) and Kharita *et al* (2008, [40]).

### 2.3.5    Strengths and Limitations of This Study

Since the ores and aggregates used to mix the high density concretes were obtained locally, this study provided overall information on the attenuation properties of the local high density concretes used in neutron shielding.  Although the neutron source used in the study was much weaker than the neutrons generated from the high energy proton beam, these measurements provide a valid surrogate for the neutron flux and attenuation walls.  In addition, since the cost of making and using high density concretes were higher than using regular density concretes, this study increased the confidence level to use high density concrete.

However, inadequate information on the actual concrete material compositions limited the Monte Carlo calculation in determining the tenth value layer (TVL) needed for shielding the high energy neutrons generated in the proton facility.  Moreover, since all measurements were conducted at a reactor where other radiation sources, although minimal in activity, were also present.  Also, one slab sample of each material was not sufficient to collimate the neuron

source and prevent the scattering from the surrounding walls in the reactor. The differences in materials' dimensions and geometries increased the uncertainty in the TVL results.

## 2.4    Conclusions

Several materials related to neutron shielding were investigated with measurements and Monte Carlo simulations. Both measurement and Monte Carlo calculations show that concrete with higher hydrogen concentrations were better in attenuating neutrons. High density concretes are more suitable if the neutron sources possess high energy. To attenuate the thermal neutrons that are generated after slowing down fast neutrons by the high density materials, materials with a high content of hydrogen are preferred. Therefore, high density concretes with high hydrogenous content are more suitable especially for space-restricted environment.

# CHAPTER 3

# NEUTRON PRODUCTION FROM ELECTRON LINEAR ACCELERATORS

This chapter focuses on the second specific aim stated in chapter 1. An introduction to the neutron production from electron linear accelerators and the neutron sources is given. The methods and materials special to this chapter are described, followed by the results and discussions.

Specific Aim 2: Compare neutron productions from two conventional linear accelerators: Varian and Elekta.

Hypothesis: The Elekta accelerator produces less secondary neutron dose due to an additional filter structure in the beam line.

## 3.1    Introduction

Since the discovery of the x-ray in 1895, therapeutic radiation has been used as a tool for cancer treatments. For most patients receiving external beam radiation, photon therapy is the current standard treatment option. Therapeutic photon beams are produced in the electron linear accelerators (linacs) and depending on the models, with beam energies ranging from 4 MV to 25 MV. It has been found that the interactions of high energy photons with the linacs head components produce neutrons that could potentially increase unwanted peripheral dose delivered to patients.

### 3.1.1    Neutron Production in Electron Linear Accelerators

In a conventional linear accelerator, electrons are accelerated through a high frequency electromagnetic waveguide and transported to a treatment head.  This accelerated electron beam can be used as an electron therapy source or can interact with high atomic (high Z) targets to generate bremsstrahlung photons for photon therapy.  When the operating mode is greater than 10 MeV, the generated high energy photon beams are contaminated with neutrons.  These neutrons are produced through photonuclear and electronuclear reactions. [50 – 51]

### 3.1.1.1    Photoneutron Production (γ,n)

The incident electron ($E_i$) interacts with the Coulomb field of nuclide R and gets scattered.  A bremsstrahlung x-ray (photon) with energy $E_\gamma$ is then created to induce a photonuclear reaction in the target A and emits a neutron (n), as shown in Figure 3.1.
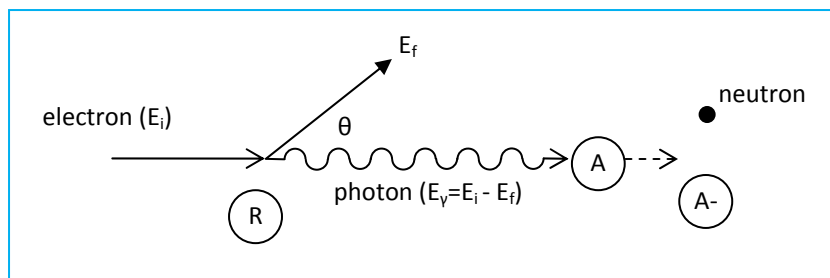


**Figure 3.1**    Illustration of photonuclear reaction. [51]

The photonuclear reaction only occurs if the photon energy is at least equal to the binding energy (BE) of the neutron in the target nucleus.  When the energy excesses the

31

threshold of such binding energy, the cross section of photonuclear reaction has a Maxwell-Bolzmann distribution and is known as giant dipole resonance region. Within the giant dipole resonance region, both evaporation and direct neutrons are contributed to the neutron spectrum. Evaporation neutrons emission is isotropical where as the direct neutrons emission follows a $\sin^2\theta$ angular distribution, where $\theta$ is the angle between the emitted neutron and the incident photon. Photons with higher energy have more direct neutrons. [52] The cross section depends on both the atomic number and abundance of element. Table 3.1 lists the common photoneutron sources and their binding energies of the neutrons in conventional linear accelerators.

**Table 3.1**      Photoneutron sources in the conventional linear accelerators.[51]

| Element | Mass Number | Relative Abundance | BE of neutron (MeV) |
|---------|-------------|--------------------|--------------------|
|         | 54          | 5.8                | 13.38              |
| Fe      | 56          | 91.7               | 11.19              |
|         | 57          | 2.1                | 7.65               |
|         | 58          | 0.2                | 10.04              |
| Cu      | 63          | 69.2               | 10.85              |
|         | 65          | 30.8               | 9.91               |
|         | 180         | 0.1                | 8.41               |
|         | 182         | 26.3               | 8.06               |
| W       | 183         | 14.3               | 6.19               |
|         | 184         | 30.6               | 7.41               |
|         | 186         | 28.6               | 7.20               |
|         | 204         | 1.4                | 8.4                |
| Pb      | 206         | 24.1               | 8.09               |
|         | 207         | 22.1               | 6.74               |
|         | 208         | 0.2                | 7.37               |

### 3.1.1.2    Electroneutron Production (e, e'n)

The electroneutron production is illustrated in Figure 3.2.  The incident electron ($E_i$) scatters through the Coulomb field of the nuclide A.  Instead of emitting a photon, the resulting virtual photon ($E_v$) interacts directly with the nucleus.  The cross sections of interaction for direct electron interactions with the nuclei is approximately 137 times smaller than the cross sections of photonuclear reaction; thus, its contribution to neutron contamination in conventional linear accelerator is small. [50-51]
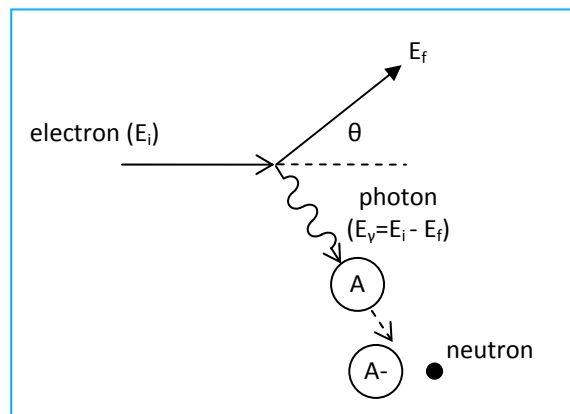


**Figure 3.2**    Illustration of electronuclear reaction. [51]

### 3.1.1.3    Neutron Sources

In an electron linear accelerator, neutrons are generated in the machine head and in patients.  Neutrons generated in the machine head can have energy up to a few MeV depending on the incident electron energy and the type of the target used in the accelerator.  These neutrons can be attenuated by the head shielding and have reduced energy.  A fraction of neutrons reached the treatment vault can be scattered back to the treatment plane.  [53 – 54]

In general, at the isocenter, the neutron fluence ($\Phi$, n/cm$^2$) per unit photon dose (Gy) can be describe as follows [55],

$$\Phi = \Phi_{dir} + \Phi_{sc} + \Phi_{th} \cdots\cdots (3.1)$$

where $\Phi_{dir}$ is the direct neutron fluence, $\Phi_{sc}$ is the scatter neutron fluence, and $\Phi_{th}$ is the thermal neutron fluence. The direct neutron fluence is proportional to inverse square of the distance between the measurement point and the target. Both scatter neutron fluence and thermal neutron fluence are proportional to the treatment room area.

Many studies have investigated the neutron productions in the treatment vaults and in patients for different electron linear accelerators. Kase *et al*. (1998, [50]) studied the neutron influence for the 10, 15, 18 and 20 MV photon beams generated by the Varian Clinac 2100/2300C using the EGS4 code coupled with the MORSE code. Two different geometries were used, including an actual geometry (85 body geometry) and a simplified spherical geometry. They reported a factor of 2 difference from these two geometries. The neutron fluences at the isocenter were $3.8 \times 10^{10}$ and $1.2 \times 10^{12}$ neutrons per Gy for the 10 MV and 18 MV photon beams, respectively. They also reported that the average neutron energy ranged from 0.04 – 0.49 MeV inside the concrete room.

Chibani *et al.* (2003, [56]) studied the dose from photon-induced nuclear particles generated by high energy photon beam for Siemens and Varian linacs. They reported the total dose equivalent ratio (DER) attributed to the neutrons, photons and alpha particles was 0.66 cSv/Gy for the Siemens 18 MV photon beam (10 × 10 cm$^2$ field size). The DER for the Varian 15 MV and 18 MV were 1.52 and 2.86 cSv/Gy respectively (10 × 10 cm$^2$ field size).

Ongaro *et al.* (2000, [57]) using MCNP-GN code, simulated the neutron production from the 18 MV photon beam generated by the SL20I-Elekta equipped with a multileaf collimator system and 15 MV beam generated by the Metatron Siemens. They reported that depending on the accelerator characteristics and distance from the isocenter, the neutron dose equivalent was between 1 and 4.8 mSv/Gy for a $10 \times 10$ cm$^2$ field at 100 cm SSD.

Ipe *et al.* (2000, [58]) measured the neutron dose equivalents for a 15 MV beam around a Varian Clinac 2300C/D. They reported that for a $20 \times 20$ cm$^2$ field, the measured neutron dose at isocenter using bubble detectors, gold foil activation and track-etch dosimeters were 0.025, 0.03 and 0.085 mSv/MU respectively.

Paredes *et al.* (1999, [59]) used CR-39 track etch detectors to measure the neutron dose for the 18 MV beam around a Varian 2100C. They reported that for a $20 \times 20$ cm$^2$ field at 100 cm SSD, the average neutron dose was 2.3 mSv per 200 cGy beam delivered. Kry *et al.* (2008, [60]) investigated the influence of the flattering filter on the neutron dose for a Varian 21EX Cliniac 18 MV beam. They reported the ambient neutron dose equivalents were $2.31 \times 10^{-5}$ Sv/MU with the flattening filter present and $1.65 \times 10^{-5}$ Sv/MU without the flattening filter.

## 3.1.2 The Varian IX and the Elekta Precise Linear Accelerators

As mentioned before, the therapeutic photon beams are generated by bombarding the target with accelerated electron beams. These generated photons are collimated initially by a primary collimator. The photons then go through flattening filters which are designed to attenuate photon fluence and generate flat dose distributions at 10 cm depth in water. The ionization chambers are used to monitor the dose rate, integral dose and field symmetry. After

the photon beams pass through the monitor chambers, they are further collimated by collimators which allow for rectangular field sizes ranging from 0 × 0 to 40 × 40 cm$^2$ at the isocenter.  Multileaf collimators (MLC) and wedges are used to further shape the beam to fit the treatment target. [61–62]  Although the basic principle of designing a electron linear accelerator is the same, different manufacturers have different approaches for achieving the desired photon strengths needed for clinical use.

Figure 3.3 illustrates 18 MV beamline of two electron linear accelerators, Varian (Varian Medical Systems, Palo Alto, CA) and Elekta (Elekta Inc, Norcross, GA), which shows the components of common neutron sources.  [63 – 64]
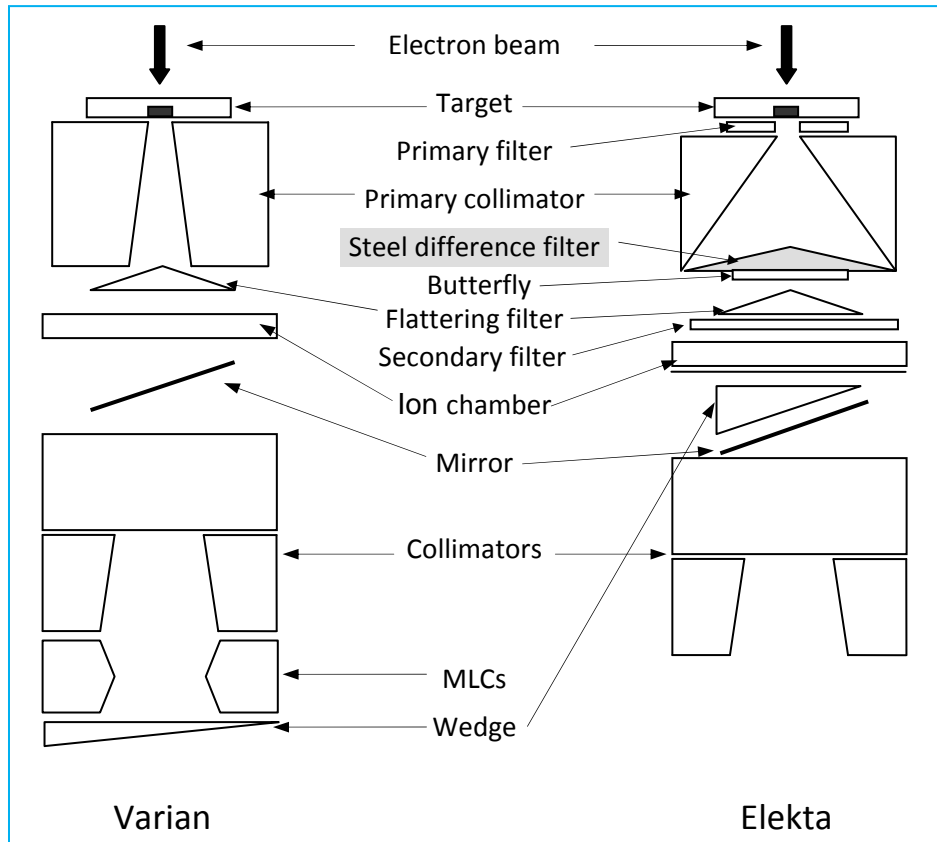


**Figure 3.3**    The schematic of 18 MV photon beamline for Varian IX and Elekta Precise accelerators. [63 – 64]

## 3.2    Methods and Materials

The neutron dose equivalents at various locations for two photon energy beam, i.e. 10 MV and 18 MV were determined experimentally for both the Varian IX and Elekta Precise linear accelerators and compared with Monte Carlo calculations.

A neutron rem meter (Model-5085 Meridian, Far West Technology Inc., Goleta, CA) was used in this study.  This neutron meter utilized a $BF_3$ proportional counter for thermal neutron detection.  The neutron responding curve of the Meridian rem meter is shown in Figure 3.4. [65] Two operating modes were available with this detector, including dose rate and integral dose measurement.
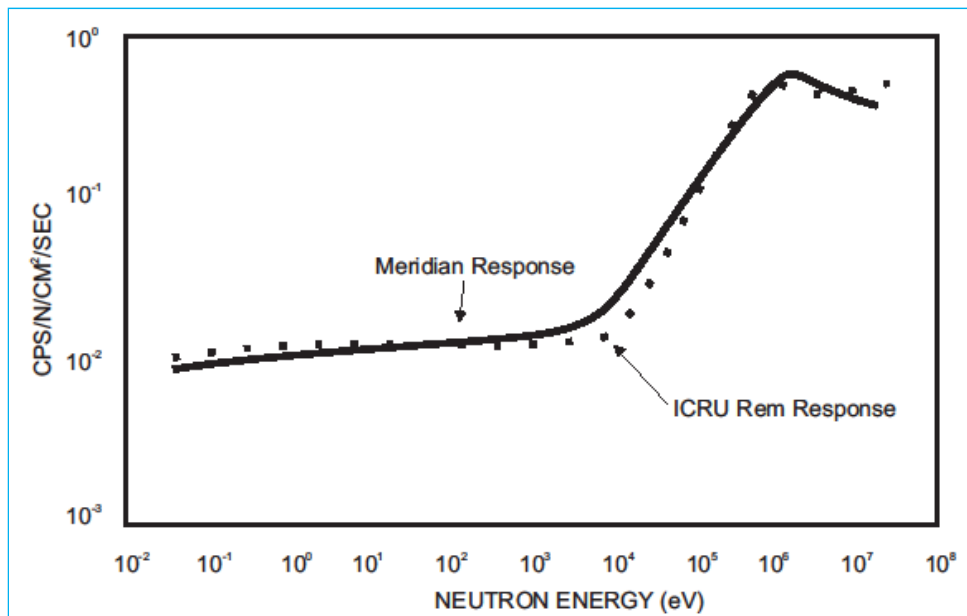


**Figure 3.4**      The neutron responding curve of the Meridian rem meter.  [65]

The neutron meter was set to discriminate gamma rays for all measurements. The neutron dose equivalents were measured for both 10MV and 18MV photon beams with the multileaf collimators (MLCs) fully retracted. A total dose of 200 MU was delivered at a rate of 100MU/min to acquire measurements at various locations. In this study, the neutron dose equivalents were measured as a function of field sizes, including $0 \times 0$, $5 \times 5$, $10 \times 10$, $20 \times 20$, $30 \times 30$ and $40 \times 40$ cm$^2$ fields. The neutron dose equivalents were also determined as a function of gantry angle, including 0°, 90°, 180° and 270°.

A schematic diagram of the measurement setup is shown in Figure 3.5. For different field sizes, the neutron meter was place on the treatment couch at a source to axis distance (SAD) of 100 cm and 50 cm away from the gantry isocenter; and the gantry angle was set to be 180°. For different gantry angle, the neutron meter was place at distances of 90 cm away from the isocente, and the field size was a $0 \times 0$ cm$^2$ field.
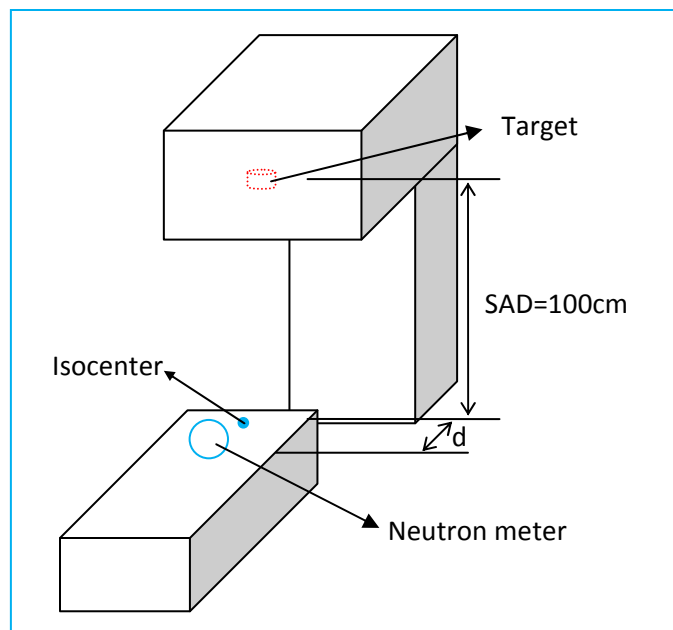


**Figure 3.5** Schematic drawing of the measurements setup. Where d is the distance between the neutron meter and the isocenter.

## 3.3    Results and Discussion

### 3.3.1     Neutron Dose Equivalent as a Fuction of Field Size

Neutron dose equivalents (H, mrem) for different field sizes are listed in Table 3.2 and plotted in Figure 3.6.  The measured neutron dose equivalents for the Elekta photon beams were significantly lower than those for the Varian linear accelerators.  The H values increased as the field size at the isocenter decreased.  This was due to the fact that as the field sizes became smaller, the incident photon beams encounter a large surface area of the jaws, which are made of tungsten alloy.

**Table 3.2**      Measured neutron dose equivalents (H) as a function of field size. The neutron meter is at 50 cm away from the isocenter and the gantry angle is 180°.

| Field size (cm$^2$) | Varian IX | | Elekta Precise | |
|---|---|---|---|---|
| | H (mrem) for 18 MV | H (mrem) for 10MV | H (mrem) for 18MV | H (mrem) for 10MV |
| 0×0 | 1.48 | 1.11 | 0.727 | 0.682 |
| 10×10 | 1.51 | 0.684 | 0.720 | 0.489 |
| 20×20 | 1.50 | 0.415 | 0.689 | 0.305 |
| 30×30 | 1.43 | 0.367 | 0.634 | 0.265 |
| 40×40 | 1.35 | 0.338 | 0.578 | 0.240 |
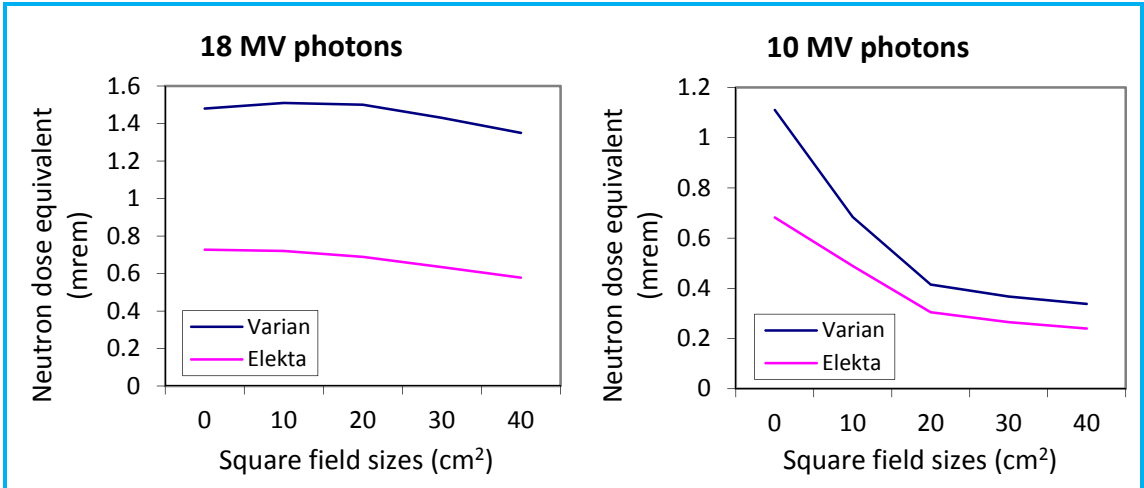
**Figure 3.6** The measured neutron dose equivalents as a function of field sizes. The neutron meter is at 50 cm away from the isocenter and the gantry angle is 180°. (See Figure 3.5)

## 3.3.2    Neutron Dose Equivalent as a Fuction of Gantry Angle

Measured neutron dose equivalents for different gantry angles are listed in Table 3.3 and plotted in Figure 3.7.   The results showed that the neutron dose equivalent was independent of the gantry angle.

**Table 3.3** Neutron dose equivalents (H) as a function of gantry angle. The neutron meter is at 90 cm away from the isocenter and the field size is 10×10 cm$^2$. (See Figure 3.5)

| | Varian IX | | Elekta Precise | |
|---|---|---|---|---|
| Gantry angle (°) | H (mrem) for 18 MV | H (mrem) for 10MV | H (mrem) for 18MV | H (mrem) for 10MV |
| 0 | 1.40 | 1.15 | 0.729 | 0.722 |
| 90 | 1.48 | 1.18 | 0.749 | 0.645 |
| 180 | 1.51 | 1.15 | 0.723 | 0.635 |
| 270 | 1.51 | 1.09 | 0.707 | 0.614 |
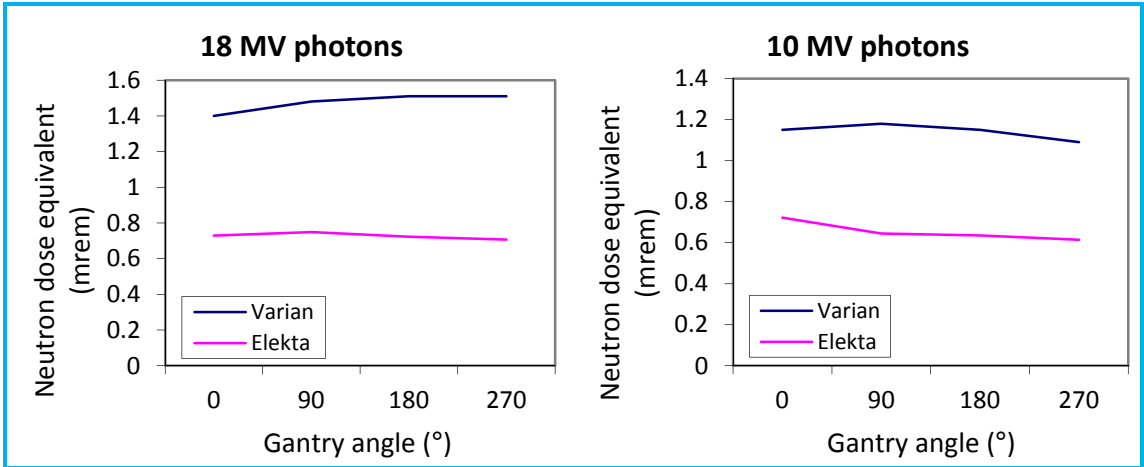
**Figure 3.7** The measured neutron dose equivalents as a function of gantry angles. The neutron meter is at 90 cm away from the isocenter and the field size is 10×10 cm$^2$. (See Figure 3.5)

For 18 MV photons, the ratio of the measured H values for two linear accelerators was nearly a factor of two in favor of the Elekta accelerator. This was likely due to the difference in beamline design (Figure 3.3). An additional steel filter was used in the Elekta beamline acts as a neutron absorber thus the lower neutron dose equivalents.

### 3.3.3 Outcome of Specific Aim and the Coherence with Literature

The goal of this chapter was to evaluate the neutron production from the two models of electron linear accelerators that were used for delivering 10 MV and 18 MV photon beams. Through the measurement method, the neutron dose equivalents (H, mrem) at the 50 cm away from the isocenter on the patient axis was found to be increased as the field sizes increased. H values were independent of the gantry angle. Neutron dose equivalents in the literature vary with parameters such as neutron detector locations and collimated field sizes, and the units of the reported results also varies. It is difficult to compare the results in this work with literature. However, the neutron dose equivalents in this work fall in the range of the data reported in the literature.

### 3.3.4    Strengths and Limitations of This Study

The work provides basic neutron production information from the two models of electron linear accelerators available in the Department of Radiation Oncology in WUSM. The measurement data indicates the neutron dose equivalents from Elekta are much lower than from Varian. This difference is especially significant for the 18 MV photon beams. It is suspected the difference is the result of the steel difference filter included in the Elekta linear accelerator. To confirm this, Monte Carlo calculations are being investigated.

### 3.4    Conclusions

Neutron dose equivalents (H, mrem) for the Varian and Elekta photon beams were measured and compared. Higher H values were found in the Varian linear accelerator, especially for the 18 MV photon beam. In general, neutron dose equivalents decreased as the field size increased. Neutron dose equivalents were found independent of gantry angle.

# CHAPTER 4

# NEUTRON PRODUCTIONS FROM THE MEVION S250 PROTON ACCELERATOR

This chapter focuses on the third specific aim stated in chapter 1. The principles of proton therapy are described, including delivery techniques and neutron productions from proton accelerators. The methods and materials special to this chapter are described. Finally, the results and discussion are included.

Specific Aim 3: Characterize the neutron production from the MEVION S250 proton accelerator.

Hypothesis: The neutron production from the MEVION S250 proton accelerator is comparable with other existing (passive scattering) proton accelerators.

## 4.1 Introduction and Basic Principles of Proton Therapy

Since the first concept of proton therapy by Wilson (1946 [67]), proton beams have been applied to various cancer sites treatment. [68–73] The advantage of using protons for radiotherapy compared with other techniques, is the capability of delivering highly conformal dose to the target volume due to its unique dose deposition characteristic – the Bragg peak (Figure 4.1 [74]). Because protons have greater masses than electrons, as they travel thorough a medium and slow down by interacting with electrons, they travel in relatively straight paths (a
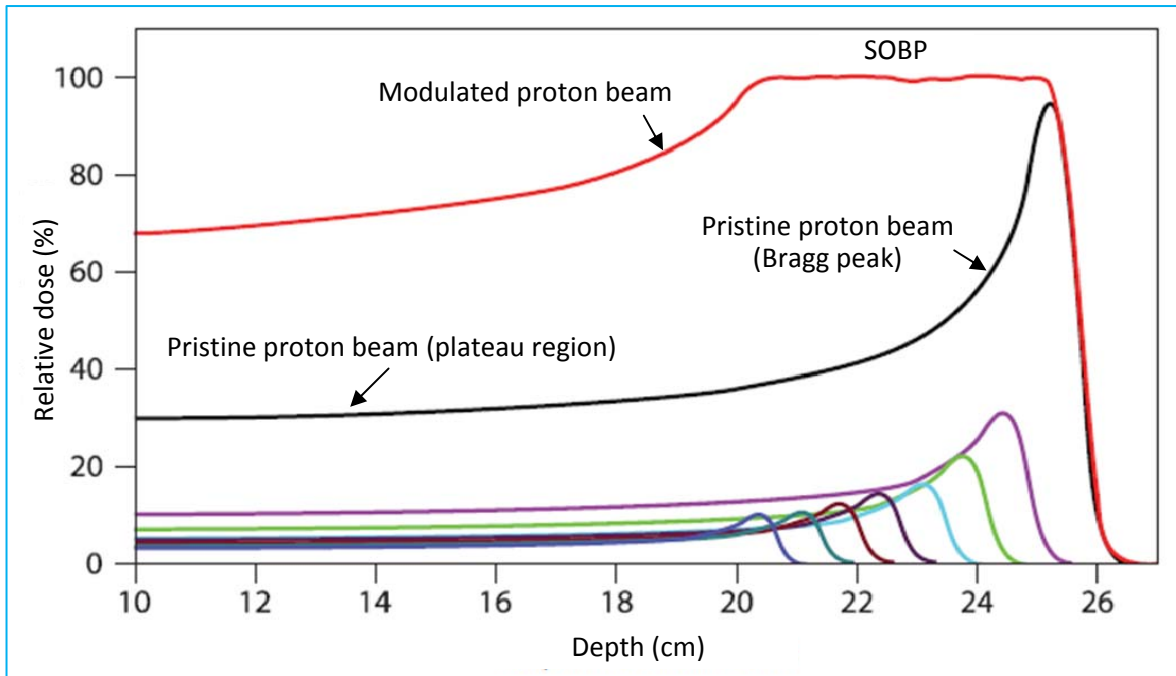
**Figure 4.1**    Central axis depth dose distributions for pristine proton beams and a modulated proton beam (spread out Bragg peak, SOBP). Note: figure is modified from McDonald et al (2010, [74]).

plateau region).  They release most of their energies at the end of the paths known as the Bragg peak region.  The sharp distal falloff after the Bragg peak with the dose approaching zero, allows for sparing normal tissue in the downstream of the beam direction. This dose confinement to the target volume reduces normal tissue complication probability. [75]  Such advantageous attributes of proton therapy not only allow for the potential higher dose delivery, but also increases the probability of local tumor control, and consequently, increased survival of cancer patients. [76]

The potential advantage of protons over other radiotherapy modalities has been discussed for various types of tumors. [77–81]  Historically, the most frequent applications are for the treatment of shallow tumors (ocular) using relative low energy protons, and treatment of deep-seated tumors (prostate) using high energy protons. [82]  Schneider *et al* (2000, [78])

investigated the probability of secondary cancer incidence after radiotherapy for Hodgkin's disease, and reported that proton therapy had a lower cancer incidence than photon therapy. Chang *et al* (2006, [79]) studied dose volume histograms (DVH) in patients with non–small-cell lung cancer and found that the dose to normal tissues was lower for proton treatment when compared with photon therapy. Using a treatment planning comparison method, Steneker *et al* (2006, [81]) investigated treatments for head and neck tumors. They concluded that for the same target dose homogeneity, intensity modulated proton therapy (IMPT) was superior in sparing organs at risk over intensity modulated photon therapy. While passive proton scattering techniques are advantageous compared with photon or electron techniques, IMPT as delivered with multiple spot beams, is even more conformal. Delivery of IMPT relies on moving "spots" of various energies and does not rely of materials to alter the beam. The risk of secondary cancer was found to be lower for the IMPT plans with reduced spot size and small numbers of fields, for which the integral dose in normal tissue was lower.

The ability of proton to deliver a high energy dose to the target and reduce the integral dose to adjacent critical structures has increased the interest in using proton for a variety of treatments.

## 4.1.1    Proton Beam Shaping and Delivery Techniques

An acceptable proton accelerator for radiotherapy requires its maximum beam energy sufficient to penetrate inhomogeneous tissues in the human body. The range of the protons depends on their speed and the materials in which they are absorbed. In order to deliver an adequate dose to the deepest region of the human body, the proton beam has to have a

minimum mean energy around 200 MeV. For different depths of the irradiation sites, the beam energies are adjusted and tuned according to the materials intercepted within the beam path. [83]

Hydrogen gas is a common proton source used for extraction. Protons are separated by introducing a charge differential before entering an accelerator. [84] The accelerated high energy proton beam extracted from a cyclotron or a synchrotron is usually a mono-energetic pencil beam in the beam plane (Bragg peak), and needs to be spread and modulated to become a clinically useful beam (spread out Bragg Peak, SOBP) as shown in Figure 4.1. There are two techniques for spreading the beam and delivering the proton dose uniformly, perpendicular to the beam plane, to the irregular shaped target volume inside a patient: active scanning and passive beam scattering. [85–86]

The active scanning method, also known as spot scanning or voxel scanning, utilizes magnetic fields to deliver the beam across the target volume laterally and in depth. In beam scanning, the region of 100% dose is strictly confined to the target along the pencil beam. Therefore, even for the complex target shape, the reduction of dose deposited to the region outside the target can be achieved. Although active scanning methods provides advantages such as higher flexibility of dose shaping, it requires substantial resources to implement safely and effectively. Another challenge of active scanning methods is the dose delivery volatility due to patient and organ motion. The sensitivity to motion limits the application of scanning method to only well immobilized patients and fixed tumors.

For a passive scattering proton accelerator, a clinical treatment beam is produced by utilizing a series of beam scattering devices in the beam-line to spread the pencil beam and

generate circular uniform field at the isocenter. The MEVION (formally Still River Systems therapy accelerator currently relies strictly on passive scattering.

Figure 4.2 shows a typical passive scatter system using double scattering technique. [87] Double scattering was developed to reduce energy loss and improve efficiency. The first scatterer is used to spread the proton dose in depth. Most often, the first scatterer is composed of high Z (atomic) material, such as lead. This is because high Z materials allow for beam scatter with minimum energy loss. In a double scattering system, the range modulator wheel serves as a first scatterer and a range shifter, and typically is constructed with two different materials to achieve constant scattering as a function of wheel rotation angle. This Gaussian beam profile produced by the first scatterer then is conformed laterally to the target volume using a second scatterer. [88] The second scatterer is also composed of two materials to achieve differential scattering across the beam profile and results in a flat profile near patient. Since passive scattering relies on the sequence of these devices to generate a useful flat proton beam, a drawback of this technique is an increased sensitivity to beam steering that even a slight deviation of the initial beam position could result in a tilted dose distribution.
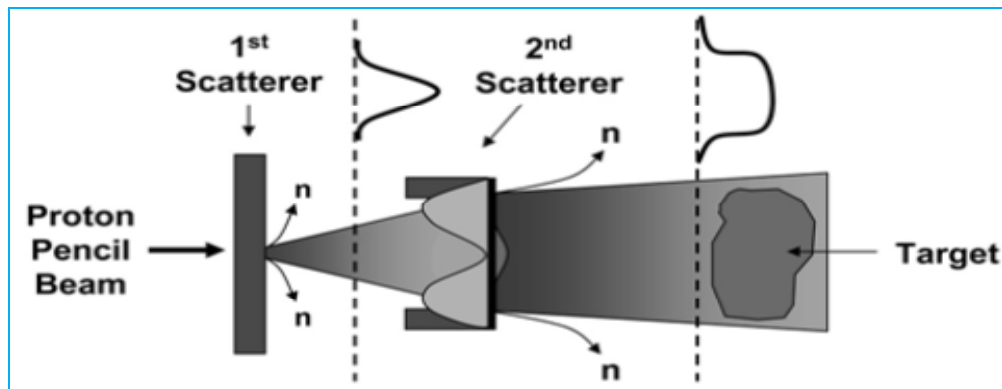


**Figure 4.2** From Hall *et al* (2006), a typical proton delivery system using passive scattering method. [87]

## 4.1.2    Neutron Production in Proton Accelerators

Neutrons are produced primarily when a large numbers of protons lose a significant amount of energy.  As protons leave the accelerator and pass through the beam shaping components in a passive scattering system, a fraction undergo inelastic nuclear reaction with the nucleus and release high energy neutrons and γ-rays.

At energies below ~10 MeV, (p,n) reactions are important sources of neutrons.  For proton energy between 50 and 500 MeV, the neutron yield is proportional to the total proton energy squared, $E^2$.  Two nuclear processes are particularly important in determining the yield of particles following proton-nucleus interactions: nuclear evaporation and intranuclear cascade. The evaporation neutrons are emitted isotropically and energy extend to about 8 MeV.  The neutrons generated from intranuclear cascade process have higher energies and can extend up to the energy of the incident proton beam. Its angular distribution is no longer uniform but forward peaked with respect to the incident proton beam direction. [32]  These produced neutrons present a concern by increasing the stray radiation dose exposed to the normal tissues in patients due to their abundance, which could potentially diminish the advantages of therapeutic protons.

Neutron production in proton accelerators with passive scattering systems has been studied using both measurements and Monte Carlo methods. [89-94]  It is found that the neutron fluence and neutron dose equivalent varies with proton beam energy, field size, nozzle components design, and other factors, such as neutron dose determine methods and experimental conditions. The magnitude of reported neutron doses is thus significantly inconsistent, with reports demonstrating as much as 3 orders of magnitude difference between measured and calculated values.

Binns *et al* (1997, [90]) measured neutron dose equivalent per therapeutic proton absorbed dose (H/D) values, between 33 and 88 mSv/Gy, in the 200 MeV beam-line of the National Accelerator Centre (NAC), at lateral distances ranging from 30 to 120 cm from the beam axis.

Yan *et al* (2002, [91]) used a Bonner sphere measured the H/D values from the 160 MeV proton beam at the Harvard Cyclotron Laboratory (HCL). They reported for a large field treatment, the H/D values ranged from approximately 1 to 15 mSv/Gy around the nozzle at distances from 26 to 196 cm from the isocenter and angles from 0° to 135° with respect to the beam-line axis. The highest H/D values were at locations close to the nozzle. Polf *et al* (2005, [92]) later used Monte Carlo methods to study the neutron spectral fluence for a same large field treatment beam-line at the HCL. They reported H/D values of up to 10 mSv/Gy around the treatment nozzle for a beam with an 8.5 cm SOBP. They also reported that H/D values increased with increasing range modulation.

Wroe *et al* (2007, [93]) measured neutron dose equivalent for a 225 MeV passively scattered proton beam at Loma Linda University Medical Center (LLUMC) and reported H/D values decreased with increasing lateral distance from the proton field edge. The H/D value for a typical prostate cancer field was ranging from 0.3 to 8.3 mSv/Gy for lateral distances from 60 to 25 cm. Moyers *et al* (2008, [94]) used both MCNPX and measurement techniques to assess neutron dose equivalent around the gantry #2 at the Loma Linda University Proton Treatment Facility (LLUPTF). They reported that, for a 250 MeV proton beam (range of 28.9cm), the measured H/D values using SWENDI-2 were ranging from 0.0922 to 1.11 mSv/Gy for off-axis distance of 29 to 100cm from the isocenter. They also reported the difference between simulated values and the measured values by as much as a factor of 4.

### 4.1.3    The MEVION S250 Proton Accelerator

The MEVION S250 proton accelerator (MEVION Medical Systems, formally Still River System, MA) utilizes a superconducting magnet synchrocyclotron with passive double scattering method for beam delivery.  It is a low power (120kW) and light weight (18 Tons) system that allows for a gantry mounted cyclotron.

The proton beam extraction efficiency of MEVION S250 is claimed to be 90% according to the manufacturer.  In other words, approximately 10% of protons are lost in the cyclotron before extraction.  The protons exit the cyclotron and enter the beam shaping system through a vacuum window approximately two meters away from the isocenter.  Figure 4.3 shows the components of the MEVION S250 treatment nozzle.  The beam shaping system comprises a first scatterer, 14 different rotating range modulator wheels, a range shifter (downstream absorber), 3 different second scatterers and a final absorber (post absorber).  With different combination of these components which are made with lead and carbon, 24 unique configurations with different penetration depths and beam modulations (SOBP) are available from the MEVION S250.  Two different circular field sizes can be generated: 25 cm and 14 cm in diameter at the isocenter.  The spread proton beam then passes through the theta carriage and the shielding box which can be extended or retracted so that the treatment applicator can be as closed as needed to patients during treatments.  The patient-specific brass aperture housed at the end of the applicator is used to fine tune the beam shape to the target volume in patients.  A range compensator may also be added to customize the range across the area of the field.
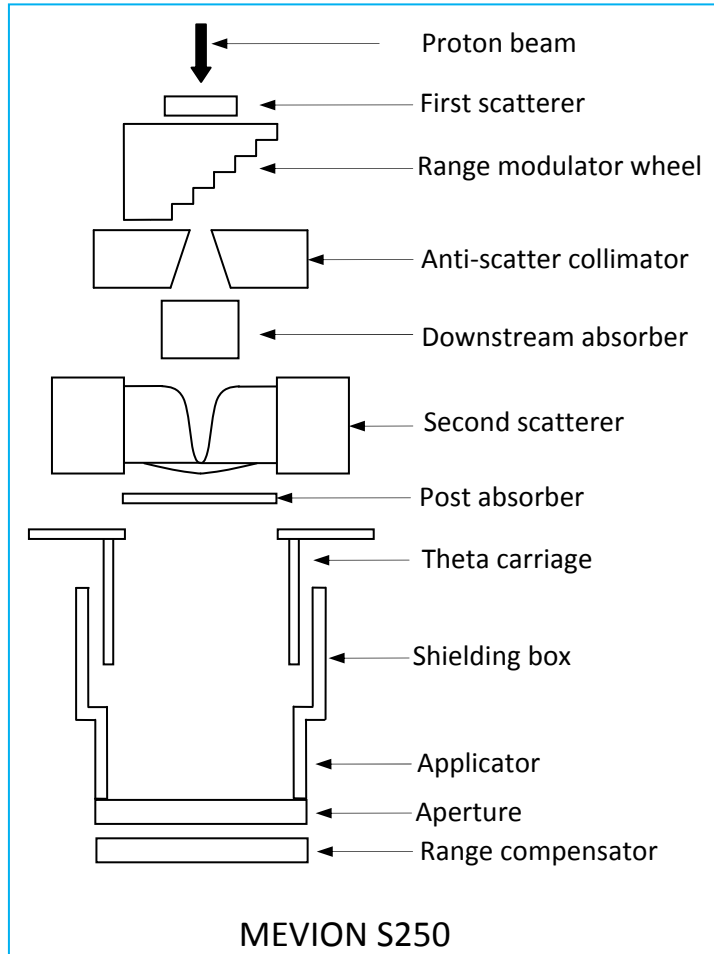
**Figure 4.3**    A schematic of the MEVION S250 proton accelerator nozzle. With different combination of these components, 24 unique configurations with different penetration depths and beam modulations are available.

## 4.2    Methods and Materials

To quantify the neutron production from the MEVION S250, the neutron dose equivalent was experimentally determined at various locations for three treatment configurations in the testing vault at MEVION Medical Systems in Littleton, MA, and compared with Monte Carlo calculations.   Additional simulations were performed to provide more information on neutron dose equivalent at different locations.

In this work, four treatment beam-line configurations were studied as shown in Table 4.1.  Configuration A was a 14 cm diameter field, 32 cm penetration depth and a 10 cm spread out Bragg peak (SOBP).  Configuration B was same as configuration A, but with small applicator. Configuration C was for a large field with a diameter of 25 cm, a range of 25 cm, and a 20 cm SOBP.   Configuration  D  was  also  a  large  field  (a  25  cm  in  diameter)  but  with  a  shallow penetration depth (5.6 cm) and a 5.6 cm SOBP.  A schematic drawing of each configuration is shown in Figure 4.4.

**Table 4.1**    The treatment configurations of the MEVION S250 included in this study.

| Configuration (#)[a] | SOBP (cm) | Range (cm) | Field Size (cm) | Applicator | Measurements | MC |
|---|---|---|---|---|---|---|
| A (13) | 10 | 32 | 14 | Large | √ | √ |
| B (13) | 10 | 32 | 14 | Small | √ | √ |
| C (1) | 20 | 25 | 25 | Large | √ | √ |
| D (12) | 5.6 | 5.6 | 25 | Large | NA | √ |

a. The # was specified by the manufacturer.
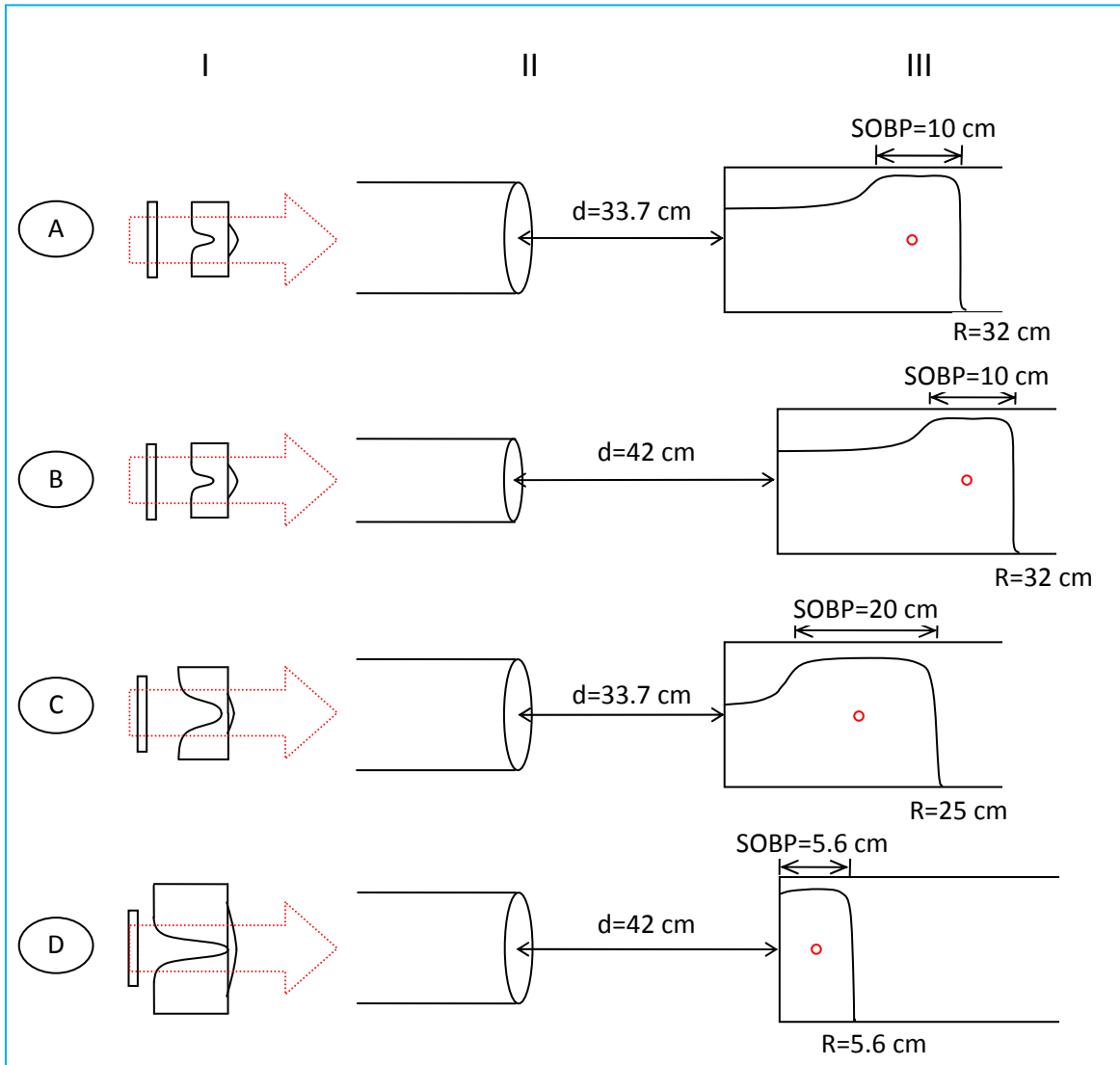
**Figure 4.4**    A schematic drawing of the four configurations of the MEVION S250 that are studied.  "I" represents the beam line;  "II" the field size and distance from beam line to surface; and "III" the result and percent depth dose curve.

## 4.2.1    Measurements

Neutron dose equivalents (H) were measured for configuration A – C.  The dose and dose equivalent for all measurements were normalized to the physical dose delivered at the isocenter.  The extension box connected to the applicator was retracted so that the downstream face of the applicator was 33.7 cm away from isocenter for configuration A and C, and 42 cm for configuration B.  Three positions were investigated as shown in Figure 4.5a.  Position 1 was located on the patient plane at approximately one meter away from the central axis.  Position 2 was under the edge of theta carriage, perpendicular to the beam central axis at 1.25 m towards to the floor.  Position 3 was chosen to help evaluate shielding, and was located at approximately one meter away the back of the accelerator along the central axis plane.  Two sets of data were collected; one set with 2.5 inch thick solid brass aperture where no beam transmission to the water phantom (closed field) and one set of data with no aperture (open field).
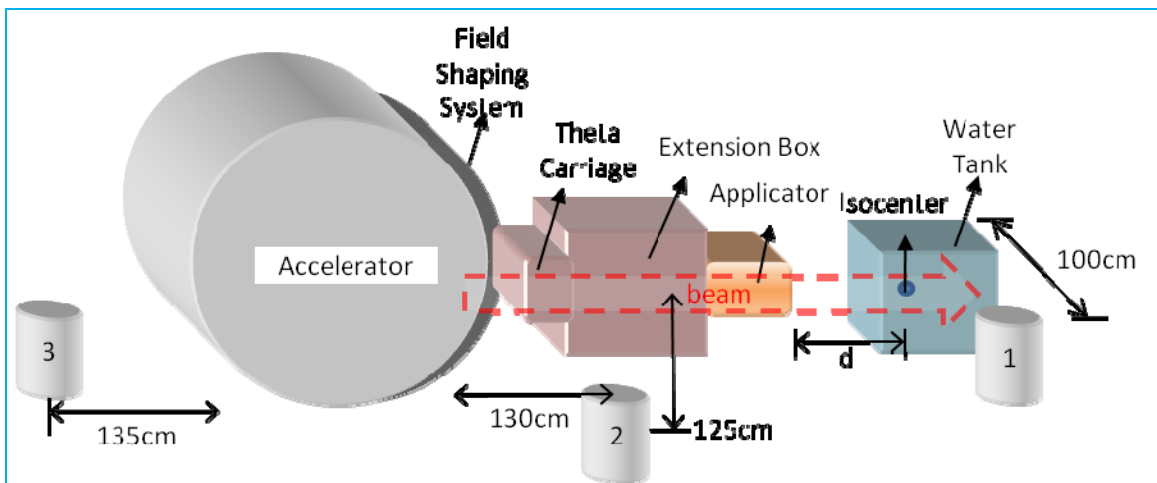


 **Figure 4.5a**  Schematic 3D view of the measurement setup, where d is the distance from the downstream face of the applicator to the isocenter. Position 1 locates at one meter laterally way from the incident proton beam.    Position 2 locates under the theta carriage and is 1.25 m below the central beam axis. Position 3 locates ~1.35 m upstream the accelerator.
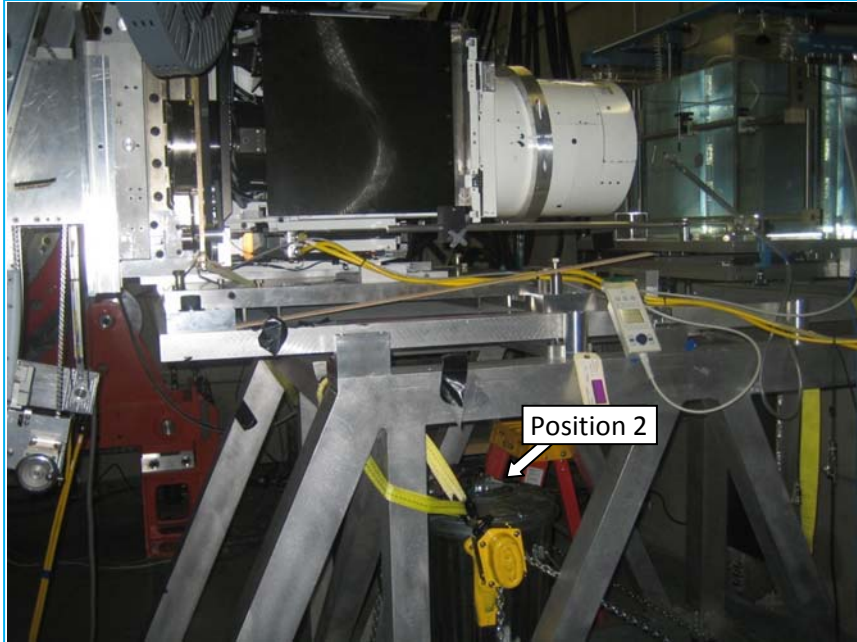
**Figure 4.5b** Experiment setup for position 2. The neutron detector is placed inside a thin steel container and located under the theta carriage.

## 4.2.1.1    Determination of Neutron Dose Equivalent (H)

For all measurements, a 250 MeV proton beam was delivered for 60 seconds.  The beam current was limited to 10 nA, frequency of 500 Hz and pulse width of 1 μs.  The ion source, $H_2$ gas, was set with a flow rate of 0.25 sccm. This low flow rate setting reduced the ion source output to avoid a "pile up" effect with the neutron detector that would result in counting loss. Two types of neutron detection systems were used for measurements; 1) SWENDI detector (Thermo Scientific, MA) and 2) BD-PND™ bubble dosimeter (Bubble Technology Industries, Canada).

The SWENDI detector is the second version of a **W**ide **E**nergy **N**eutron **D**etection **I**nstrument made of high-density polyethylene. [95]  A $^3$He tube is placed in the center of the polyethylene moderator and is surrounded by a layer of tungsten powder to increase the

sensitivity to neutron energy to approximately 10 MeV.  The SWENDI detector was placed in a thin steel container to avoid electromagnetic interference (Figure 4.5b).  A video camera was attached inside to capture the output display so that the integral dose equivalent could be read directly at the end of each run without entering the room as not to disrupt the setup.

The BD-PND[TM] bubble detectors are passive neutron dosimeters.  Superheated liquid drops are suspended in a polymer matrix inside a thin glass tubing which has dimension of 1.9 cm in diameter and 14.5 cm in length.  Visible vapor bubbles are formed when ionizing radiation pass through the polymer and release energy that induces localized boiling of the superheated liquid drops. [96]  The energy range for the BD-PND[TM] bubble detector is from <200keV to >15MeV.  This maximum energy response for this experiment may be limiting as neutron energies can be as high as 250 MeV.  Bubble detectors can be reset by a piston and reused.  The vendor stated sensitivity for the two BD-PND[TM] bubble detectors used are 14 bubbles/mrem and 45 bubbles/mrem respectively at an operating temperature range of 20-37 ˚C.  The number of bubbles for each measurement is counted by two individuals and the average number was recorded. The dose equivalent (H) was then calculated by equation (4.1).

$$H(mrem) = \frac{\# \text{ of bubbles}}{14 \text{ or } 45 \text{ bubbles/mrem}} \quad ......(4.1)$$

## 4.2.1.2    Determination of Physical Delivered Dose (D)

A Wellhofer cylindrical ionization chamber (Wellhofer FC65-P/BNC-SN1911; IBA Dosimetry, TN) was placed in a water tank (Blue Phantom, IBA Dosimetry America, TN) to determine the absolute dose delivered.  A Dose-1 electrometer (IBA Dosimetry America) connected to the chamber was calibrated to indicate the measured dose delivered (D).

A Parallel Plate Chamber (PPC05; IBA, TN) was placed in the water tank to determine the absolute dose delivered.  The vendor stated sensitivity of the PPC05 is $5.1839 \times 10^8$ Gy/C.  The Dose-1 electrometer (IBA dosimetry America, TN) with a measuring mode set to be as 21.7 nC/Gy was used, and displayed "measured" dose (M, Gy).  The delivered dose (D, Gy) was then calculated using equation (4.2).

$$D \text{ (Gy)} = M \text{ (Gy)} * 21.7 \text{ nC/Gy} * 5.1839*10^{-1} \text{ Gy/nC} \quad ......(4.2)$$

## 4.2.1.3    Determination of Measured H/D

The obtained Neutron Dose Equivalent (H) and Physical Delivered Dose (D) were used to calculate H/D directly for open fields.  In the case when full slab brass apertures were used, the protons were absorbed by the brass, and the recorded dose was nearly zero.  Thus, the average neutron dose equivalent per therapeutic dose (mSv/Gy) was normalized using recorded monitor unit (MU) values according to following (equation (4.3)).

$$(\text{mSv/Gy}) = \frac{\text{Recorded neutron equivalent}}{\text{MU} * c} ......(4.3)$$

Where $c$ is the dose/MU measured in the case of open field.

## 4.2.2    Monte Carlo Simulations

Neutron dose equivalents per absorbed dose (H/D) were calculated for configurations A – D.  A detailed model of the MEVION S250 nozzle was created which accurately represented the actual beam-line components.  The cyclotron and the testing vault conditions, including walls, ceiling, and floor, were also accounted for.  The incident proton beam impinged onto the upstream surface of the first scatter was simulated with a mean energy of 250 MeV, which had

an initial Gaussian distribution profile in energy ($\sigma_E$ = 0.42 MeV) and in space ($\sigma_x = \sigma_y$ = 0.25 cm).

Each neutron source was simulated with $1 \times 10^8$ proton histories, unless specified otherwise, to ensure the statistical relative error was less than 0.05%. For all calculations, simulation mode was set to include neutrons, protons and photons, so that all these particles were transported and tracked. Parallel computations were run, using up to 7 desktop computers and 54 nodes.

To benchmark the simulation methods, H/D values were calculated corresponding to all measured positions with the water phantom in place. To estimate H/D values as a function of location around the treatment nozzle, additional positions were calculated for each configuration. As shown in Figure 4.6, H/D were calculated on the patient plane at distances of r = 50, 75, 100, 125 and 150 cm from isocenter and at angle of $\theta$ = 0°, 45°, 60°, 90° and 135° with respect to the initial beam central axis. Limited by physical walls locations of the testing vault and the large water phantom (Blue Phantom, IBA Dosimetry America, TN) used in this work, H/D values were determined up to 25 locations for each configuration.

Calculations were also performed to examine the dose contribution from the water phantom. The water phantom importance was set to be zero in these simulations, so that all particles entering water phantom were assumed absorbed.
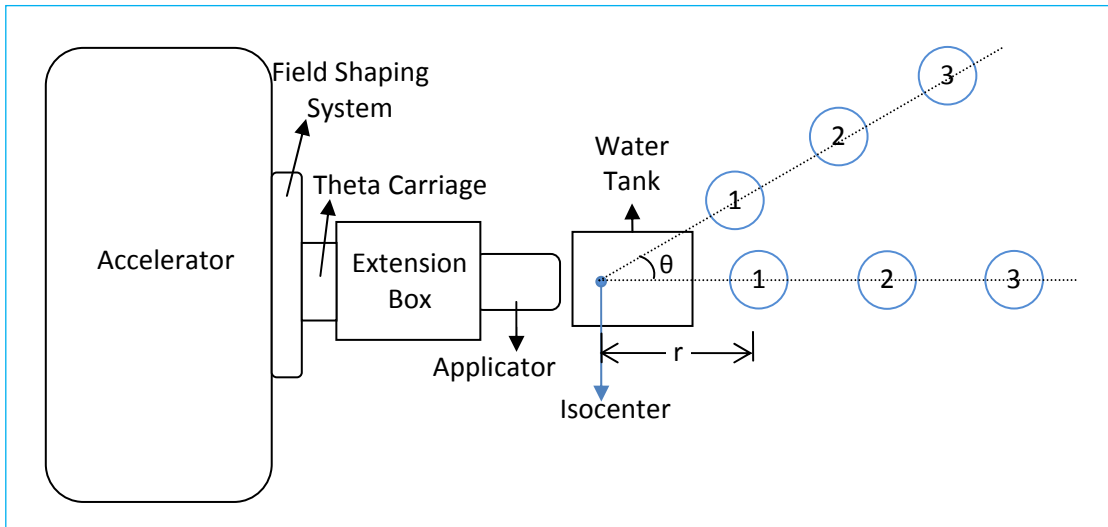
**Figure 4.6** Schematic view of the simulation setup. The blue circles represent neutron receptors; where r is the distance from neutron meter to isocenter, and θ is angle with respect to the beam central axis. (Note: figure no to scale)

In light of the fact that most neutrons were produced within the beam-line components, H/D values were calculated with 1 inch thick of shielding placed around the nozzle for configuration C, open field, to assess the effect of this additional shielding.  Two materials were investigated, 5% borated polyethylene (BPE, 11.6% H, 5% B, 61.2% C, 22.2% O, model SWX-201HD, Shieldwerx[TM], NM) and nickel.   Two different shielding lengths were considered as shown in Figure 4.7; a shorter shielding box (80 × 80 × 88 cm$^3$, Figure 4.7a) only covered the theta carriage and the applicator; where as in Figure 4.7b, an additional shielding box (60 × 60 × 88  cm$^3$) was added to extended the coverage from the applicator to target.
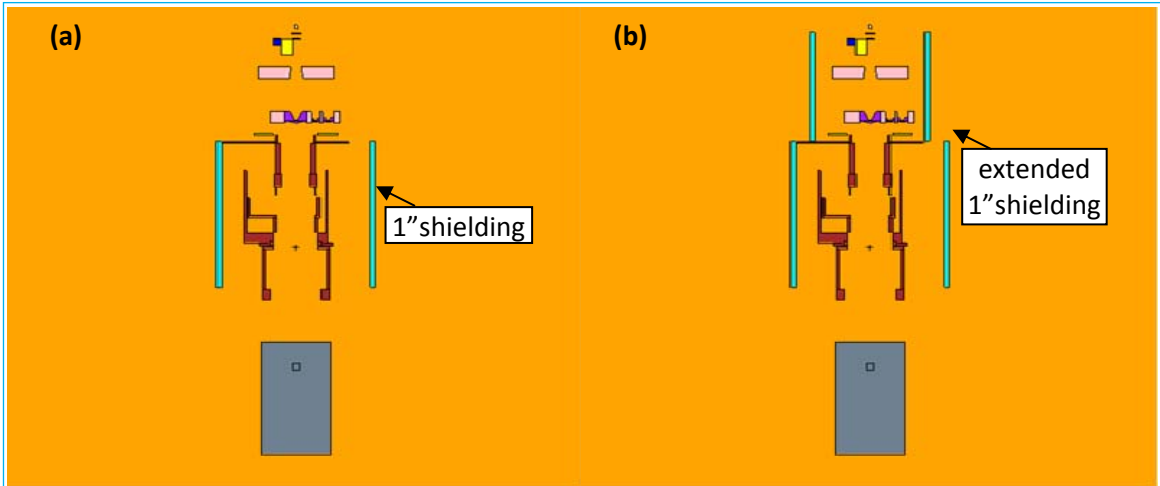
**Figure 4.7** Additional 1 inch shielding boxes made of either 5% BPE or Ni are added around the treatment nozzle for configuration C open field to estimate the H/D values. In (a), a shielding box only covers the theta carriage and the applicator. In (b), shielding box extended to cover the target. (Note: figure not to scale).

## 4.2.2.1    Calculations of Neutron Dose Equivalent and Proton Absorbed Dose

To determine the neutron dose equivalent per absorbed dose (H/D) around the treatment nozzle, total neutron dose equivalent per incident proton (H/p) and total therapeutic proton dose per incident proton (D/p) were obtained separately (equation (4.4)).

$$\frac{H}{D} = \frac{H/p}{D/p} \quad \cdots\cdots (4.4)$$

The value H/p, is calculated based on the simulated neutron spectral fluence, $\Phi(E_n)$. Neutron spectral fluences per incident proton ($\Phi(E_n)/p$, cm$^{-2}$) were tallied in 400 logarithmically spaced energy bins between 0.01 eV and 300 MeV within 12-cm-diameter, air filled spherical receptors. These energy weighted neutron spectral fluence were then converted to energy weighted neutron dose equivalent ($H(E_n)/p$) using the energy dependent fluence-to-dose

equivalent conversion coefficient ($h_{\Phi_E}$, Sv cm$^2$) from the ICRP Publication 74 (1996, [29]) according equation (4.5).

$$H(E_n)_i/p = h_{\Phi}(E_n)_i \cdot \Phi(E_n)_i \cdot d(E_n)_i \quad \cdots\cdots (4.5)$$

Where $(E_n)_i$ is maximum neutron energy of the ith energy bin and $d(E_n)_i$ is the ith neutron energy interval. The total neutron dose equivalent per incident proton (H/p) at each location was then obtained by summing the neutron spectral fluence over all energy bins according equation (4.6).

$$H/p = \sum_{i=1}^{m} H(E_n)_i/p \quad \cdots\cdots (4.6)$$

Where m is the total number of energy bins.

The value of D/p was determined on the central axis at the depth corresponding to the center of the spread out Bragg peak (SOBP) of each configuration. The water phantom, measuring 68 cm in depth (along the beam plane), 40.7 cm in height, and 35 cm in width, was positioned with its upstream face normal to the incident beam and the isocenter was located at the center of the SOBP. The absorbed dose was tallied within a 2 × 2 × 2 cm$^2$ space at isocenter, i.e. the center of the SOBP. The F6 tally was used to tally the energy deposit over the simulation space. The total absorbed doses tallied were including doses from all types of particles tracked.

In reality, the range modulator wheel (RMW) was continuously rotating at a certain rate during treatment. Due to the limitation of computing time, however, all calculations reported in this chapter, unless specified otherwise, were simulated with the RMW set to be at the middle of the thinnest step (one step only). One additional calculation was done for configuration C to obtain the weighted H/D values ($(H/D)_{weighted}$) where all steps were used according to equation (4.7).

$$(H/D)_{weighted} = \sum_{j=1}^{k} (H/D)_j \cdot w_j \quad \cdots\cdots (4.7)$$

The value k, is the total steps of a RMW including one brass stop block; $(H/D)_j$ is the jth neutron

equivalent dose per absorbed dose calculated at the middle of each step and $w_j$ is the weighting

of the jth step based on each step angle. In the case of configuration C, the RMW is composed of

19 steps and 1 brass stop block.  For each step, $1 \times 10^7$ proton histories were calculated in this

calculation.

## 4.3     Results and Discussion

### 4.3.1      Comparison of Measurements and Calculations

To validate the simulation method built for determining total neutron dose equivalent

per therapeutic proton dose (H/D) in this work, the H/D values of the three examined positions

obtained by measurements and calculations were compared and listed in Table 4.2.   The

measured H/D values for configuration A using SWENDI and BD-PND[TM] bubble detectors were

less than 20% different.  The calculation values agreed with the measured values within a factor

of 2.

The higher H/D values in closed fields were the results of protons stopping in high Z

materials (brass apertures).  For ease of comparison, simulated H/D values for position 1 – 3 for

configuration D were also included in Table 4.2.   For configuration D, H/D values were not

notably different between open field and closed field.   This was because for such a shallow

depth (5.6 cm range) and a small SOBP (5.6 cm), most of the incident protons were degraded in

the beam-line before reaching the brass apertures, that the neutron production in the closed

fields did not increase significantly as the result of existence of these high Z materials.  Such greater degradation in the beam-line also led to higher H/D values at all positions for configuration D, compared to the other three configurations.

Configuration C and D were the large lateral field size configurations which allowed for treating tumors with large sizes. H/D values were higher in C and D compared to A and B. The reason was the amount of lead and carbon used for the first and second scatterers were greater for configuration C and D, which resulted in shorter ranges and larger field sizes.

Simulated H/D values were found to be between 0.36 and 2.94 mSv/Gy at Position 1. Position 2 had relatively higher H/D values for all configurations. This may be due to the fact that position 2 was closer to the floor and neutron scattering was more significant.  The highest H/D value was found to be at position 2 for configuration D.  Position 3 representing radiation leakage, the simulated H/D values were less than 0.5 mSv/Gy for all configurations considered (ranging from 0.034 to 0.394 mSv/Gy).

**Table 4.2**     Comparison of the measured and simulated total neutron dose equivalent per therapeutic dose (H/D) in unit of mSv Gy$^{-1}$ for configuration A – C. All measured H/D are normalized to the physical dose delivered at the isocenter.  Simulated H/D values for configuration D are included.

| Position | open field | | | | closed field | | | |
|---|---|---|---|---|---|---|---|---|
| | SWENDI (mSv/Gy) | BD-PND (mSv/Gy) | MCNPX (mSv/Gy) | $\frac{\text{MCNPX}}{\text{SWENDI}}$ | SWENDI (mSv/Gy) | BD-PND (mSv/Gy) | MCNPX (mSv/Gy) | $\frac{\text{MCNPX}}{\text{SWENDI}}$ |
| **configuration A** | | | | | | | | |
| 1 | 0.39 | NA | 0.36 | 0.92 | 0.51 | NA | 0.90 | 1.76 |
| 2 | 0.36 | 0.31 | 0.45 | 1.25 | 0.55 | 0.66 | 0.83 | 1.51 |
| 3 | 0.14 | 0.10 | 0.034 | 0.24 | NA | NA | 0.062 | NA |
| **configuration B** | | | | | | | | |
| 1 | 0.50 | NA | 0.44 | 0.88 | 0.81 | NA | 0.94 | 1.16 |
| 2 | 0.84 | NA | 0.51 | 0.61 | 0.94 | NA | 0.89 | 0.95 |
| 3 | 0.17 | NA | 0.044 | 0.26 | 0.19 | NA | 0.061 | 0.32 |
| **configuration C** | | | | | | | | |
| 1 | 1.93 | NA | 1.70 | 0.88 | 2.16 | NA | 2.71 | 1.25 |
| 2 | 2.18 | NA | 2.78 | 1.28 | NA | NA | 3.56 | NA |
| 3 | 0.56 | NA | 0.19 | 0.34 | NA | NA | 0.25 | NA |
| **configuration D** | | | | | | | | |
| 1 | | | 2.84 | | | | 2.92 | |
| 2 | | | 5.72 | | | | 5.78 | |
| 3 | | | 0.389 | | | | 0.394 | |

Monte Carlo simulations confirmed that the generated neutrons from the MEVION S250 had energies ranging from thermal to the full primary incident proton energy of 250 MeV.  The calculations also revealed that the largest contribution to neutron dose equivalent were from high energy neutrons (Figure 4.8).  Figure 4.8a showed the neutron fluence spectra per incident proton ($\Phi(E_n)/p$) for position 1 for configuration A – D.   Each neutron fluence spectrum contained three peaks; including a thermal neutron peak, an evaporation neutron peak around 1 MeV, and finally a cascade neutrons peak.  The energy between 1 eV to 0.01 MeV was the $1/E_n$ region, where neutron fluence was approximately proportional to the inverse of the neutron energy.  The neutron fluence spectra also indicated more neutrons were produced in closed fields than for open fields, especially for configurations with large SOBPs and deep penetration depths, i.e. configuration A – C.  The corresponding spectra of neutron dose equivalent per incident proton ($H(E_n)/p$) are plotted in Figure 4.8b.  These $H(E_n)/p$ spectra show that neutrons

with energy less than 0.01 MeV (thermal neutrons and $1/E_n$ regions) do not contribute significantly to the total neutron dose equivalent (H). To better understand the H/D distribution as a function of neutron energy, $H(E_n)/p$ was normalized to total absorbed proton dose at the isocenter and plotted as $H(E_n)/D$ spectra in Figure 4.8c. The $H(E_n)/D$ spectra allow for direct comparison between each configuration. As indicated in 4.7c, evaporation neutrons are the dominant sources to the total neutron dose equivalent for all configurations in this position. For configuration D, in addition to the evaporation neutrons, cascade neutrons are also prominent sources that contributed to the total neutron dose equivalent.

Neutron production distributions in terms of fluence, dose equivalent for position 2 and 3 are plotted in Figure 4.9 and Figure 4.10 respectively. Similar to position 1, $H(E_n)/D$ spectra revealed that evaporation neutrons and cascade neutrons are dominant for point 2 (Figure 4.9c). For the radiation leakage location (position 3), neutron production is much lower. The majority of neutrons have energies at the thermal range and around 1 MeV range (Figure 4.10a). Most of the neutron dose equivalent for position 3 comes from evaporation neutrons (Figure 4.10c).

**a.** Neutron fluence spectra per incident proton ($\Phi(E_n)/p$).

**b.** Neutron dose equivalent per incident proton ($H(E_n)/p$).

**c.** Neutron dose equivalent per absorbed dose ($H(E_n)/D$).
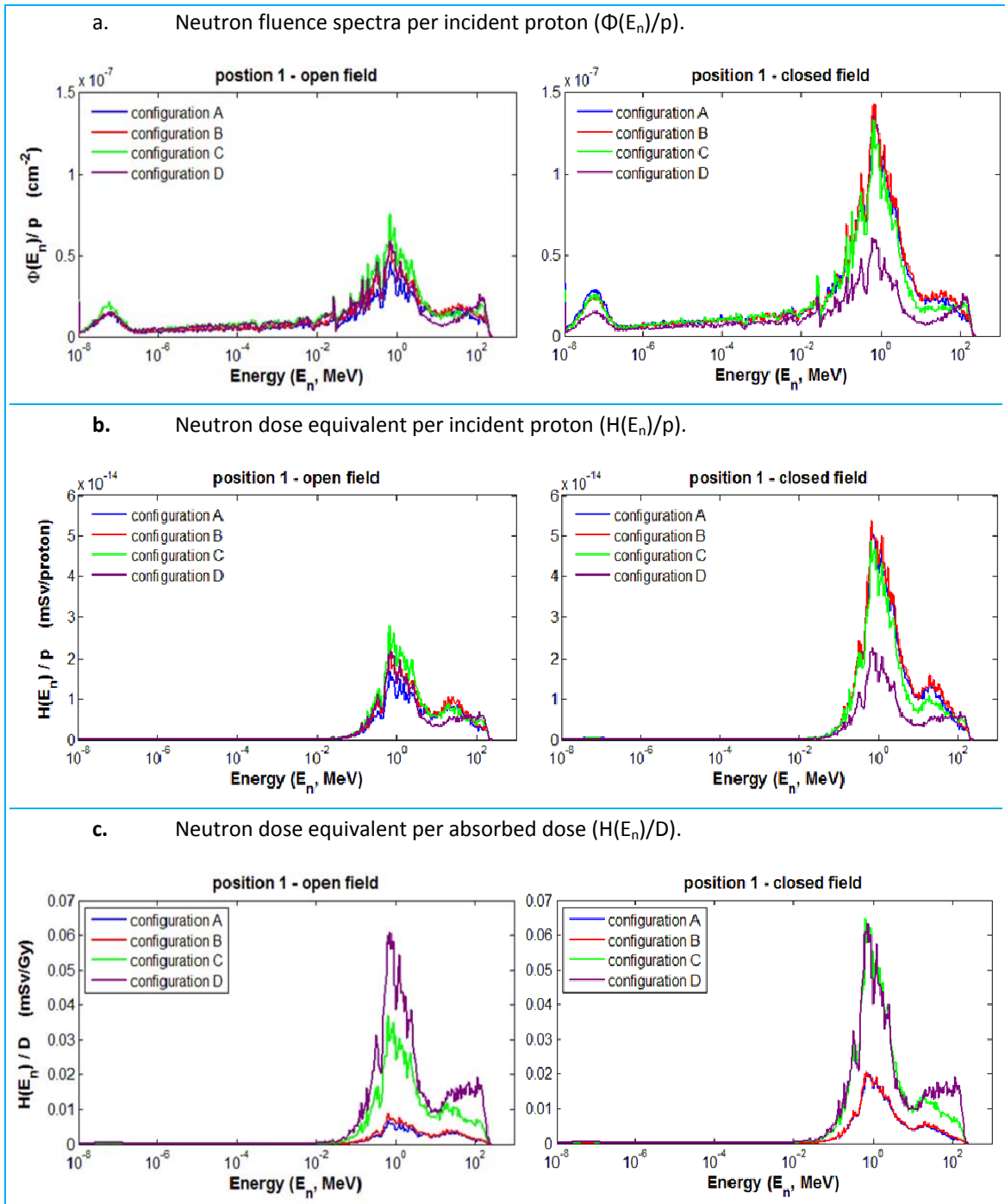
**Figure 4.8** Neutron productions at position 1 for configuration A – D in terms of fluence and dose equivalent are presented. 4.8a are the spectra of neutron fluence per incident proton, $\Phi(E_n)/p$; three peaks were due to thermal neutrons, evaporate neutrons and cascade neutrons. Neutron productions are greater in closed fields. 4.8b are the spectra of neutron dose equivalent per incident proton ($H(E_n)/p$). Neutrons with energies less than 0.01 MeV do not contribute significantly to total dose equivalent. 4.8c are the neutron dose equivalent spectra normalized to the total absorbed dose.

**a.** Neutron fluence spectra per incident proton ($\Phi(E_n)/p$).

**b.** Neutron dose equivalent spectra per incident proton ($H(E_n)/p$).

**c.** Neutron dose equivalent per absorbed dose ($H(E_n)/D$).
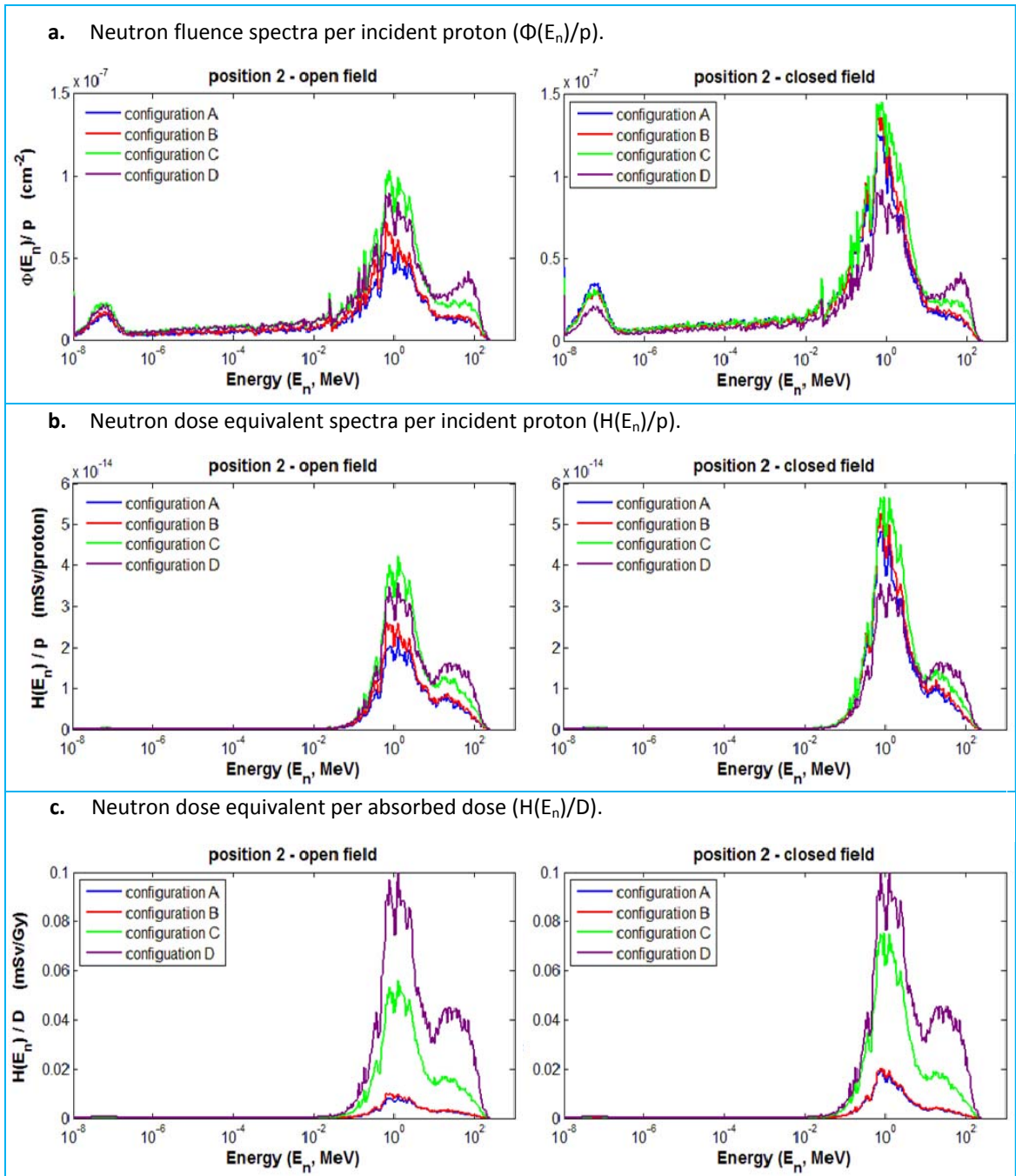
**Figure 4.9** Neutron productions at position 2 for configuration A – D in terms of fluence and dose equivalent are presented. 4.9a are the spectra of neutron fluence per incident proton, $\Phi(E_n)/p$; three peaks were due to thermal neutrons, evaporate neutrons and cascade neutrons. More neutrons are produced in closed fields. 4.9b are the spectra of neutron dose equivalent per incident proton ($H(E_n)/p$). Neutrons with energies less than 0.01 MeV do not contribute significantly to total dose equivalent. 4.9c are the neutron dose equivalent spectra normalized to the total absorbed dose.

**a.** Neutron fluence spectra per incident proton ($\Phi(E_n)/p$).



**b.** Neutron dose equivalent spectra per incident proton ($H(E_n)/p$).



**c.** Neutron dose equivalent spectra per absorebed dose ($H(E_n)/D$).
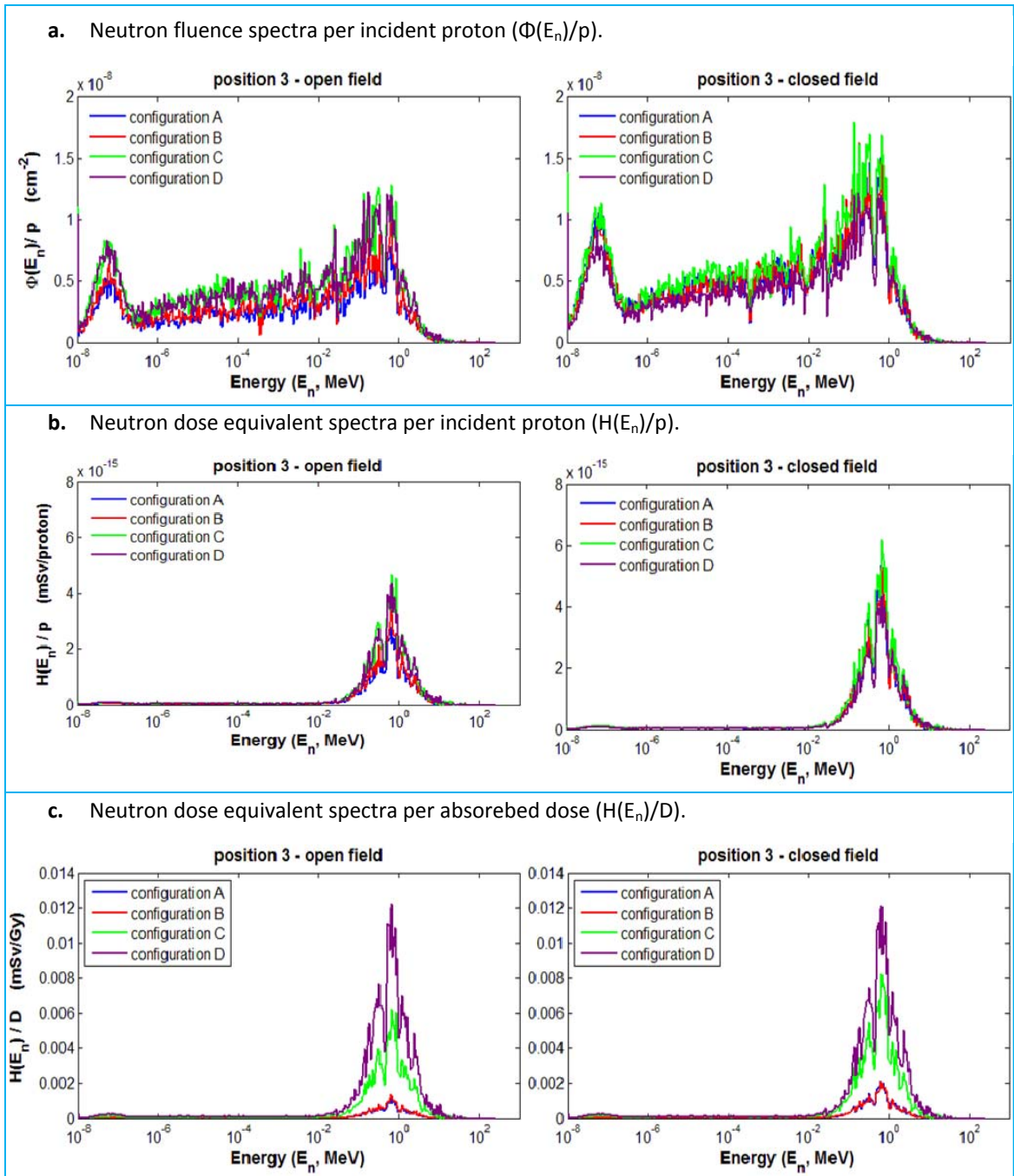


**Figure 4.10** Neutron productions at position 3 for configuration A – D in terms of fluence and dose equivalent are presented. 4.10a are the spectra of neutron fluence per incident proton, $\Phi(E_n)/p$; three peaks were due to thermal neutrons, evaporate neutrons and cascade neutrons. More neutrons are produced in closed fields. 4.10b are the spectra of neutron dose equivalent per incident proton ($H(E_n)/p$). Neutrons with energies less than 0.01 MeV do not contribute significantly to total dose equivalent. 4.10c are the neutron dose equivalent spectra normalized to the total absorbed dose.

## 4.3.2    Influence of the Water Phantom on H/D Values

Since water is an excellent moderator for fast neutrons and a relatively good absorber for thermal neutrons, the attenuation and scattering of protons in the water phantom (patient) may affect total H/D values.  To study the neutron dose equivalent contribution from the large water phantom used in all simulations, open fields calculations were performed for all four configurations with particle tracking turned off, and the results are listed as "exclude water phantom" in Table 4.3.  By comparing to the H/D values in Table 4.2 (listed as "include water phantom in Table 4.3), the percent differences indicates the net amount of neutron dose equivalent came from or absorbed by the water phantom.  The value percent difference is defined as

$$\% \text{ difference} = 100 \left( \frac{\text{Including water phantom-excluding water phantom}}{\text{including water phantom}} \right)$$

**Table 4.3**    Calculated H/D (mSv/Gy) for open field for configuration A – D. The values of excluding water phantom are obtained by assuming all particles are absorbed in the water phantom. The percent differences indicate the contributions from the water phantom.

|  | position | Include water phantom | Exclude water phantom | % from water |
|---|---|---|---|---|
| | | **H/D (mSv/Gy)** | | |
| configuration A | 1 | 0.36 | 0.19 | 46% |
| | 2 | 0.45 | 0.37 | 17% |
| | 3 | 0.034 | 0.026 | 24% |
| configuration B | 1 | 0.44 | 0.30 | 30% |
| | 2 | 0.51 | 0.45 | 13% |
| | 3 | 0.044 | 0.031 | 18% |
| configuration C | 1 | 1.70 | 1.38 | 19% |
| | 2 | 2.78 | 2.63 | 5% |
| | 3 | 0.19 | 0.17 | 8% |
| configuration D | 1 | 2.84 | 3.05 | -7.61% |
| | 2 | 5.72 | 5.64 | 1.50% |
| | 3 | 0.389 | 0.38 | 1.71% |
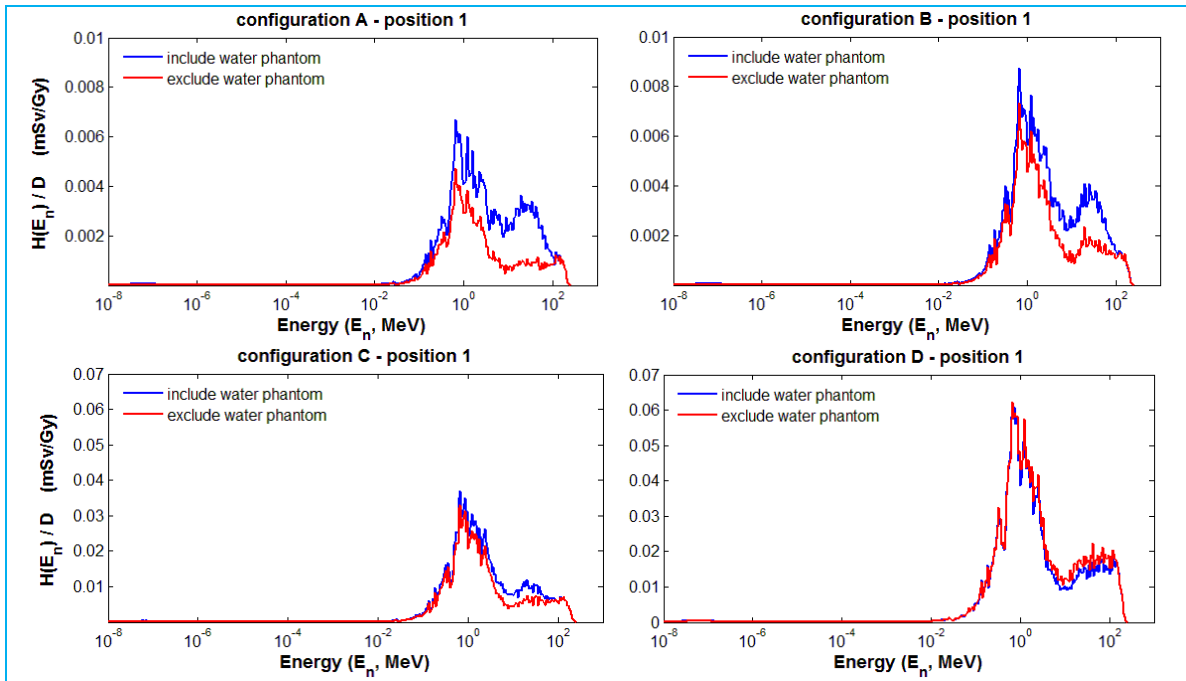
**Figure 4.11** Simulated $H(E_n)/D$ spectra of position 1 for configuration A – D open fields to show the influence of water phantom. For configuration A – C, the effects of net neutron productions are greater than absorptions in this location; whereas for configuration D, net neutron absorption is slightly significant.

The lower H/D values for excluding water phantom simulations are the result of assuming no particles came from the water phantom. In other words, exclusion of the water phantom is a pure absorption effect for neutrons. The significance of water moderating neutrons that originated in the nozzle depended on the neutron receptors' locations. Position 3 was the most distant from the water phantom, thus was the least impacted. The most impacted location was position 1 of the three positions considered. This was most likely due to position 1 located closest to the water phantom, as there was only air between the neutron receptor and the water phantom.

In reality, the water phantom not only served as a moderator for neutrons produced in the nozzle, but also as a neutron source and a moderator for neutrons reaching the water phantom. This is important to understand as patients are also a source of neutrons. As shown in Figure 4.11, the net result from existence of water phantom increased neutron dose equivalent at both evaporation and cascade neutrons in configuration A – C position 1.

The negative value at position 1 for configuration D suggested that neutron absorption in the water phantom was greater than production to this location, as shown in Figure 4.11 – configuration D. This was a combined effect from the unique characteristics of configuration D and the location of position 1. Since configuration D was a short range configuration, a large fraction of neutron dose equivalent came from the high energy neutrons produced in the nozzle. In addition, because the isocenter was defined at the center of SOBP, i.e. 2.8 cm from the upstream face of the water phantom for configuration D, the amount of water allowed for attenuating those high energy cascade neutrons into evaporation neutrons was small. Furthermore, position 1 was located 90° laterally to the isocenter with respect to the incident proton beam axis. As would be discussed in more detail in next section, for positions located on the 90° to the incident proton beam plane, the cascade neutrons peaks are not a significant contributor to the total H/D. Therefore, when water phantom is considered, the net neutron does equivalent to position 1 is lower.

### 4.3.3 Neutron Dose Equivalent per Absorbed Dose (H/D) Distribution around the Treatment Nozzle

The H/D values around the treatment nozzle were calculated at various locations for configuration A – D. All locations were specified as a function of isocenter-to-neutron-receptor distnace (r) and as a function of angle (θ) with respect to the initial proton beam axis around the treatment nozzle as discribed in the method section. Three field sizes were considered for each configuration, including an open field, a 10×10 cm$^2$ field, and a closed field. The results are presented in Table 4.4 – 4.7 and Figure 4.12 – Figure 4.15 for configuration A – D respectively.

For configuration A, H/D values range from 0.31 to 1.12 mSv/Gy for open fields; 0.43 – 2.70 mSv/Gy for 10×10 cm$^2$ fields; and 0.38 – 3.85 mSv/Gy for closed fields. For configuration B, H/D values range from 0.35 to 1.15 mSv/Gy for open fields; 0.39 – 2.56 mSv/Gy for 10×10 cm$^2$ fields; and 0.34 – 4.46 mSv/Gy for closed fields. For configuration C, H/D values range from 1.32 to 3.15 mSv/Gy for open fields; 1.18 – 8.66 mSv/Gy for 10×10 cm$^2$ fields; and 1.10 – 9.30 mSv/Gy for closed fields. For configuration D, the H/D values range from 1.50 to 5.58 mSv/Gy for open fields; 1.41 – 5.61 mSv/Gy for 10×10 cm$^2$ fields; and 1.34 – 5.66 mSv/Gy for closed fields. With exceptions of all fields in configuration D and the open field in configuration A, the highest H/D value for each field size of each configuration is at the location of r = 50 cm and θ = 125°. For configuration D, the highest values are at the location of r = 150 cm and θ = 125° in open field, 10×10 cm$^2$ field and closed field.

**Table 4.4** Simulated H/D values as a function of distance from the isocenter (r) and angle with respect to the initial proton beam axis (θ) for configuration A; open field, 10×10 cm$^2$ field and closed field. 22 locations around the treatment nozzle are included.

| configuration A | | | | | |
|---|---|---|---|---|---|
| H/D (mSv/Gy) | | | | | |
| | angle (θ°) | | | | |
| Distance (r, cm) | 0 | 45 | 60 | 90 | 125 |
| **Open field** | | | | | |
| 50 | 1.09 | 1.12 | 1.10 | 0.95 | 0.78 |
| 75 | 0.61 | 0.67 | 0.65 | 0.58 | 0.63 |
| 100 | 0.48 | 0.49 | 0.47 | 0.45 | 0.55 |
| 125 | | 0.41 | 0.40 | 0.36 | 0.47 |
| 150 | | | 0.34 | 0.31 | 0.44 |
| **10×10 cm$^2$** | | | | | |
| 50 | 0.84 | 1.03 | 1.19 | 1.81 | 2.70 |
| 75 | 0.53 | 0.72 | 0.83 | 1.22 | 1.41 |
| 100 | 0.43 | 0.58 | 0.66 | 0.87 | 1.01 |
| 125 | | 0.51 | 0.55 | 0.63 | 0.77 |
| 150 | | | 0.48 | 0.50 | 0.67 |
| **Closed field** | | | | | |
| 50 | 0.60 | 0.93 | 1.21 | 2.40 | 3.85 |
| 75 | 0.45 | 0.74 | 0.94 | 1.65 | 1.91 |
| 100 | 0.38 | 0.62 | 0.77 | 1.11 | 1.33 |
| 125 | | 0.56 | 0.65 | 0.80 | 0.98 |
| 150 | | | 0.58 | 0.62 | 0.82 |

**Table 4.5** Simulated H/D values as a function of distance from the isocenter (r) and angle with respect to the initial proton beam axis (θ) for configuration B; open field, 10×10 cm$^2$ field and closed field. 22 locations around the treatment nozzle are included.

| configuration B | | | | | |
|---|---|---|---|---|---|
| H/D (mSv/Gy) | | | | | |
| | angle (θ°) | | | | |
| Distance (r, cm) | 0 | 45 | 60 | 90 | 125 |
| **Open field** | | | | | |
| 50 | 0.93 | 1.01 | 1.04 | 1.03 | 1.15 |
| 75 | 0.54 | 0.65 | 0.67 | 0.67 | 0.85 |
| 100 | 0.42 | 0.51 | 0.51 | 0.52 | 0.68 |
| 125 | | 0.43 | 0.43 | 0.42 | 0.55 |
| 150 | | | 0.37 | 0.35 | 0.51 |
| **10×10 cm$^2$** | | | | | |
| 50 | 0.78 | 0.95 | 1.10 | 1.66 | 2.56 |
| 75 | 0.49 | 0.69 | 0.83 | 1.09 | 1.43 |
| 100 | 0.39 | 0.58 | 0.66 | 0.78 | 1.01 |
| 125 | | 0.51 | 0.56 | 0.60 | 0.75 |
| 150 | | | 0.49 | 0.48 | 0.65 |
| **Closed field** | | | | | |
| 50 | 0.50 | 0.84 | 1.19 | 2.76 | 4.46 |
| 75 | 0.40 | 0.74 | 1.11 | 1.67 | 2.25 |
| 100 | 0.34 | 0.68 | 0.95 | 1.13 | 1.48 |
| 125 | | 0.63 | 0.81 | 0.84 | 1.06 |
| 150 | | | 0.70 | 0.67 | 0.87 |

**Table 4.6** Simulated H/D values as a function of distance from the isocenter (r) and angle with respect to the initial proton beam axis (θ) for configuration C; open field, 10×10 cm$^2$ field and closed field. 21 locations around the treatment nozzle are included.

| configuration C | | | | | |
|---|---|---|---|---|---|
| H/D (mSv/Gy) | | | | | |
| | angle (θ°) | | | | |
| Distance (r, cm) | 0 | 45 | 60 | 90 | 125 |
| **Open field** | | | | | |
| 50 | | 3.31 | 3.28 | 2.90 | 3.15 |
| 75 | 1.69 | 2.22 | 2.17 | 2.25 | 2.99 |
| 100 | 1.32 | 1.73 | 1.78 | 1.97 | 2.91 |
| 125 | | 1.55 | 1.54 | 1.69 | 2.63 |
| 150 | | | 1.41 | 1.47 | 2.72 |
| **10×10 cm$^2$** | | | | | |
| 50 | | 3.25 | 4.52 | 6.49 | 8.66 |
| 75 | 1.43 | 2.81 | 3.42 | 4.06 | 5.36 |
| 100 | 1.18 | 2.35 | 2.78 | 3.08 | 4.30 |
| 125 | | 2.14 | 2.36 | 2.44 | 3.56 |
| 150 | | | 2.10 | 2.04 | 3.40 |
| **Closed field** | | | | | |
| 50 | | 3.22 | 4.92 | 7.20 | 9.30 |
| 75 | 1.30 | 2.93 | 3.81 | 4.29 | 5.73 |
| 100 | 1.10 | 2.52 | 3.05 | 3.19 | 4.54 |
| 125 | | 2.29 | 2.55 | 2.52 | 3.72 |
| 150 | | | 2.26 | 2.11 | 3.52 |

**Table 4.7** Simulated H/D values as a function of distance from the isocenter (r) and angle with respect to the initial proton beam axis (θ) for configuration D; open field, 10×10 cm$^2$ field and closed field. 21 locations around the treatment nozzle are included.

| configuration D | | | | | |
|---|---|---|---|---|---|
| H/D (mSv/Gy) | | | | | |
| | angle (θ°) | | | | |
| Distance (r, cm) | 0 | 45 | 60 | 90 | 125 |
| **Open field** | | | | | |
| 50 | | 2.08 | 2.33 | 2.99 | 3.85 |
| 75 | 1.56 | 2.18 | 2.50 | 3.25 | 4.95 |
| 100 | 1.50 | 2.20 | 2.53 | 3.22 | 5.18 |
| 125 | | 2.21 | 2.37 | 2.95 | 4.95 |
| 150 | | | 2.34 | 2.69 | 5.58 |
| **10×10 cm$^2$** | | | | | |
| 50 | | 2.09 | 2.41 | 3.17 | 4.23 |
| 75 | 1.48 | 2.22 | 2.56 | 3.36 | 5.11 |
| 100 | 1.41 | 2.23 | 2.57 | 3.30 | 5.27 |
| 125 | | 2.23 | 2.41 | 3.00 | 5.00 |
| 150 | | | 2.37 | 2.73 | 5.61 |
| **Closed field** | | | | | |
| 50 | | 2.12 | 2.46 | 3.23 | 4.28 |
| 75 | 1.37 | 2.26 | 2.60 | 3.39 | 5.17 |
| 100 | 1.34 | 2.26 | 2.60 | 3.32 | 5.32 |
| 125 | | 2.26 | 2.44 | 3.02 | 5.05 |
| 150 | | | 2.39 | 2.75 | 5.66 |

**Figure 4.12** Simulated H/D values for configuration A at 22 locations around the treatment nozzle are presented as a function of distance of the neutron receptor to the isocenter (r) and angle (θ) with respect to initial beam axis. H/D values decrease with increasing r and  θ.

**Figure 4.13** Simulated H/D values for configuration B at 22 locations around the treatment nozzle are presented as a function of distance of the neutron receptor to the isocenter (r) and angle (θ) with respect to initial beam axis. H/D values decrease with increasing r and θ.
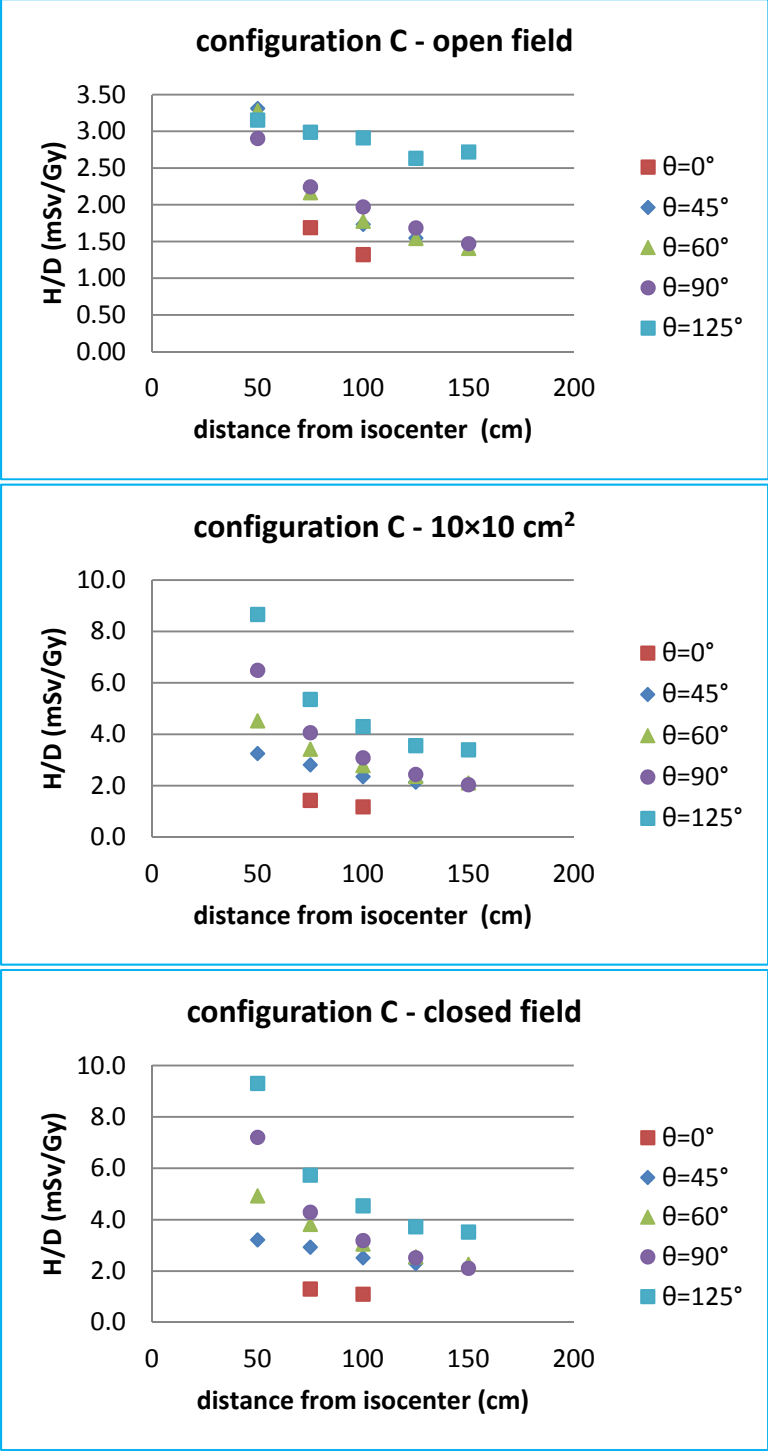
**Figure 4.14** Simulated H/D values for configuration C at 21 locations around the treatment nozzle are presented as a function of distance of the neutron receptor to the isocenter (r) and angle (θ) with respect to initial beam axis. H/D values decrease with increasing r and θ.
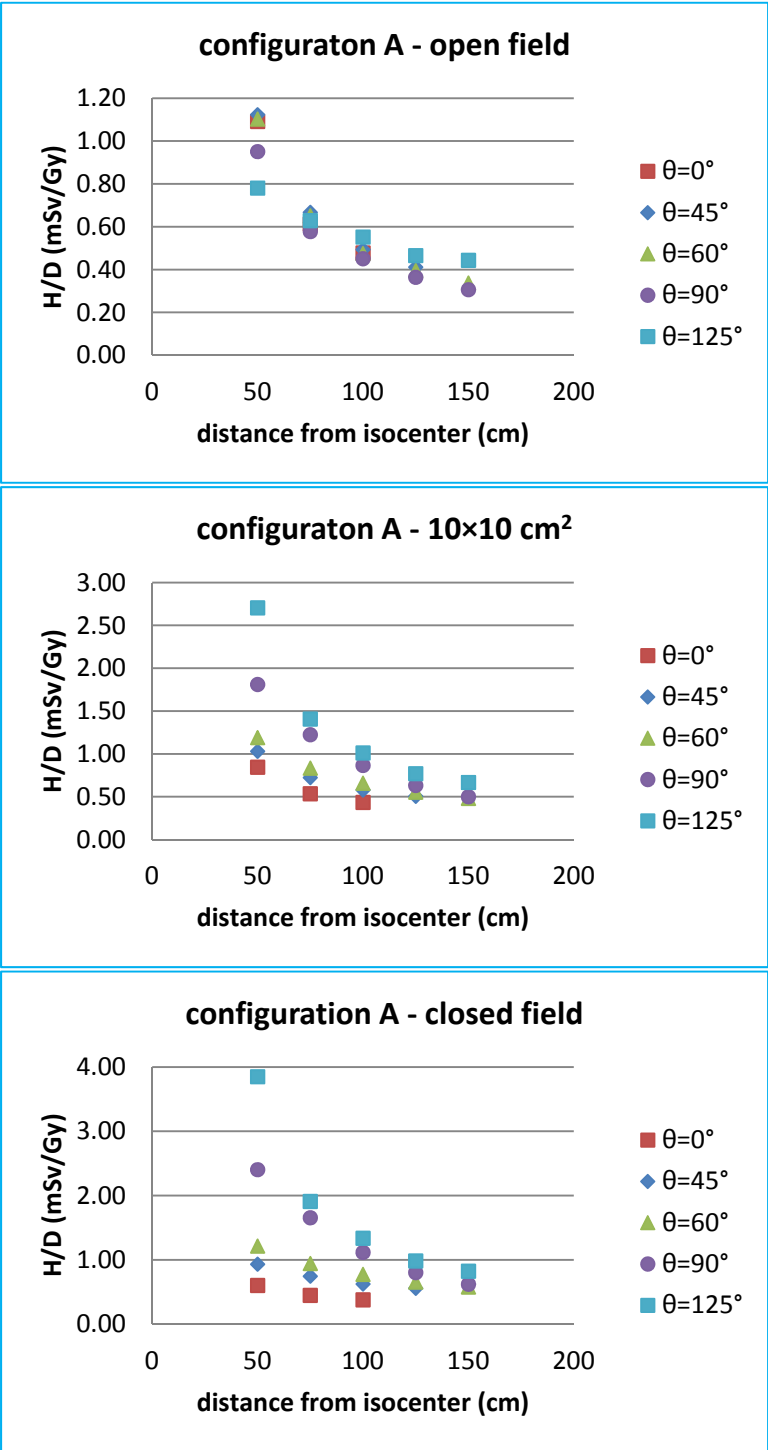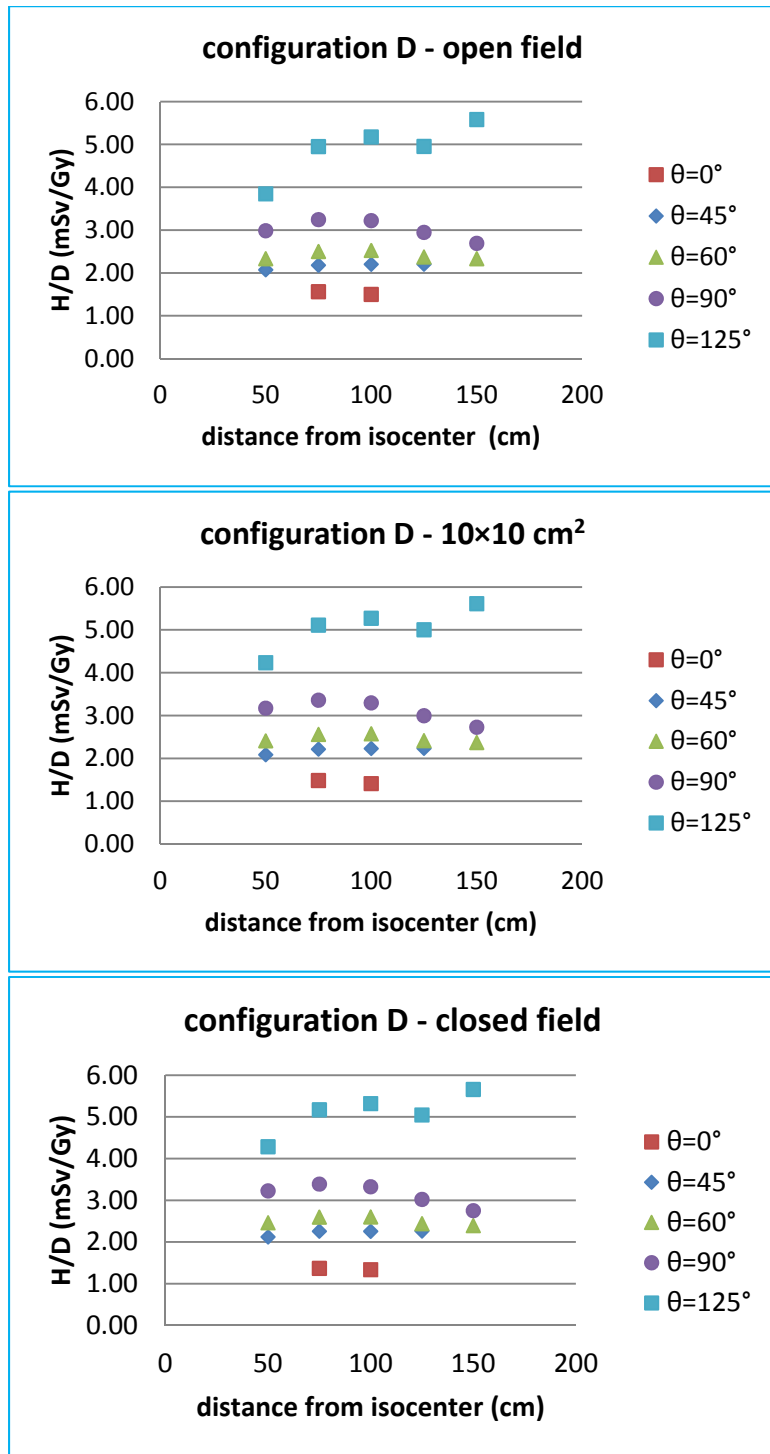
**Figure 4.15**  Simulated H/D values for configuration D at 21 locations around the treatment nozzle are presented as a function of distance of the neutron receptor to the isocenter (r) and angle (θ) with respect to initial beam axis. H/D values decrease with increasing r and  θ.
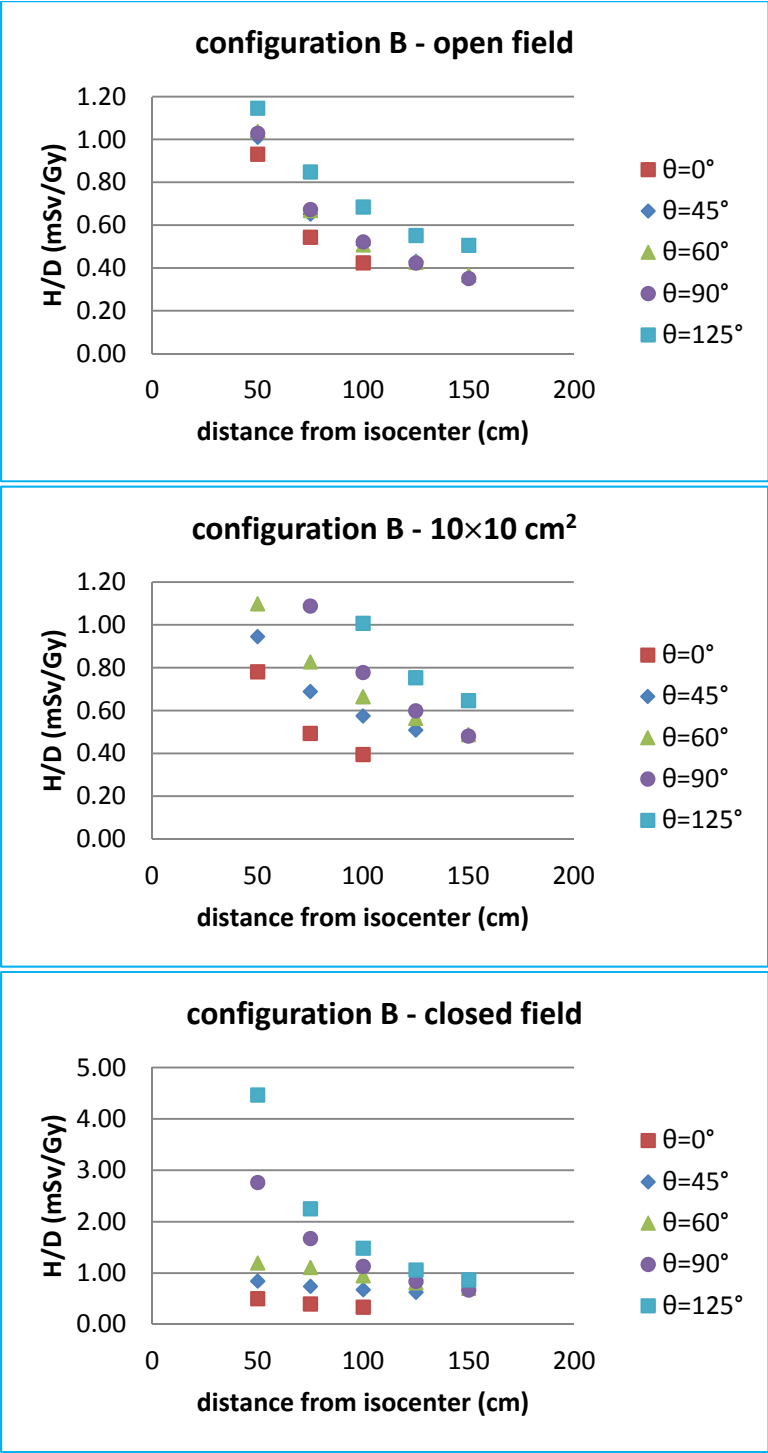
## 4.3.3.1    H/D Values as a Fuction of Distance and Angle

For the deep penetration configurations, i.e. configuration A – C, simulated H/D values decrease with increasing distance from the isocenter (r) but increase with increasing angle from the inicitial proton beam direction (θ), with a few exceptions.  Since these results were determined with a water phantom present, the influence of water phantom should be taken into account.  Figure 4.17 left column showed the $H(E_n)/D$ spectra as a function of distance from the isocenter at five angles for configuration A open field when the water phantom was considered.  The $H(E_n)/D$ spectra for excluding the water phantom was plotted in the right column to help illustrate how H/D values change as a function of distance and angle.  As discussed previously, neutrons from evaporation processes and intranuclear cascade processes were the dominant components contributed to the total H/D values.  Therefore, all $H(E_n)/D$ spectra were plotted to only include neutron energy from 1 keV 1000 MeV.

The $H(E_n)/D$ spectra obtained from simulations with the water phantom excluded were the  neutron dose equivalents from neutrons that did not go through the water phantom.  Both evaporation and cascade neutron peaks increased with angle from the initial beam plane (θ).  By comparing the left column (including water phanton) and the right column (excluding water phantom), the significance of the water phantom as a function of θ can be understood.

Because cascade neutrons emissions are forward peaked in the direction with respect to the incident proton beam axis,   the $H(E_n)/D$ attributed to cascade neutrons decreases dramatically as distance increases.  This phenomenon is most significant at positions along the incident beam direction, and the significance diminishes as angle increases.

On the other hand, evaporation neutrons emissions are isotropical. Therefore, the $H(E_n)/D$ attributed to this compoment varies with the distances between neutron sources and neutron receptors. This can be seen clearly in Figure 4.18, where the $H(E_n)/D$ spectra in Figure 4.17 are presented as a function of angle with respect to incident beam axis. Consequently, the slightly increase in magnitude in $H(E_n)/D$ are seen at large angles. For neutrons generated in the beam-line, at a given isocenter-to-neutron-receptor-distance (r), the distance between the neutron recepter and the neutron source (nozzle) decreased as $\theta$ increases. For evaporation neutrons generated inside the water phantom, since the distance of the neutron sources to the neutron receptors are the same for each angle at certain distance from the isocenter (r), neutron dose equivalent are the same to each neutron receptor. However, in configuration A with $\theta = 0°$, since the large water phantom attenuated the cascade neutrons to lower energies, the end result of the distribution and magnitude of $H(E_n)/D$ from evaporation neutrons increased slightly as the distance from isocenter (r) increased. Therefore, the H/D values decrease with increasing distance from the isocenter (r). The H/D values increase with increasing angle from the inicitial proton beam direction ($\theta$). Two exceptions are seen where H/D decreased as $\theta$ increased from 90° to 45°, including at r = 50 cm to r = 125 cm in configuration A open field and r = 50 cm in configuration C open field. This is because for deep range configurations, incident protons that reach the water phantom still possess high energies and could introduce high energy neutrons. In addition, since the isocenter was defined at the center of SOBP, the amount of water allowed for moderating neutrons originated from the nozzle is also a factor. The H/D values are thus also affected by field sizes and distance between nozzle and the water phantom. As seen in Figure 4.16, the iscocenter in configuration A and C are closer to the nozzle (33.7 cm vs 42 cm in B and D). For configuration A open field, since the distance from the downstream face of the applicator and the upstream face of the water

phantom is shorter, a large fraction of neutrons generated in the nozzle most likely entered the

water phantom, and subsequently were attenuated by it.  Since the proton range in water for

this configuration is 32 cm, protons that entered the water phantom had energies to produce

high energy neutrons.  Based on the two reasons, neutrons were likely to be moderated to

evaporation neutrons energies for isotropic emission toward the downstream side of water

phantom.  As a result, H/D values are higher at $\theta = 45°$ than at $\theta = 90°$.  A similar mechanism can

be used to explain configuration C.  The isocenter in configuration C was 20 cm from the

upstream face of the water phantom, and the distance between applicator and water were

slightly longer than configuration A.  Therefore, H/D decreased as $\theta$ increased only extended to

neutron receptors at r = 50 cm.
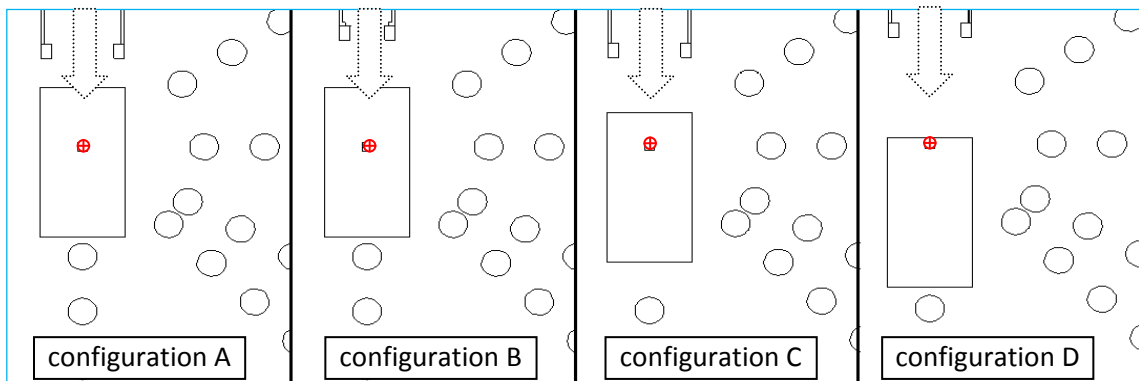


**Figure 4.16**  Schematic simulation drawings for configuration A – D to show the relative locations of between the beam-line components, the water phantom (square box) and neutron receptors (circle). The incident proton beam direction is shown in dashed arrow; the red circle cross is the isocenter.  (Note: Figure not to scale).

Evaparation neutrons and cascade neutrons behave the same way in configuration D; therefore, H/D values increased with increasing angle with respect to the initial proton beam axis.  However, for such a limited range configuration, evaporation neutrons were dominant to

81

the total H/D as seen in Figure 4.19.  Although $H(E_n)/D$ came from cascade neutrons decreased with increaing distance from the isocenter at a certain angle direction, the effect is small that total H/D did not change as distance from the isocenter changed.  One exception was at $\theta = 125°$, H/D values were increasing, as the distance from isocenter (r) inceasing.  This is because at the direction of  $\theta = 125°$, as r increases, neutron receptor's location is closer to upstream of the treatment nozzle, where neutron production is greater for this configuration compared to locations which are downstream and closer to the isocenter.

$H(E_n)/D$ spectra as function of distance from isocenter (r) for configuration B and C are included in Appendix A.
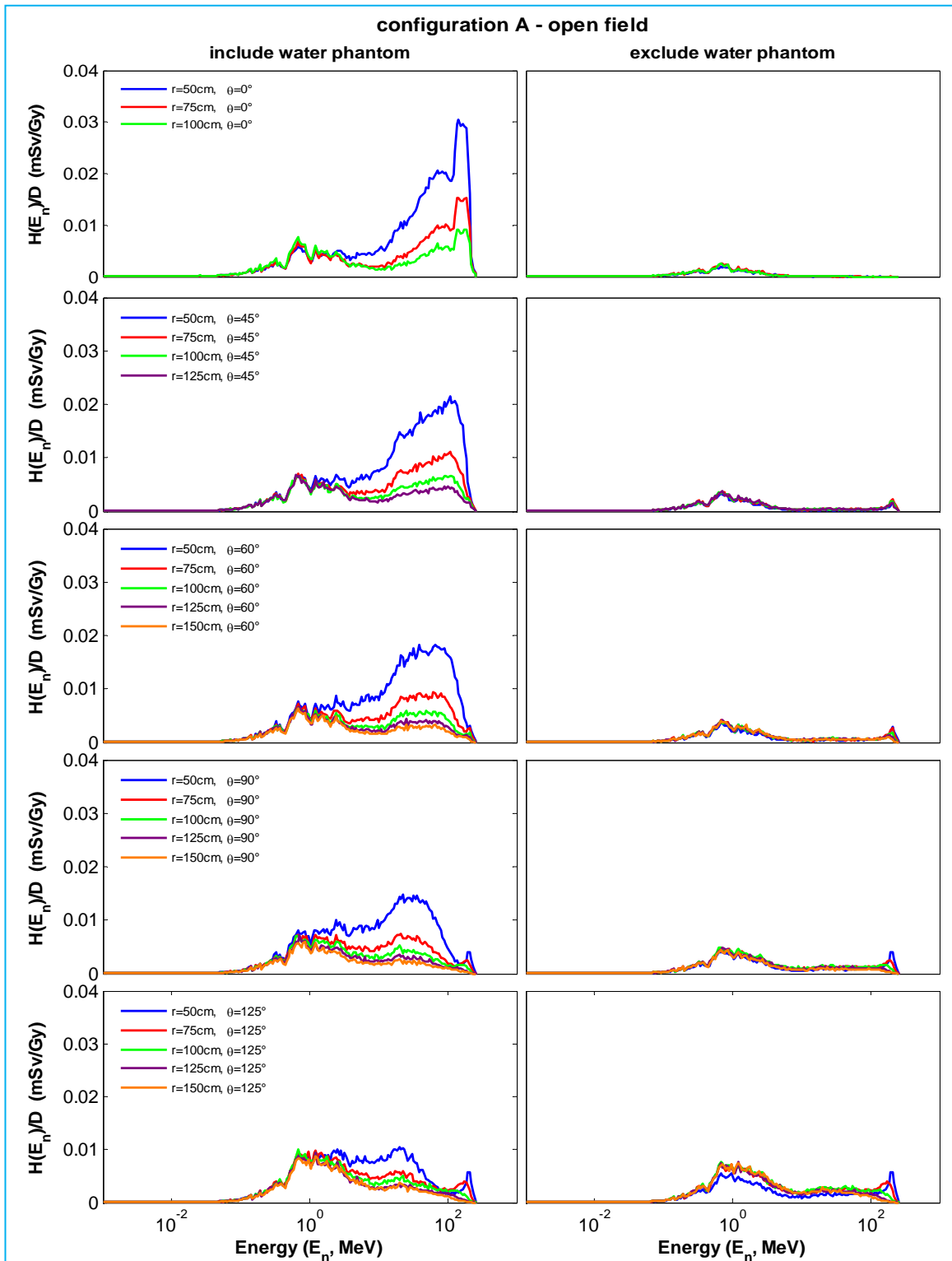
**Figure 4.17** Simulated H(E$_n$)/D spectra as a function of distance (r) at five different angle (θ) for configuration A open fields. The left column shows the spectra when including the water phantom. The right column shows the spectra when excluding the water phantom.
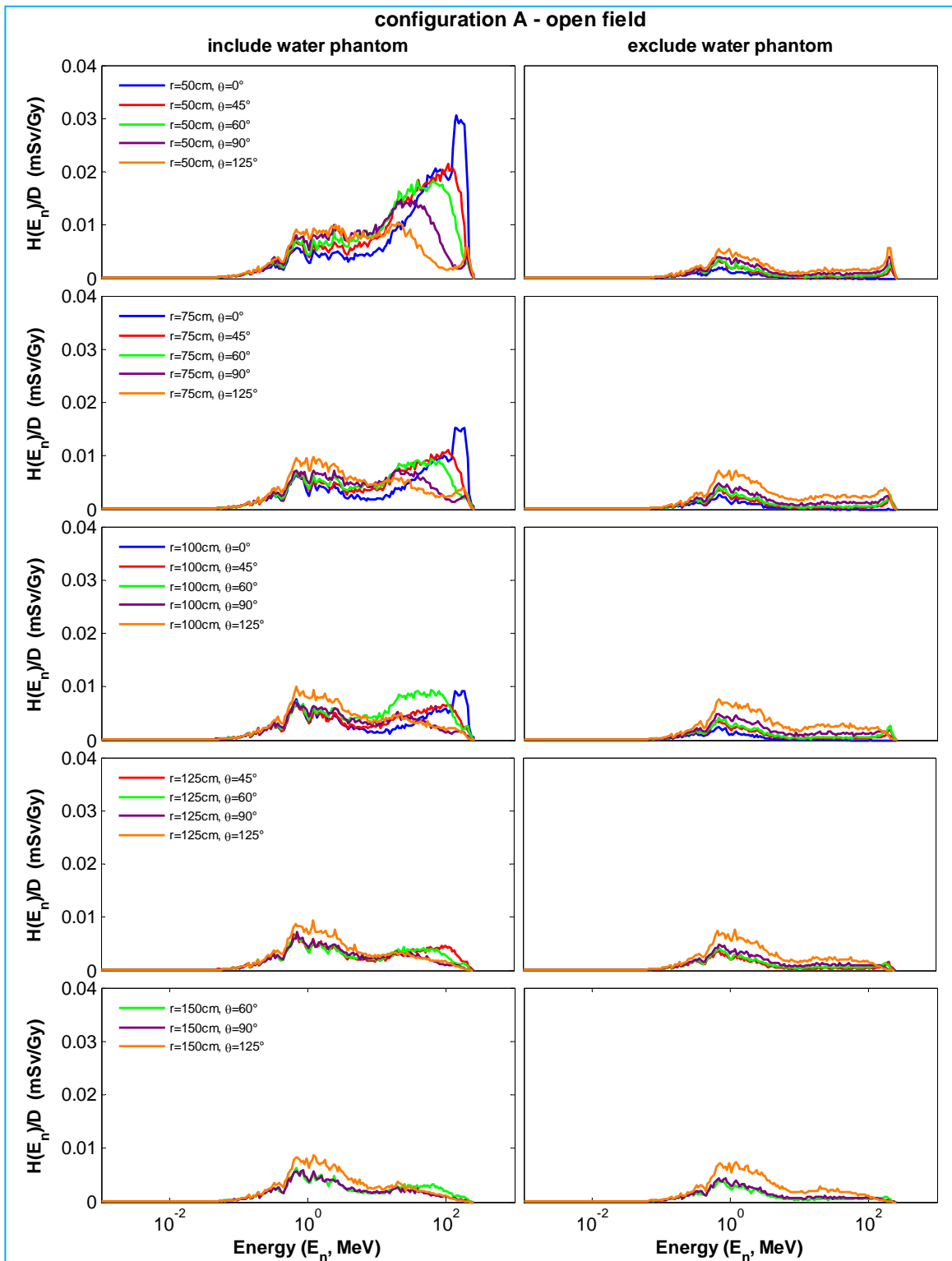
**Figure 4.18** Simulated $H(E_n)/D$ spectra as a function of angles ($\theta$) with respect to the incident proton beam axis at 5 different isocenter-to-neutron-receptor distance (r) for configuration A open fields. The left column shows the spectra when including the water phantom. The right column shows the spectra when excluding the water phantom.
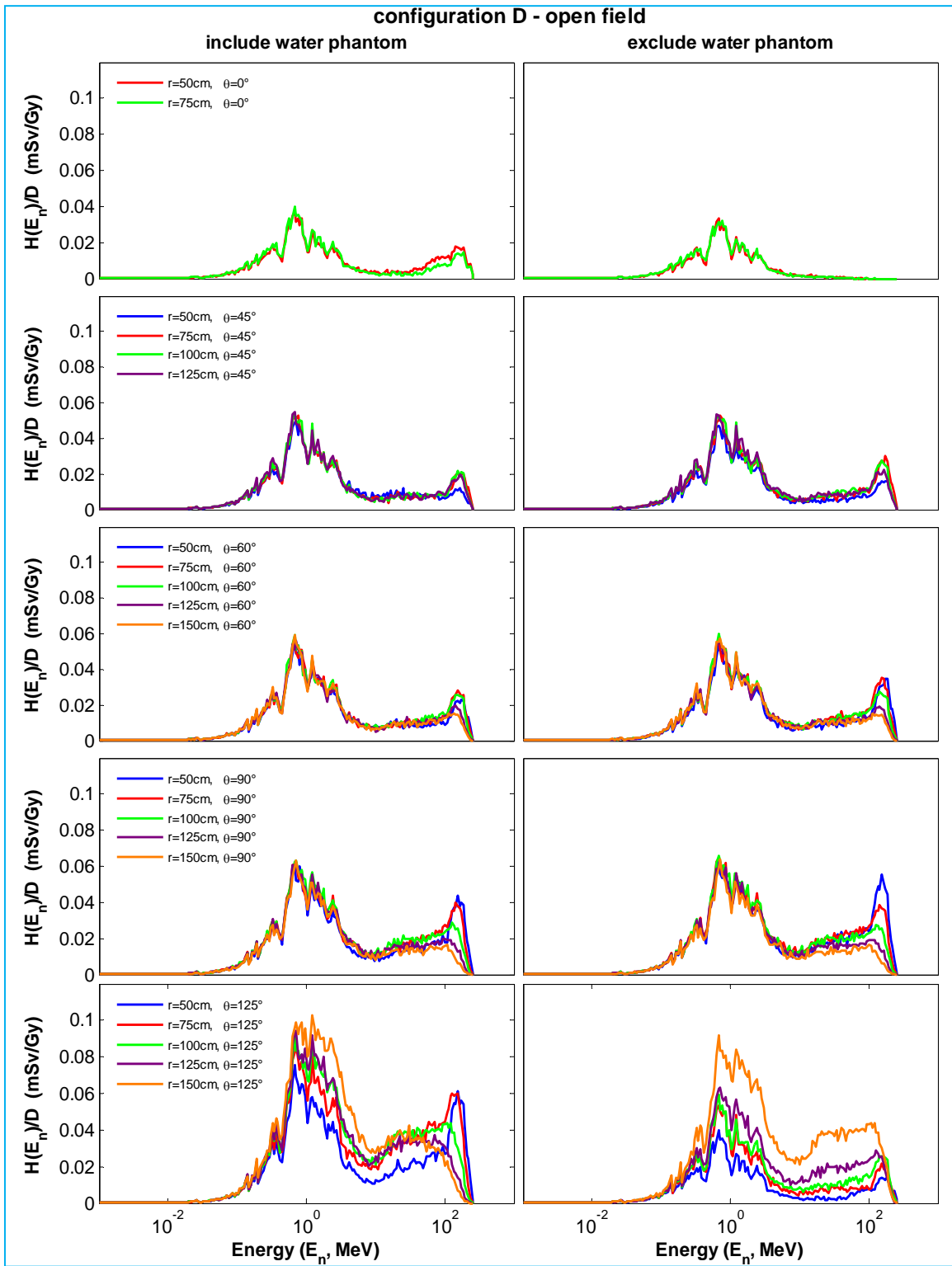
**Figure 4.19** Simulated $H(E_n)/D$ spectra as a function of distance (r) at five different angles (θ) for configuration D open fields. The left column shows the spectra when including the water phantom. The right column shows the spectra when excluding the water phantom.

## 4.3.3.2    H/D Values as a Fuction of Aperture Field Size

Three field sizes were considered, including a $0 \times 0$ cm$^2$ (closed field), $10 \times 10$ cm$^2$, and an open field.  The H/D values increased with field sizes for locations on the initial proton beam axis.  For the other locations as specified by distance from isocenter (r) and angle with respect to the incident proton beam plane ($\theta$), H/D values decreased as field sizes increased for most cases.  The fluctuation of total H/D is the result of two competing effects within the final collimator and the influence from the water phantom.  Since the influence of the water phantom was discussed in previous section, this section focuses on the effects of final collimators.

The final collimators had two different attributes.  First, as a shielding for neutrons produced in the upstream components in the nozzle.  Second, as a neutron source where neutrons were produced due to the proton interaction with collimator.  As the field size increased, a greater fraction of protons escape without producing neutrons in the final collimators.  In other words, a greater fraction of protons entered the water phantom and generated neutrons.  In addition, as the field size increase, neutron shielding was reduced so that a greater fraction of produced neutrons from the upstream components escaped.  For locations on the initial proton beam direction ($\theta = 0°$), as the field size increased, the cross sections of escaping protons and escaping produced neutrons were larger than the other positions.  These escaped protons interacted with the water phantom and produced neutrons.  Therefore, H/D values increased as field sizes increased as shown in Figure 4.20a, where the H/D at r = 100 cm, $\theta = 0°$ is plotted as a function of aperture sizes for all configurations.
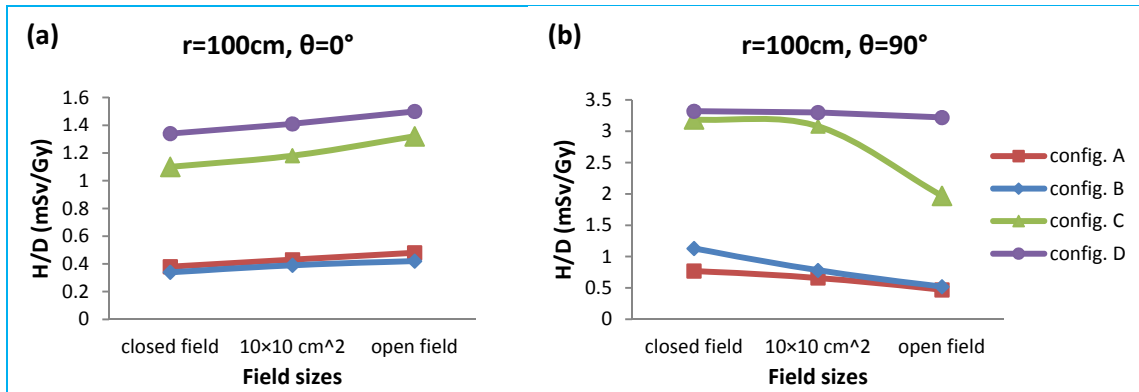
**Figure 4.20** H/D values as a function of field sizes for neutron receptors located at 100 cm away from isocenter (r = 100 cm) in all configurations. (a) shows H/D increase with field sizes when the neutrons are at the incident proton plane ($\theta$ = 0°). (b) is for $\theta$ = 90°, where H/D values decrease as field sizes increase.

Figure 4.20b shows H/D values as a function of aperture sizes for the standard reference point for determining dose to patient, i.e. r =100 cm and $\theta$ = 90°. The detail $H(E_n)/D$ spectra at each location for all three field sizes are plotted in Figure 4.21 − 4.24 for configuration A − D respectively.
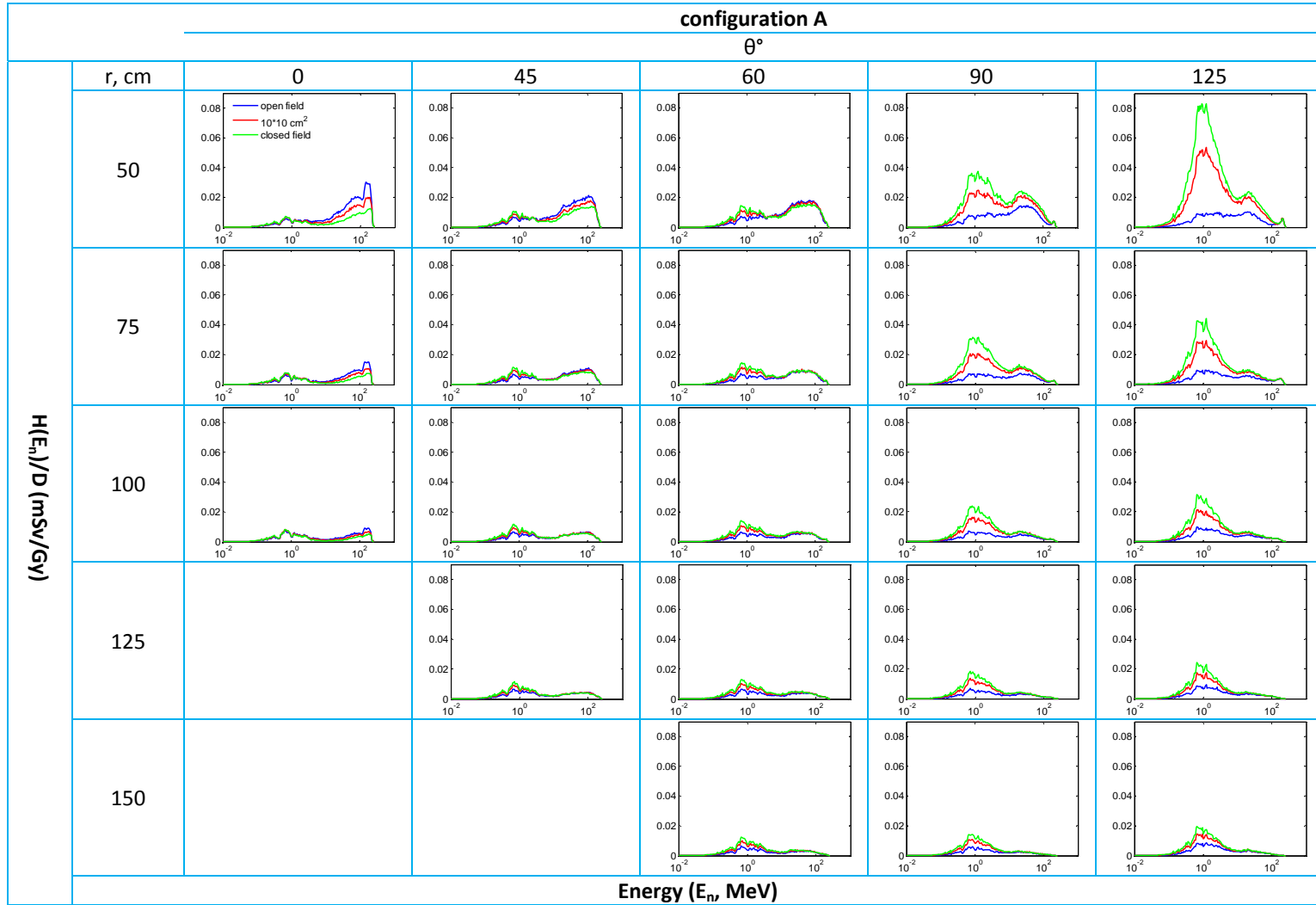
**Figure 4.21**  Simulated H(En)/D spectra as a function of field sizes for configuration A.
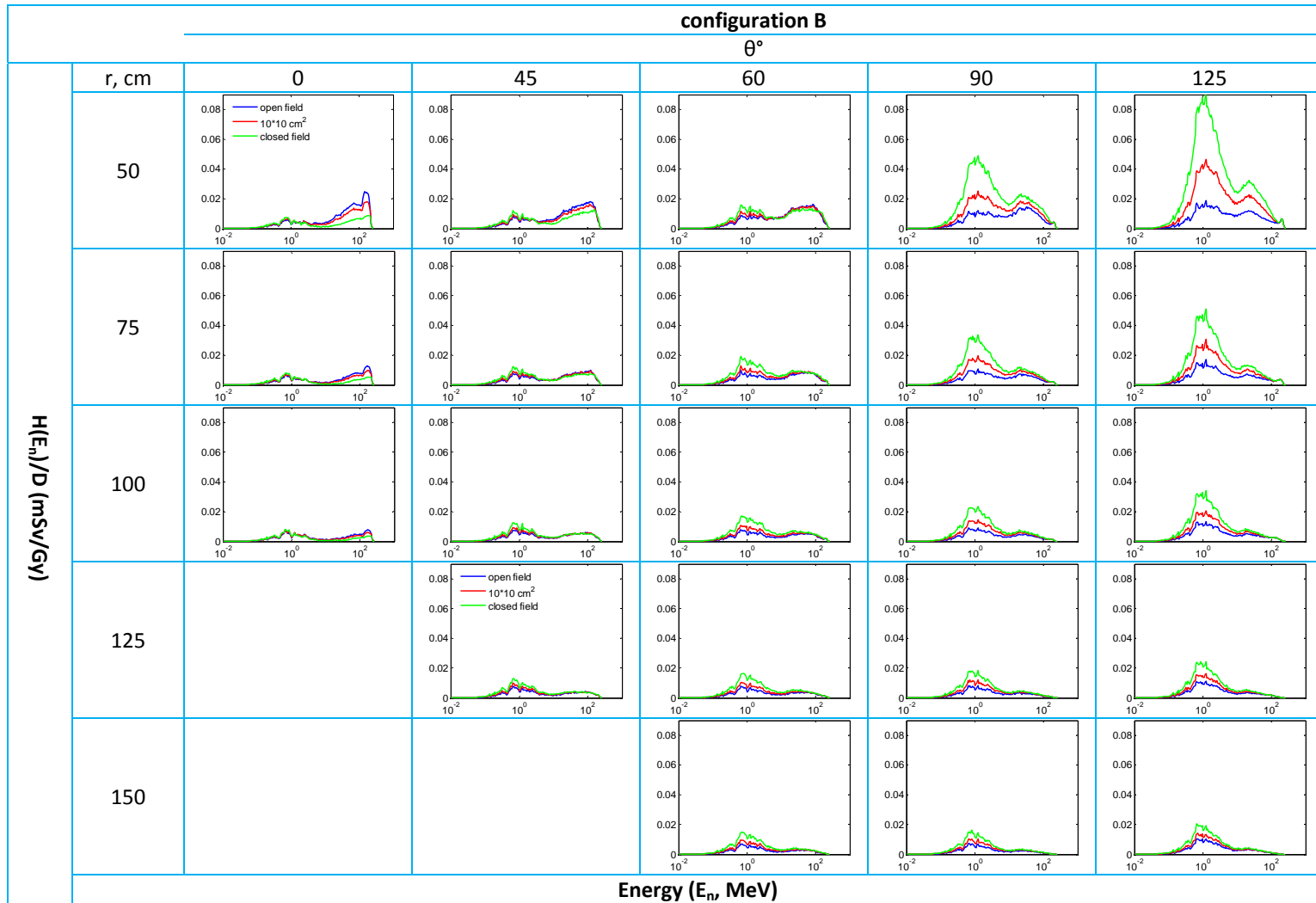
**Figure 4.22** Simulated H(En)/D spectra as a function of field sizes for configuration B.
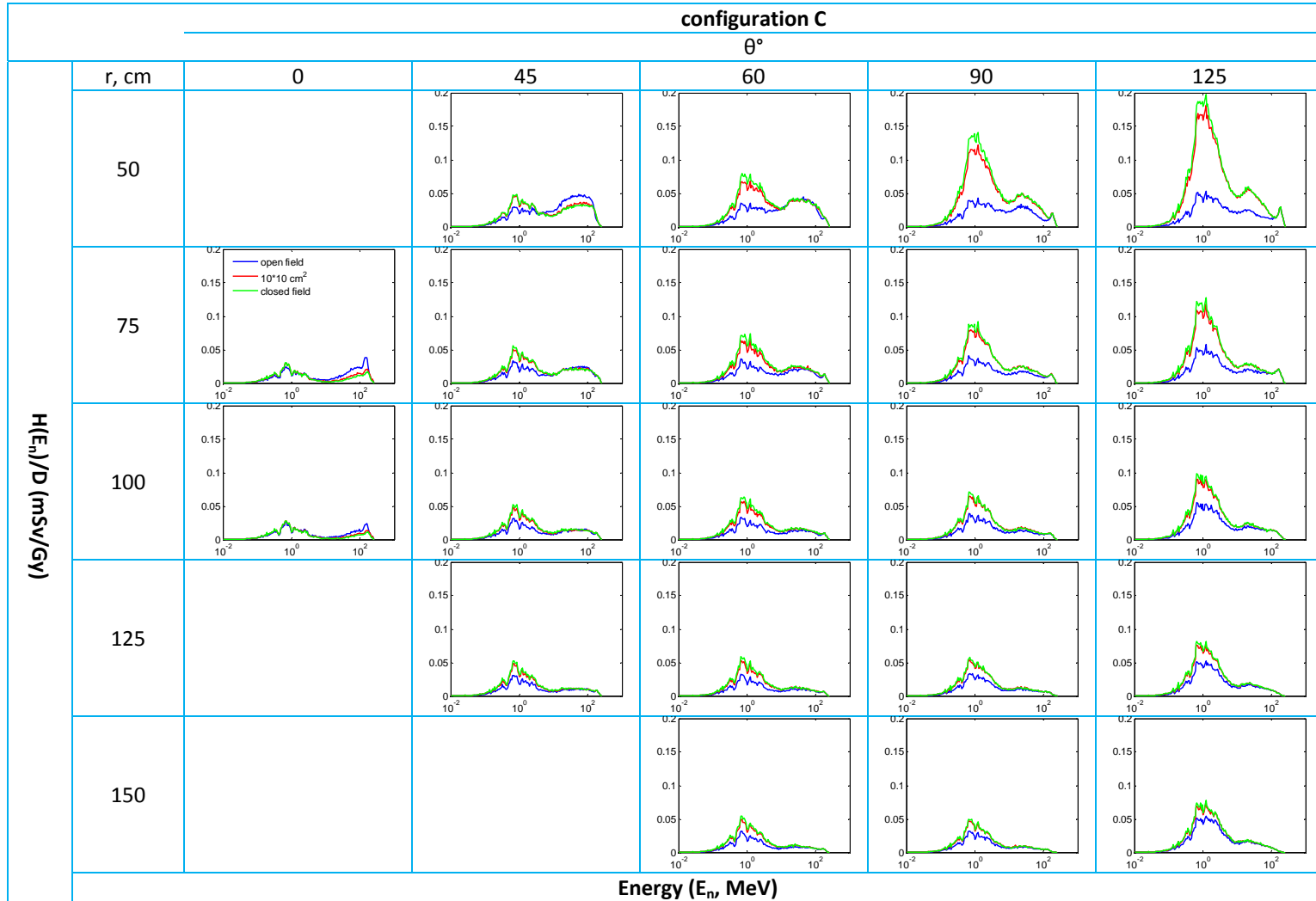
**Figure 4.23** Simulated H(En)/D spectra as a function of field sizes for configuration C.
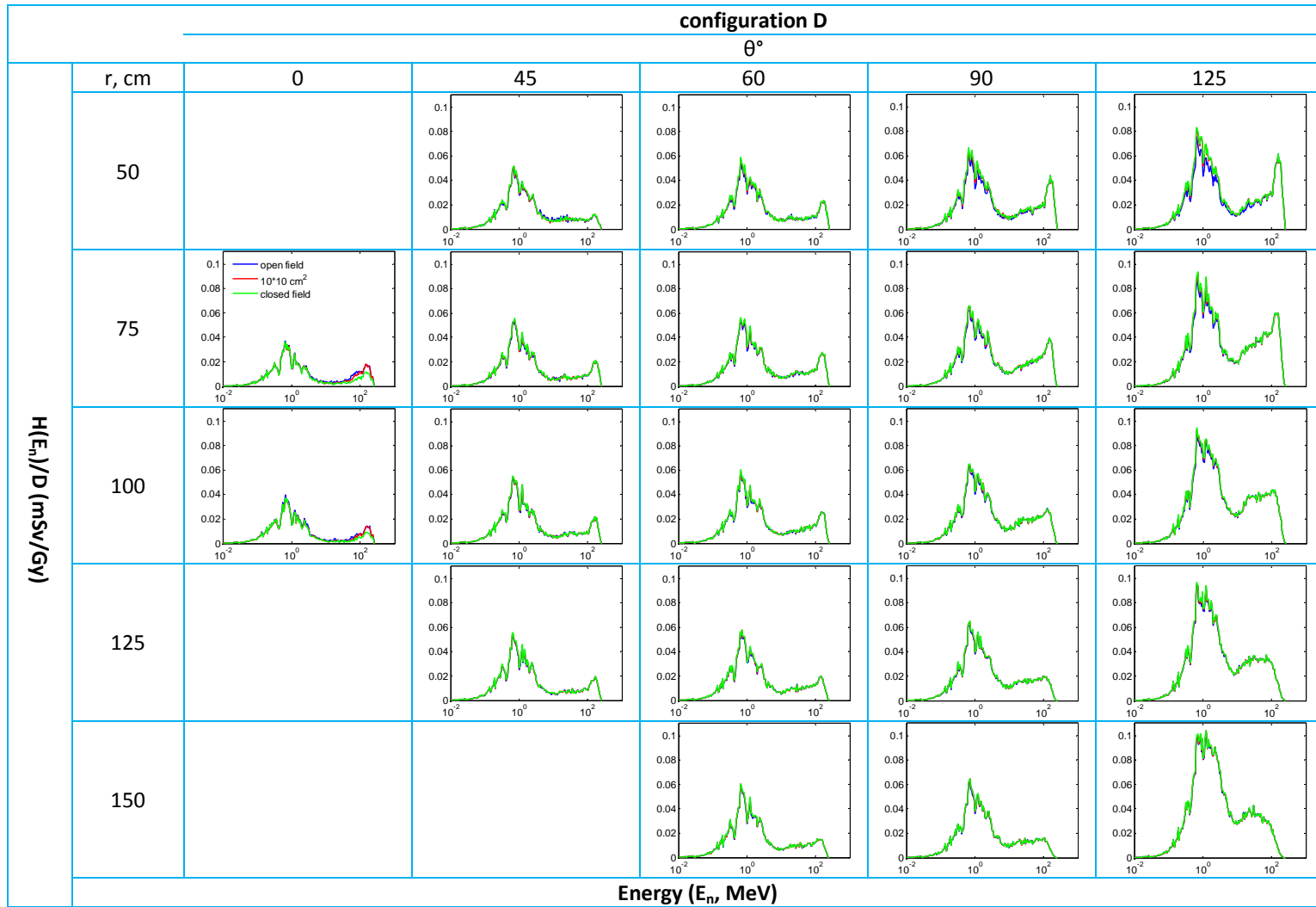
**Figure 4.24**   Simulated H(En)/D spectra as a function of field sizes for configuration D.

### 4.3.4  H/D Values as a Function of Treatment Nozzle Position

The treatment nozzle, i.e. extension box along with the applicators, can be retracted during treatments so that patient specific compensators can be as close as needed to be for each patient.  The nozzle position is defined as the distance (d) between the downstream face of the applicators from the isocenter, and can be anywhere from 7 to 42 cm (fully extended position to fully retracted position).  Since a fraction of neutron dose equivalents came from neutrons generated in the nozzle, treatment nozzles were set to; 7, 14, 21, 35, 42 cm, whenever possible for configurations B – D open field to evaluate the changes of H/D values.  The results are presented in Table 4.8 – 4.11 for configuration B – D respectively.  The H/D values are found to decrease as treatment nozzle moves away from the isocenter.  This is due to when treatment nozzle position advances, neutron sources originate at nozzle are moved away from the neutron receptors.  As shown in Figure 4.25, the effect is diminished as neutrons receptors' distances from the isocenter increased.
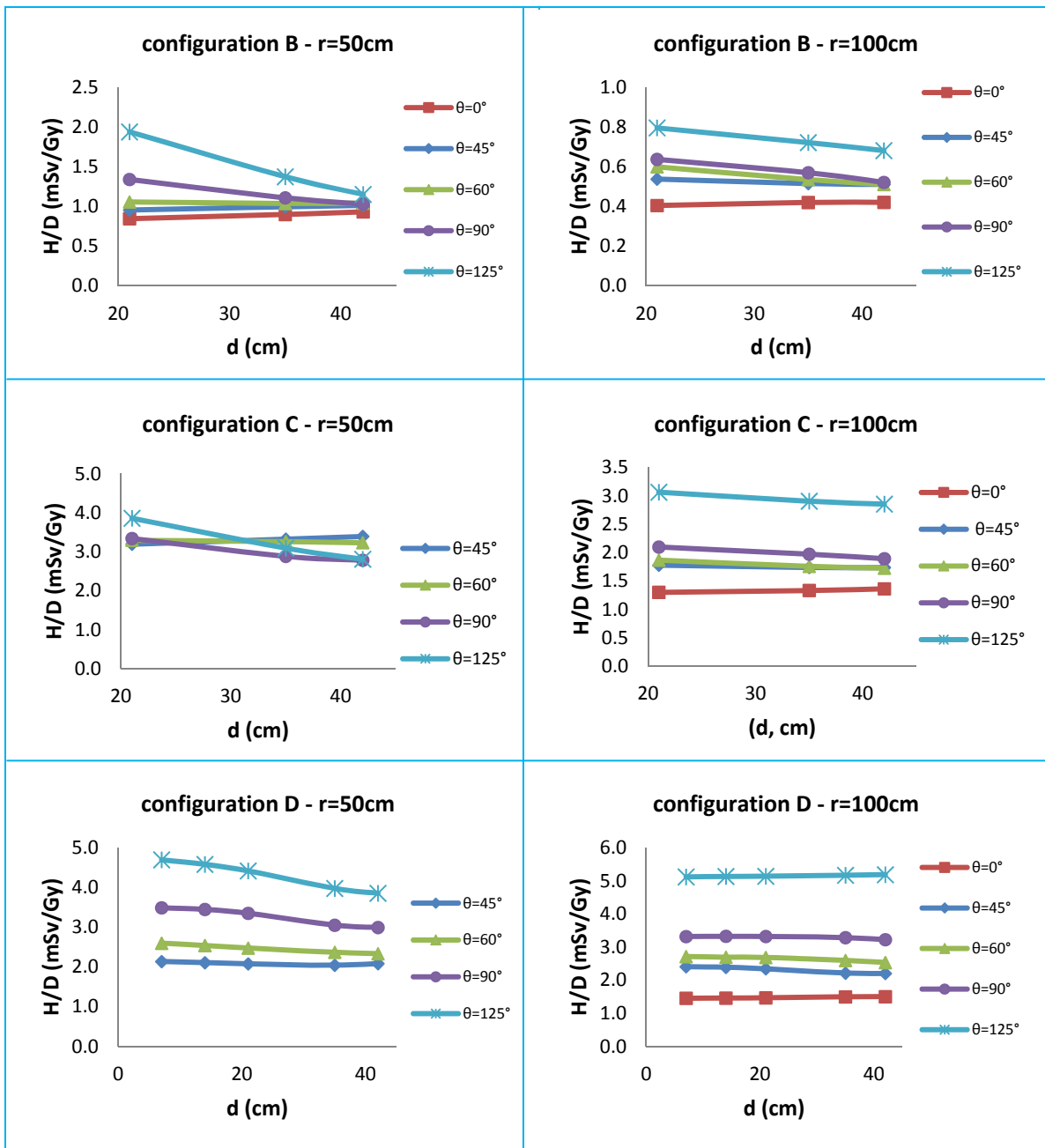
**Figure 4.25** H/D values as a function of the treatment nozzle position for configuration B – D open fields. Where d is the distance between the downstream face of the applicator to the isocenter. Where r is the neutron receptor distance from the isocenter. In general, H/D decreases as d increases.

**Table 4.8** Simulated H/D values as a function of treatment nozzle position (d) for configuration B. Where r is the neutron receptor's distance from the isocenter and θ is the angle with respect to the initial proton beam axis.

| configuration B – open field | | | | | |
|---|---|---|---|---|---|
| H/D (mSv/Gy) | | | | | |
| | angle (θ°) | | | | |
| Distance (r, cm) | 0 | 45 | 60 | 90 | 125 |
| **d = 21 cm** | | | | | |
| 50 | 0.84 | 0.95 | 1.05 | 1.34 | 1.94 |
| 75 | 0.51 | 0.66 | 0.75 | 0.86 | 1.08 |
| 100 | 0.40 | 0.54 | 0.60 | 0.64 | 0.79 |
| 125 | | 0.47 | 0.50 | 0.49 | 0.62 |
| 150 | | | 0.43 | 0.40 | 0.55 |
| **d = 35 cm** | | | | | |
| 50 | 0.90 | 0.99 | 1.04 | 1.11 | 1.37 |
| 75 | 0.53 | 0.66 | 0.69 | 0.74 | 0.96 |
| 100 | 0.42 | 0.51 | 0.53 | 0.57 | 0.72 |
| 125 | | 0.44 | 0.45 | 0.45 | 0.58 |
| 150 | | | 0.39 | 0.37 | 0.52 |
| **d = 42 cm** | | | | | |
| 50 | 0.93 | 1.01 | 1.04 | 1.03 | 1.15 |
| 75 | 0.54 | 0.65 | 0.67 | 0.67 | 0.85 |
| 100 | 0.42 | 0.51 | 0.51 | 0.52 | 0.68 |
| 125 | | 0.43 | 0.43 | 0.42 | 0.55 |
| 150 | | | 0.37 | 0.35 | 0.51 |

**Table 4.9** Simulated H/D values as a function of treatment nozzle position (d) for configuration C. Where r is the neutron receptor's distance from the isocenter and θ is the angle with respect to the initial proton beam axis.

| configuration C – open field | | | | | |
|---|---|---|---|---|---|
| H/D (mSv/Gy) | | | | | |
| | angle (θ°) | | | | |
| Distance (r, cm) | 0 | 45 | 60 | 90 | 125 |
| **d = 21 cm** | | | | | |
| 50 | | 3.19 | 3.30 | 3.34 | 3.86 |
| 75 | 1.66 | 2.21 | 2.28 | 2.47 | 3.35 |
| 100 | 1.30 | 1.78 | 1.87 | 2.10 | 3.06 |
| 125 | | 1.62 | 1.60 | 1.78 | 2.72 |
| 150 | | | 1.46 | 1.54 | 2.78 |
| **d = 33.7 cm** | | | | | |
| 50 | | 3.31 | 3.28 | 2.90 | 3.15 |
| 75 | 1.69 | 2.22 | 2.17 | 2.25 | 2.99 |
| 100 | 1.32 | 1.73 | 1.78 | 1.97 | 2.91 |
| 125 | | 1.55 | 1.54 | 1.69 | 2.63 |
| 150 | | | 1.41 | 1.47 | 2.72 |
| **d = 35 cm** | | | | | |
| 50 | | 3.32 | 3.26 | 2.88 | 3.10 |
| 75 | 1.70 | 2.21 | 2.15 | 2.21 | 2.96 |
| 100 | 1.33 | 1.74 | 1.76 | 1.97 | 2.90 |
| 125 | | 1.54 | 1.53 | 1.69 | 2.62 |
| 150 | | | 1.40 | 1.47 | 2.71 |

**Table 4.10** Simulated H/D values as a function of treatment nozzle position (d) for configuration D. Where r is the neutron receptor's distance from the isocenter and θ is the angle with respect to the initial proton beam axis.

| configuration D – open field | | | | | |
|---|---|---|---|---|---|
| H/D (mSv/Gy) | | | | | |
| | angle (θ°) | | | | |
| Distance (r, cm) | 0 | 45 | 60 | 90 | 125 |
| **d = 7 cm** | | | | | |
| 50 | | 2.13 | 2.59 | 3.48 | 4.69 |
| 75 | 1.56 | 2.39 | 2.77 | 3.50 | 5.17 |
| 100 | 1.45 | 2.40 | 2.71 | 3.31 | 5.11 |
| 125 | | 2.39 | 2.49 | 2.97 | 4.86 |
| 150 | | | 2.43 | 2.69 | 5.52 |
| **d = 14 cm** | | | | | |
| 50 | | 2.10 | 2.54 | 3.44 | 4.58 |
| 75 | 1.56 | 2.34 | 2.76 | 3.49 | 5.17 |
| 100 | 1.46 | 2.38 | 2.69 | 3.32 | 5.13 |
| 125 | | 2.38 | 2.48 | 2.98 | 4.87 |
| 150 | | | 2.42 | 2.69 | 5.54 |
| **d = 21 cm** | | | | | |
| 50 | | 2.07 | 2.47 | 3.35 | 4.41 |
| 75 | 1.56 | 2.29 | 2.72 | 3.46 | 5.18 |
| 100 | 1.47 | 2.34 | 2.68 | 3.32 | 5.13 |
| 125 | | 2.36 | 2.48 | 2.97 | 4.89 |
| 150 | | | 2.41 | 2.69 | 5.55 |
| **d = 35 cm** | | | | | |
| 50 | | 2.04 | 2.37 | 3.05 | 3.97 |
| 75 | 1.56 | 2.21 | 2.55 | 3.35 | 5.08 |
| 100 | 1.49 | 2.21 | 2.59 | 3.28 | 5.16 |
| 125 | | 2.25 | 2.43 | 2.97 | 4.92 |
| 150 | | | 2.38 | 2.69 | 5.58 |
| **d = 42 cm** | | | | | |
| 50 | | 2.08 | 2.33 | 2.99 | 3.85 |
| 75 | 1.56 | 2.18 | 2.5 | 3.25 | 4.95 |
| 100 | 1.5 | 2.2 | 2.53 | 3.22 | 5.18 |
| 125 | | 2.21 | 2.37 | 2.95 | 4.95 |
| 150 | | | 2.34 | 2.69 | 5.58 |

## 4.3.5      Influence of Additional Shielding Materials on H/D Values

The H/D values were determined when additional shielding box made of either 5% borated polyethylene (BPE) or nickel added around the treatment nozzle.  The results for position 1 – 3 are listed in Table 4.11.  Figure 4.26 shows the trend of change for H/D values at the other positions.  Two different lengths of shielding box were considered.  The shorter box covered from the applicators up to the theta carriage (Figure 4.7), listed as BPE and Ni in Table 4.11.  The longer one covered from the applicators to the target, listed as extended BPE and extended Ni in Table 4.11.  Results show that both short length BPE shielding box and Ni shielding box did not affect the H/D values in any positions (<1%).  An interesting aspect is the H/D values for BPE and Ni are similar for all positions.  One possible reason is that for an open field configuration with no brass apertures present, the neutron sources in the nozzle were the range modulator and the secondary scatterer, which contain high Z materials.  Therefore, shielding around the theta carriage was not ideal.  The other reason is that the thickness of the box was only 1 inch, which might not be sufficient for high energy neutrons generated in the nozzle.

Results show that extended shielding boxes lowered the H/D values for all positions.  The extended BPE shielding box was more effective (<25%) than extended Ni box (<20%).

**Table 4.11**    The H/D values at position 1 – 3 for configuration C open field when additional shielding materials are added around the treatment nozzle.  BPE and Ni are short length shielding boxes covering the applicators up to the theta carriage; whereas extended BPE and extended Ni cover from applicator to the target.

| | H/D (mSv/Gy) | | | | |
|---|---|---|---|---|---|
| Position | no shielding | BPE | Ni | extended BPE | extended Ni |
| 1 | 1.70 | 1.69 | 1.69 | 1.27 | 1.49 |
| 2 | 2.78 | 2.78 | 2.78 | 2.03 | 2.40 |
| 3 | 0.19 | 0.19 | 0.19 | 0.15 | 0.19 |
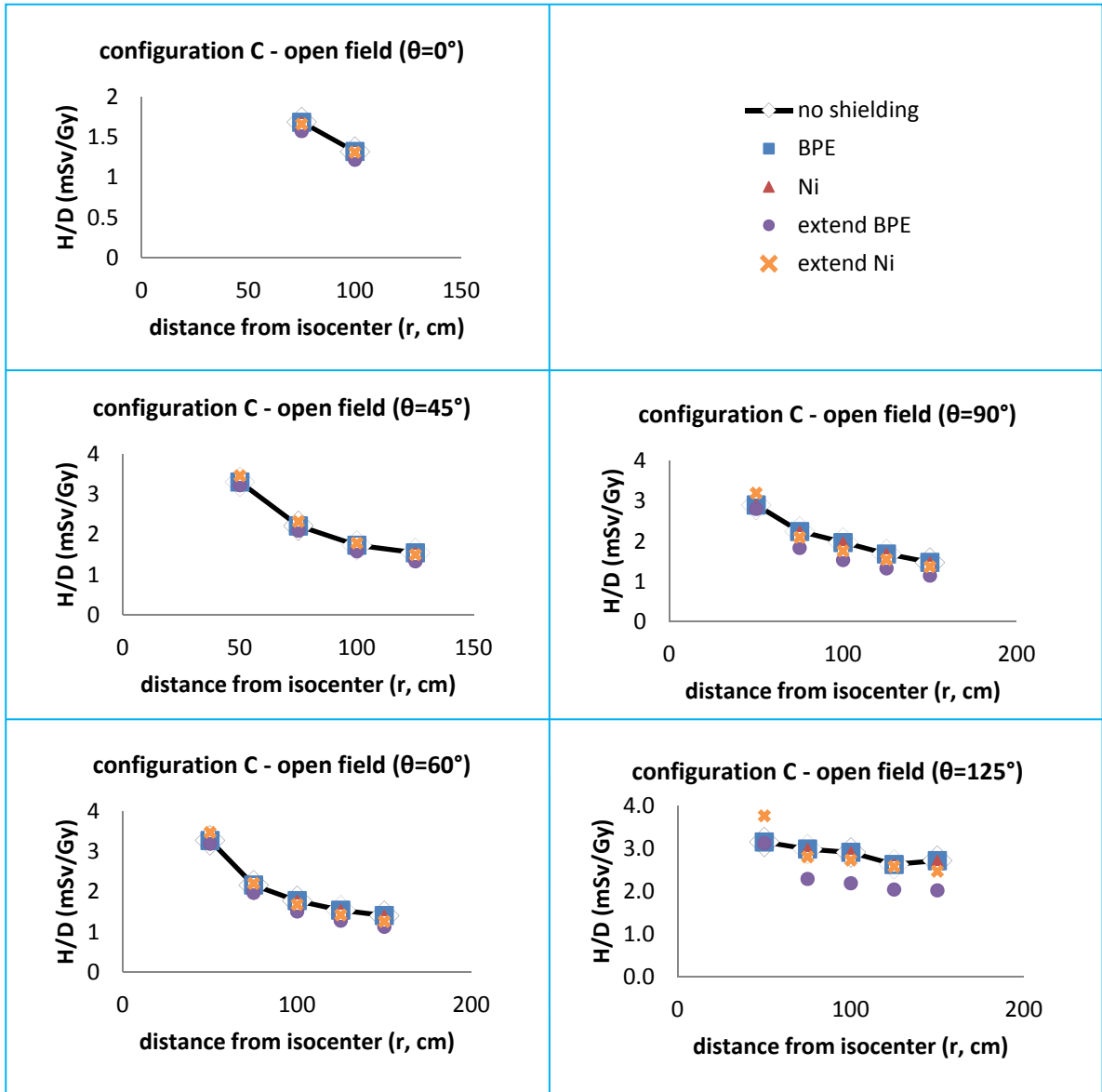
**Figure 4.26** H/D values as a function of distance from isocenter (r) around treatment nozzle for configuration C open field when additional shielding boxes are present. θ is the angle with respect to the incident proton beam axis. Extended BPE shielding box is the most sufficient design among the four conditions considered.

## 4.3.6    Comparison of the One Step and Multiple Step Methods

Since the range modulator wheels (RMW) are rotating 360° with a certain speed during beam delivery, the most appropriate method to calculate the neutron dose equivalent (H) from this accelerator using MCNPX is to determine H one degree at a time for 360 degrees and then sum the angle-weighted results.  However, this is not practical as the computation time for each run, depends on the configuration, usually ranges from 10000 to 40000 minutes with $10^8$ particles tracking.  A more practical approach is to calculate H at the middle of each step of a RMW and obtain the step-weighted H values (multiple step method).  Yet, due to the limited computing resources and time, and since the interests of this work was to estimate the overall neutron productions around the accelerator in terms of; configurations, field sizes, treatment nozzle positions, the one step method was used. The one step method was useed to calculate the neutron dose equivalent per absorbed proton dose at the middle of the largest step, i.e. the thinnest step, of the RMW for each configuration.

To evaluate the sufficiency of using one step of the RMW comparing to using all steps, weighted H/D values around the treatment nozzle were simulated for configuration C open field. There were 19 steps and one brass block in the RMW used for configuration C.  For multiple steps method, $1\times10^7$ proton histories were simulated in each step.  The results are listed in Table 4.12.  The differences of simulated H/D values from both methods are less than 20% (compared Table 4.12 with Table 4.6 open field).

**Table 4.12** The H/D values for configuration C using multiple step method. Where r is the neutron receptor's distance from the isocenter and θ is the angle with respect to the initial proton beam axis.

| | configuration C – open field | | | | |
|---|---|---|---|---|---|
| | H/D (mSv/Gy) | | | | |
| | angle (θ°) | | | | |
| Distance (r, cm) | 0 | 45 | 60 | 90 | 125 |
| 50 | | 3.05 | 3.11 | 2.98 | 3.37 |
| 75 | 1.63 | 2.20 | 2.21 | 2.39 | 3.26 |
| 100 | 1.31 | 1.83 | 1.89 | 2.19 | 3.22 |
| 125 | | 1.65 | 1.67 | 1.90 | 2.99 |
| 150 | | | 1.55 | 1.70 | 3.18 |

## 4.3.7    Outcome of Specific Aim and the Coherence with Literature

The goal of specific aim was to characterize the neutron production from the MEVION S250 proton accelerator by both measurement and Monte Carlo simulation techniques. Depending on the configurations, at least 24 locations for each configuration were investigated. The calculated values agreed with measured values within a factor of 2.  Overall, the ambient neutron dose equivalent per therapeutic proton dose (H/D) around the MEVION S250 proton accelerator is found to be influenced by the configuration design, i.e. proton range and spread out Bragg peak, treatment nozzle position, aperture field size and the positions where the neutron dose equivalent is determined.  For the standard reference point for determining dose to patient, i.e.  100 cm away from the isocenter and 90° with respect to the incident proton beam, the H/D values are found to decrease as the aperture field size increased, and to decrease as the distance between the treatment nozzle and the isocenter increased.

Neutron dose equivalent distributions around the treatment nozzle in this study are generally consistent with previous studies.  Neutron dose equivalent per therapeutic proton dose (H/D, mSv/Gy) compared to other studies for passive scattering systems are listed in Table 4.13.

**Table 4.13**   Comparison of H/D values with literature.

| Facility | Energy (MeV) | Range (cm) | SOBP (cm) | Field Size (cm) | Method[a] | Phantom | H/D at d cm lateral (mSv/Gy) | Ref |
|---|---|---|---|---|---|---|---|---|
| MEVION S250 | 250 | 32 | 10 | 14 | MC | Water | 1.03 (d=50) <br> 0.52 (d=100) | This study |
| MEVION S250 | 250 | 25 | 20 | 25 | MC | Water | 2.90 (d=50) <br> 2.25 (d=100) | This study |
| Harvard Cyclotron Laboratory (HCL) | 160 | 16 | 8.2 | Very large field | Meas. | Lucite | 4.80 (d=50) | [91] |
| Harvard Cyclotron Laboratory (HCL) | 160 | 15.8 | 8.5 | Large field size | MC | Lucite | 6.3 (d=50) <br> 1.8 (d=100) | [92] |
| MGH (Boston, MA) | 235 | 28.8 | 10.4 | -- | Meas. | Lucite | 0.3 (d=60) | [93] |
| LLUMC (Loma Linda, CA) | 250 | 28.9 | 10 | 14 | MC: no RMW | Water | 0.338 (d=100)[b] | [94] |
| MDACC (Houston, TX) | | 16 | 2 | 25.4 | Meas. | Water | 1.1 (d=50) | [97] |
| National Cancer Center, Korea | 230 | 20 | 9 | -- | Meas. +6.5cm brass | Water | 1.17 (d=50) | [98] |

[a] MC – Monte Carlo method; Meas. – Measurement.
[b] This H/D was at depth = 10 cm from isocenter.

## 4.3.8      Strengths and Limitations of This Study

This study was unique because the MEVION S250 proton accelerator was the first compact proton accelerator available, so that the neutron assessments in this study provided the first glimpse of the neutron distribution around this proton accelerator. Unlike other single room passive scattering proton accelerators, this unit had the cyclotron in the same room with patients. To benchmark the H/D results reported, the details of the cyclotron was thus included in the Monte Carlo simulations as needed.

There were several limitations of this study. First, both measurements and Monte Carlo simulations in this study were based on the first prototype of the MEVION S250 proton accelerator located in the Still River System in Massachusetts. All the shielding parameters around the accelerator were specific to their facility. In addition, the system was still under some minor design adjustments for some configurations. The neutron dose equivalent per therapeutic doses reported in this study hence might not be representative of the proton facility in Washington University School of Medicine in St. Louis (WUSM). However, simulations were benchmarked against each measurement condition in this study, and the H/D results were found to be within a factor of 2. The neutron productions in the facility in WUSM thus could use a similar model for calculations in the future. Second, this work only investigated 4 out of 24 configurations that the MEVION S250 offered. Although these 4 configurations were believed to "the worst case scenario" cases in terms of neutron radiation, the other 20 configurations should be investigated to provide full evaluation of neutron productions around the MEVION S250 proton accelerator. Third, H/D values reported in this study in terms of treatment nozzle distances from the isocenter were based on open fields, i.e. no brass apertures in place. Since

these final collimators were other main neutron sources to patients, additional modeling could be done for closed aperture cases.

## 4.4    Conclusions

Neutron productions around the MEVION S250 proton accelerator were evaluated with measurements and Monte Carlo simulations.  Measured H/D values were found to be within a factor of 2 of the calculated values.  H/D values decreased as the field sizes increased.  As a function of distance from the isocenter, H/D values decreased as distance increased. Calculations and measurements in this work agreed well with prior investigations for passive scattering systems.

## BIBLIOGRAPHY

[1]     Parker RG, Enstrom JE. Second Primary Cancers of the Head and Neck Following of Initial Primary Head and Neck Cancers. *Int. J. Radiation Oncology Biol. Phys.* 1988;14:561-564.

[2]     Movsas B, Hanlon AL, Pinover W, Hanks GE. Is There an Increased Risk of Second Primaries Following Prostate Irradiation? *Int. J. Radiation Oncology Biol. Phys.* 1998;41(2):251-255.

[3]     Brenner DJ, Curtis RE, Hall EJ, Ron E. Second Malignancies in Prostate Carcinoma Patients after Radiotherapy Compared with Surgery. *Cancer*. 2000;88(2):398-406.

[4]     Bostrom PJ, Soloway MS. Secondary Cancer After Radiotherapy for Prostate Cancer: Should We Be More Aware of The Risk? *European Urology*. 2007;52(4):973-982.

[5]     Rapiti E, Fioretta G, Verkooijen HM, et al. Increased Risk of Colon Cancer after External Radiation Therapy for Prostate Cancer. *Int. J. Cancer*. 2008;123(5):1141-1145.

[6]     Bhojani N, Capitanio U, Suardi N, et al. The Rate of Secondary Malignancies after Radical Prostatectomy versus External Beam Radiation Therapy for Localized Prostate Cancer: A Population-Based Study on 17,845 Patients. *IInt. J. Radiation Oncology Biol. Phys.* 2010;76(2):342-348.

[7]     Sigurdson AJ, Jones IM. Second Cancers after Radiotherapy: Any Evidence for Radiation-Induced Genomic Instability? *Oncogene*. 2003;22(45):7018-7027.

[8]     Abdel-Wahab M, Reis IM, Hamilton K. Second Primary Cancer after Radiotherapy for Prostate Cancer-A SEER Analysis of Brachytherapy versus External Beam Radiotherapy. *Int. J. Radiation Oncology Biol. Phys.* 2008;72(1):58-68.

[9]     Hall E. The Impact of Protons on The Incident of Second Malignancies in Radiotherapy. *Technol Cancer Res Treat* 2007; 6:31-34.

[10]    Schneider U, Lomax A, Lombriser N. Comparative Risk Assessment of Secondary Cancer Incidence after Treatment of Hodgkin's Disease with Photon and Proton Radiation. *Radiat Res*. 2000;154(4):382-388.

[11]    Sources: Physician Characteristics and Distribution in the U.S., 2008 Edition, 2004 IMV Medical Information Division, 2003 SROA Benchmarking Survey.

[12]    NCRP, 1971. Protection against Neutron Radiation. *Report No. 38*. Washington, D.C.: National Council on Radiation Protection and Measurements.

[13]    Tsoulfanidis N, Landsberger S. *Measurement and Detection of Radiation*. 3rd edition. CRC Press; 2010.

[14]    Stabin MG. *Radiation Protection and Dosimetry: An Introduction to Health Physics*. New York: Springer; 2007.

[15] Bramblett R, Ewing RI, Bonner TW. A New Type of Neutron Spectrometer. *Nucl. Instrum. Methods*. 1960;9(1):1–12.

[16] Olsher RH, Hsu H, Beverding A, et al. WENDI: an Improved Neutron REM Meter. *Health Phys*. 2000;78(2):170-181.

[17] Olsher RH, MclLean TD. High-Energy Response of the PRESCILA and WENDI-II Neutron REM Meters. *Radiat Prot Dosimetry*. 2008;130(4):510-513.

[18] Ing H, Houlty RA, MclLean TD. Bubble detectors — A Maturing Technology. *Radiation Measurements*. 1997;27(1):1-11.

[19] Roy S. C., Superheated Liquid and Its Place in Radiation Physics, *Radiat Phys. Chem.*, 2001, 61:271-281.

[20] d'Errico F. Status of Radiation Detection with Superheated Emulsions. *Radiat Prot Dosimetry*. 2006;120(1-4):475-479.

[21] Perowitz, D.B. *MCNPX$^{TM}$ USER'S MANUAL*, version 2.6.0, Los Alamos National Laboratory, New Mexico, 2008.

[22] Berger, MJ. Monte Carlo Calculation of the Penetration and Diffusion of Fast Charged Particles, in *Methods in Computational Physics, Vol 1*, edited by Alder, B, Fernbach, S and Rotenberg, M. New York: 1963.

[23] Goudsmit, S and Saunderson, L. Multiple Scattering of Electrons. *Phys. Rev.*,1940, 57:24.

[24] Landau, L. On the Energy Loss of Fast Particles by Ionization. *J. Phys. USSR*, 1944:201.

[25] Blunck, O and Leisegang, S. Zum Energieverlust schneller Elektronen in dünnen Schichten. *Z. Physik,* 1950,128:500.

[26] Koch, KW and Motz, JW. Bremsstrahlung Cross-Section Formulas and Related Data. *Rev. Mod. Phys.*, 1959, 31:920.

[27] Huges, HG. LA-UR-96-4583. *Treating Electron Transport in MCNP$^{TM}$*. Los Alamos National Laboratory, New Mexico, 1996.

[28] X-5 Monte Carlo Team. LA-UR-03-1987. *MCNPX – A General Monte Carlo N-Particle Transport Code,* version 5. Volume 1: Overview and Theory. Los Alamos National Laboratory, New Mexico, 2008.

[29] ICRP, 1996. Conversion Coefficients for use in Radiological Protection against External Radiation. *ICRP Publication 74*. Ann. ICRP 26 (3-4).

[30] Stabin MG. *Radiation Protection and Dosimetry: An Introduction to Health Physics*. New York: Springer; 2007.

[31] Martin JE. *Physics for Radiation Protection: A Handbook*. 2$^{nd}$ edition. Wiley-VCH Verlag GmbH & Co.; 2006.

[32]  NCRP, 2003. Radiation Protection for Particle Accelerator Facilities. *Report No. 144*. Bethesda, MD: National Council on Radiation Protection and Measurements.

[33]  Avery S, Ainsley C, Maughan R, McDonough J. Analytical Shielding Calculations for a Proton Therapy Facility. *Radiation Prot dosimetry*. 2008;131(2):167-179.

[34]  Volkman DE. Concrete for Radiation Shielding. In: Lamond JF, Pielert JH *Significance of Tests and Properties of Concrete and Concrete-Making Materials*. West Conshohocken, PA: ASTM International; 2006:570-577.

[35]  Metha PK, Monteiro PJ. *Concrete: Microstructure, Properties, and Materials*. 3rd. Blacklick, OH: McGraw-Hill Professional; 2005

[36]  Bashter II. Calculation of Radiation Attenuation Coefficients for Shielding Concretes. *Annals of Nuclear Energy*. 1997;24(17):1389-1401.

[37]  Abdo AE. Calculation of the Cross-Sections for Fast Neutrons and Gamma-Rays in Concrete Shields. *Annals of Nuclear Energy*. 2002;29(16):1977-1988.

[38]  Akkurt I, Basyigit C, Kilincarslan S, Mavi B, Akkurt A. Radiation Shielding of Concretes Containing Different Aggregates. *Cement and Concrete Composites*. 2006;28(2):153-157.

[39]  Facure A, Silva AX. The Use of High-Density Concretes in Radiotherapy Treatment Room Design. *Applied radiation and isotopes: including data, instrumentation and methods for use in agriculture, industry and medicine*. 2007;65(9):1023-1028.

[40]  Kharita M, Takeyeddin M, Alnassar M, Yousef S. Development of Special Radiation Shielding Concretes using Natural Local Materials and Evaluation of Their Shielding Characteristics. *Progress in Nuclear Energy*. 2008;50(1):33-36.

[41]  Griffin MA, Landsberger S, Biegalski S, Cournoyer ME. Characterization of A Plutonium Beryllium Source for Use in Neutron Damage Studies. *Journal of Radioanalytical and Nuclear Chemistry*. 2008;276(3):807-811.

[42]  Thomas D, Alevra A. Bonner Sphere Spectrometers – a Critical Review. *Nuclear Instruments and Methods in Physics Research Section A: Accelerators, Spectrometers, Detectors and Associated Equipment*. 2002;476(1-2):12-20.

[43]  Alevra aV, Thomas DJ. Neutron Spectrometry in Mixed Fields: Multisphere Spectrometers. *Radiat Prot Dosimetry*. 2003;107(1-3):37-72.

[44]  Miller WH and Bugger RM. Additional Experimental Tests of the Bonner Sphere Neutron Spectrometer. *Nuclear Instruments and Methods in Physics Research A*. 1985;236(2):333-339.

[45]  R Williams III, Gesh CJ, and Pagh RT. Compedium of Material Composition Data for Radiation Transport Modeling. PNNL-15870, Pacific Northwest National Laboratory, Richland, WA. 2006.

[46] McConn RJ, Jr, CJ Gesh, RT Pagh, RA Rucker, and R Williams III. Compendium of Material Composition Data for Radiation Transport Modeling. PNNL-15870 Rev. 1, Pacific Northwest National Laboratory, Richland, WA. 2011.

[47] Material data sheet for SWX-201HD, Shieldwerx[TM], NM. Available at: http://shieldwerx.com

[48] *Shielding Calculation for the BJH Proton Facility*. Washington University in St. Louis, Missouri, 2007.

[49] Sullivan AH. *A Guide to Radiation and Radioactivity Levels near High Energy Particle Accelerators*. Nuclear Technology Publishing, 1992.

[50] Kase KR et al., Neutron Fluence and Energy Spectrum around the Varian CLinac 2100C/2300C Medical Accelerator. *Health Phy.* 1998;74:38-47.

[51] NCRP, 1984. Neutron Contamination from Medical Electron Accelerators. *Report No. 79*. Bethesda, MD: National Council on Radiation Protection and Measurements.

[52] Liu JC, Nelson WR, Kase KR, and Mao XS. Calculations of the Giant-Dipole-Resonance Photoneutrons using a Copled EGS4-MORSE Code. *Radiat Prot Dosimetry*. 1997;70(1-4):49-54.

[53] Barber WC and Georget WD. Neutron Yields from Targets Bombarded by Electrons. *Phys. Rev.*, 1959,116(6):1551-1559.

[54] McCall RC, Jenkins TM, and Shore RA. Transport of Accelrator Produced Neutrons in a Concrete Room. *IEEE Trans. Nucl. Sci. L.*, 1979,26(1):1593-1602.

[55] McGinley PH. *Shielding Techniques for Radiation Oncology Facilities*. Medical Physics Publishing, Madison, Wisconsin, 1998.

[56] Chibani O and Ma CC. Photonuclear Dose Calculations for High-Energy Photon Beams from Siemens and Varian linacs. *Medical Physics*. 2003;30(8):1990.

[57] Ongaro C Zanini a, Nastasi U, et al. Analysis of photoneutron spectra produced in medical accelerators. *Physics in medicine and biology*. 2000;45(12):L55-61.

[58] Ipe N, Roesler S, Jiang S, Ma C. Neutron Measurements for Intensity Modulated Radiation Therapy. *Proceedings of the 22nd Annual International Conference of the IEEE Engineering in Medicine and Biology Society*. 2000;4(April):3234-3237.

[59] Paredes L et al., Fast Neutron Leakage in 18 MeV Medical Electron Accelerator. *Radiation Measurements*. 1999:31(1-6):475-478.

[60] Kry SF, Howell RM, Titt U, et al. Energy Spectra, Sources, and Shielding Considerations for Neutrons Generated by a Flattening Filter-Free Clinac. *Medical Physics*. 2008;35(5):1906-1911.

[61] Karzmark CJ, Nunan CS, Tanabe E. *Medical Electron Accelerators*. New York. McGraw-Hill, Inc; 1993.

[62] Verhaegen F, Seuntjens J. Monte Carlo Modelling of External Radiotherapy Photon Beams. *Phys. Med. Biol.* 2003;48(21):R107-164.

[63] C- Series Clinac Accelerator System Basics, (2002), Varian Medical Systems (Palo Alto, CA).

[64] Elaekta Precise 2nd Line Physics Training Course Manual, (2001), Elekta Inc. (Norcross, GA).

[65] Far West Technology Inc. URL: http://www.fwt.com. Accessed date: July, 2010.

[66] Followill DS, Stovall MS, Kry SF, Ibbott GS. Neutron Source Strength Measurements for Varian, Siemens, Elekta, and General Electric Linear Accelerators. *Journal of Applied Clinical Medical Physics/American College of Medical Physics*. 2003;4(3):189-94.

[67] Wilson RR. Radiological Use of Fast Protons. *Radiology*. 1946;47:487-491.

[68] Kjellberg RN, Hanamura T, Davis KR, et al. Bragg-Peak Proton-Beam Therapy for Arteriovenous Malformations of the Brain. *N Engl J Med*. 1983;309(5):269-274.

[69] Munzenrider JE. Proton Therapy for Uveal Melanomas and Other Eye Lesions. *Strahlenther Onkol*. 1999; 175(2):68-73.

[70] Egger E, Zografos L, Schalenbourg A, et al. Eye Retention after Proton Beam Radiotherapy for Uveal Melanoma. *Int J Radiat Oncol Biol Phys*. 2003;55(4):867-880.

[71] Shioyama Y, Tokuuye K, Okumura T, et al. Clinical Evaluation of Proton Radiotherapy for Non–Small-Cell Lung cancer. *Int J Radiat Oncol Biol Phys*. 2003;56(1):7-13.

[72] Hara I, Murakami M, Kagawa K, et al. Experience with Conformal Proton Therapy for Early Prostate Cancer. *Am J Clin Oncol*. 2004;27(4):323-327.

[73] Brada M, Pijls-Johannesma M, De Ruysscher D. Proton Therapy in Clinical Practice: Current Clinical Evidence. *Journal of clinical oncology*. 2007;25(8):965-970.

[74] McDonald MW, Fitzek MM. Proton Therapy. *Current problems in cancer*. 2010;34(4):257-296.

[75] Fuss M, Poljanc K, Miller DW, et al. Normal Tissue Complication Probability (NTCP) Calculations as a Means to Compare Proton and Photon Plans and Evaluation of Clinical Appropriateness of Calculated Values. *Int J Cancer*. 2000;90(6):351-8.

[76] Suit H, Urie M. Proton Beams in Radiation Therapy. *J Natl Cancer Inst*. 1992;84(3):155-164.

[77] Lomax AJ, Bortfeld T, Goitein G, et al. A Treatment Planning Inter-Comparison of Proton and Intensity Modulated Photon Radiotherapy. *Radiother Oncol*. 1999;51(3):257-271.

[78] Schneider U, Lomax A, Lombriser N. Comparative Risk Assessment of Secondary Cancer Incidence after Treatment of Hodgkin's Disease with Photon and Proton Radiation. *Radiat Res*. 2000;154(4):382-388.

[79] Chang JY, Zhang X, Wang X, et al. Significant Reduction of Normal Tissue Dose by Proton Radiotherapy Compared with Three-Dimensional Conformal or Intensity-Modulated

Radiation Therapy in Stage I or Stage III Non-Small-Cell Lung Cancer. *Int. J. Radiation Oncology Biol. Phys.* 2006;65(4):108710-96.

[80]  Cozzi L, Fogliata A, Lomax AJ, Bolsi A. A treatment planning comparison of 3D conformal therapy, intensity modulated photon therapy and proton therapy for treatment of advanced head and neck tumours. *Radiother Oncol* 2001;61:287-297.

[81]  Steneker M, Lomax A, Schneider U. Intensity Modulated Photon and Proton Therapy for the Treatment of Head and Neck Tumors. *Radiother Oncol.* 2006;80(2):263-267.

[82]  Vynckier S. Dosimetry of Clinical Neutron and Proton Beams: an Overview of Recommendations. *Radiat Pro Dosimetry*. 2004;110(1-4):565-572.

[83]  Delaney TF, Kooy HM, Proton and Charged Particle Radiotherapy. Lippncott Williams & Wilkins, 2008.

[84]  Flanz J, Smith A. Technology for Proton Therapy. *Cancer Journal*. 2009;15(4):292-297.

[85]  Gottschalk B, Pedroni E. Treatment Delivery Systems. In: DeLaney TF, Kooy HM Philadelphia: Lippincott Williams & Wilkins; 2008.

[86]  ICRU Report 59. Verhey L, Blattman H, DeLuca P, Miller D. Clinical Proton Dosimetry – Part I: Beam Production, Beam Delivery and Measurement of Absorbed Dose, 1998.

[87]  Hall EJ, PHil D, D Sc. Intensity-Modulated Radiation Therapy, Protons, and the Risk of Second Cancers. *Int. J. Radiation Oncology Biol. Phys.* 2006;65(1):1-7.

[88]  Zheng Y et al., Monte Carlo Simulations of Neutron Spectral Fluence, Radiation Weighting Factor and Ambient Dose Equivalent for a Passively Scattered Proton Therapy Unit. *Phys Med Biol*, 2008, 53:187-201.

[89]  Agosteo S, Birattari C, Caravaggio M, Silari M, Tosi G. Secondary Neutron and Photon Dose in Proton Therapy. *Radiother Oncol*. 1998;48(3):293-305.

[90]  Binns PJ and Hough JH. Secondary Dose Exposures During 200 MeV Proton Therapy. *Radiat. Prot. Dosim.* 1997,70:441–444.

[91]  Yan X, Titt U, Koehler A, Newhauser W. Measurement of Neutron Dose Equivalent to Proton Therapy Patients Outside of the Proton Radiation Field. *Nucl Instrum Methods A*. 2002;476(1-2):429-434.

[92]  Polf JC, Newhauser WD. Calculations of Neutron Dose Equivalent Exposures from Range-Modulated Proton Therapy Beams. *Phys Med Biol*. 2005;50(16):3859-73.

[93]  Wroe A, Clasie B, Kooy H, et al. Out-of-Field Dose Equivalents Delivered by Passively Scattered Therapeutic Proton Beams for Clinically Relevant Field Configurations. *Int. J. Radiation Oncology Biol. Phys.* 2009;73(1):306-313.

[94]  Moyers MF, Benton ER, Ghebremedhin A, Coutrakon G. Leakage and Scatter Radiation from a Double Scattering based Proton Beamline. *Medical Physics*. 2008;35(1):128-144.

[95]   Olsher RH, Hsu H, Beverding A, et al. WENDI: an Improved Neutron REM Meter. *Health Physics*. 2000;78(2):170-181.

[96]   Roy SC, Superheated Liquid and Its Place in Radiation Physics, *Radiat Phys. Chem.*, 2001, 61:271-281.

[97]   Wang X, Sahoo N, Zhu RX, Zullo JR and Gillin MT. Measurement of Neutron Dose Equivalent and Its Dependence on Beam Configuration for a Passive Scattering Proton Delivery System. Int. J. Radiat. Oncol. Biol. Phys. 2010;76(5):1563-1570.

[98]   Shin D, Yoon M, Kwak J, et al. Secondary Neutron Doses for Several Beam Configurations for Proton Therapy. *Int. J. Radiat. Oncol. Biol. Phys.* 2009;74(1):260-265.

# APPENDIX A – H(E$_n$)/D AS A FUNCTION OF DISTANCE

## A.1    Configuration B – Open Field

## A.2 Configuration C – Open Field
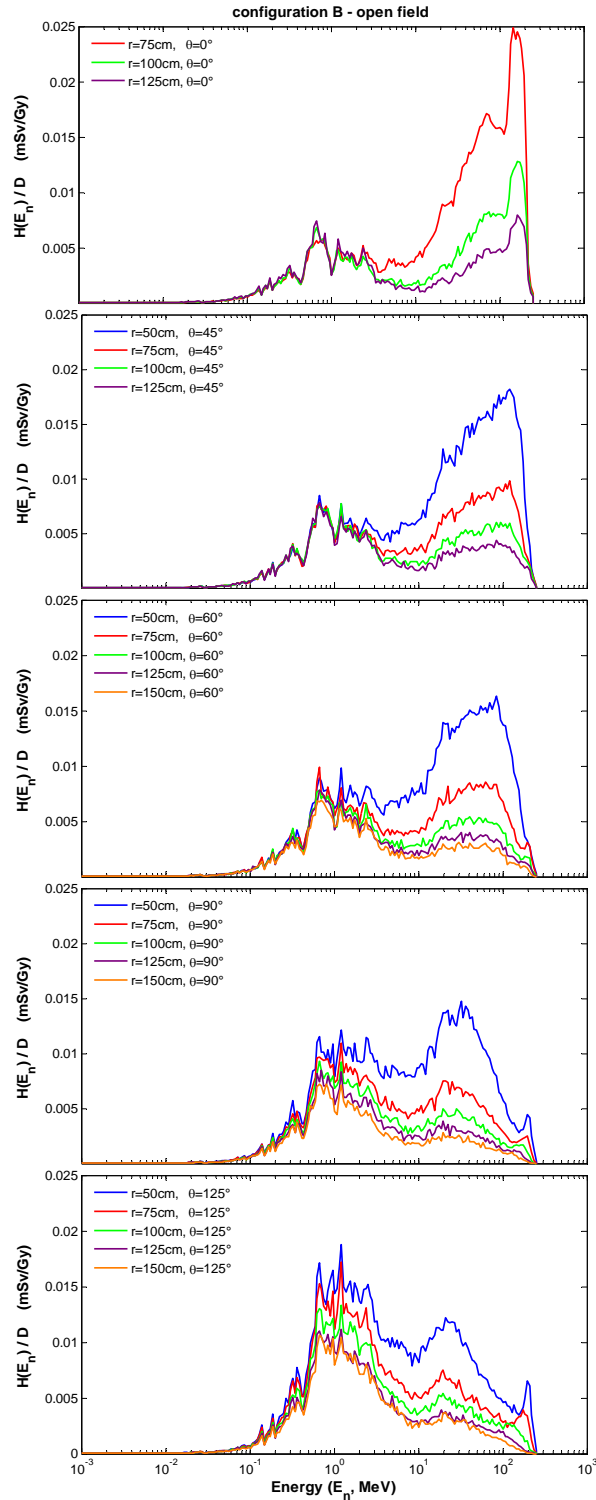


configuration C - open field
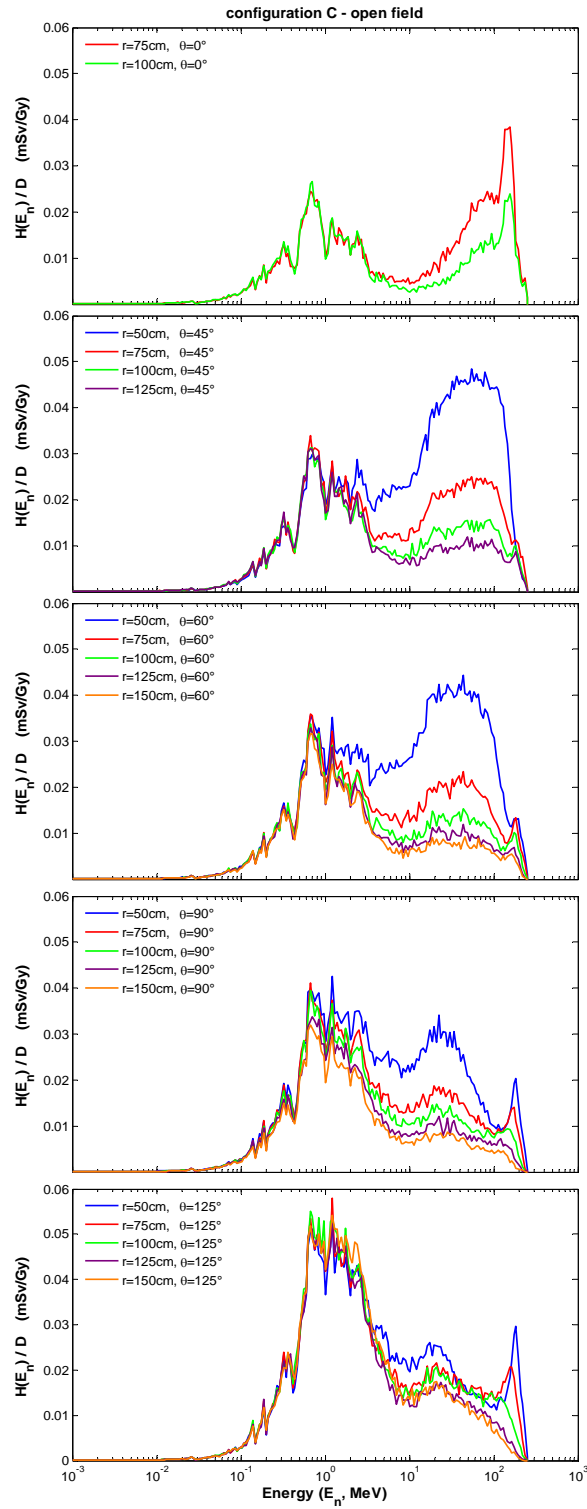
# GLOSSARY

**Absorbed Dose** (D; unit: gray(Gy))

mean energy imparted by ionizing radiation to matter of mass.
[ 1 Gray (Gy) = 1 J/Kg = 100 rad = $6.24 \times 10^{12}$ MeV/kg deposited energy ]

**Ambient Dose Equivalent** (H*(d); unit: sievert(Sv))

at a point in a radiation field is the dose equivalent that would be produced by the corresponding expanded and aligned field in the ICRU sphere at the depth d, on the radius opposing the direction of the aligned field.
1 Sievert (Sv) = 100 Rem (Roentgen equivalent of man)

**Dose Equivalent** (H; unit: sievert(Sv))

the product of absorbed dose (D) and the quality factor (Q) at a point in tissue.

**Effective Dose** (E; unit: gray(Gy))

a summation of the equivalent doses in tissues or organs ($H_T$), each multiplied by the appropriate tissue weighting factor ($W_T$)

**Equivalent Dose** ($H_{T,R}$; unit: sievert(Sv))

the product of absorbed dose averaged over the tissue or organ due to radiation R, ($D_{T,R}$) and the relevant radiation weighting factor for radiation R, ($W_R$).

**Exposure**

A measurement of photon fluence at a certain point in space integrated over time, in terms of ion charge of either sign produced by secondary electrons in a small volume of air about that point
[1 C/kg of air (1 Roentgen (R) = $2.58 \times 10^{-4}$ C/kg)]

**Fluence** ($\Phi$; unit: $m^{-2}$)

The number of particles incident on a sphere of cross section area

**Linear Energy Transfer** (LET; unit: keV/μm)

the rate of energy loss by the radiation in the medium.

**Monitor Unit** (MU)

100 MU/Gy defines depth dose maximum in a water phantom irradiated with a 10 cm × 10 cm field.

**Radiation Weighting Factor** ($w_R$)

formally the quality factor Q, but $w_R$ is defined for radiation incident on the body.

**Range**

the mean depth of penetration measured along a straight line of the protons when they enter the medium to the point where additional displacement is no longer detectable.

**Relative Biological Effectiveness**

the ratio of doses required to reach a given biological endpoint, all other conditions being kept constant.

# VITA

     Kuan Ling (Gwen) Chen was born in Taipei, Taiwan.  She received a Bachelor of Science degree in Medical Radiation Technology in Kaohsiung Medical University in Kaohsiung, Taiwan in June, 2003.  In August 2006, she began the pursuit of a Master of Science degree in Nuclear Engineering at the University of Missouri–Columbia in Columbia, Missouri.  She completed the degree with an emphasis on Medical Physics in December 2008.  In January 2009, she continued her education in the Nuclear Science and Engineering Institute at the University of Missouri–Columbia.  She received her Doctor of Philosophy in Nuclear Engineering in December 2011.